LBL-23333 c.2

Lawrence Berkeley Laboratory
UNIVERSITY OF CALIFORNIA

Materials & Chemical Sciences Division

RECEIVED
LAWRENCE
BERKELEY LABORATORY
JUN 9 1987
LIBRARY AND
DOCUMENTS SECTION

ON MECHANICAL BEHAVIOR OF METAL-CERAMIC BONDED SYSTEMS

M.-C. Lu
(Ph.D. Thesis)

April 1987

TWO-WEEK LOAN COPY

This is a Library Circulating Copy which may be borrowed for two weeks.

LBL-23333 c.2

Prepared for the U.S. Department of Energy under Contract DE-AC03-76SF00098

DISCLAIMER

This document was prepared as an account of work sponsored by the United States Government. While this document is believed to contain correct information, neither the United States Government nor any agency thereof, nor the Regents of the University of California, nor any of their employees, makes any warranty, express or implied, or assumes any legal responsibility for the accuracy, completeness, or usefulness of any information, apparatus, product, or process disclosed, or represents that its use would not infringe privately owned rights. Reference herein to any specific commercial product, process, or service by its trade name, trademark, manufacturer, or otherwise, does not necessarily constitute or imply its endorsement, recommendation, or favoring by the United States Government or any agency thereof, or the Regents of the University of California. The views and opinions of authors expressed herein do not necessarily state or reflect those of the United States Government or any agency thereof or the Regents of the University of California.

On Mechanical Behavior of Metal-Ceramic Bonded Systems

Mei-Chien Lu

Ph.D. Thesis

Materials and Chemical Sciences Division
Lawrence Berkeley Laboratory
University of California
and
Department of Materials Science and Mineral Engineering
University of California
Berkeley, California 94720

April 1987

This work was supported by the Director, Office of Energy Research, Office of Basic Energy Sciences, Materials Sciences Division of the U.S. Department of Energy under Contract Number DE-AC03-76SF00098.

On Mechanical Behavior of Metal-Ceramic Bonded Systems

Ph.D Dissertation

Department of Materials Science
and Mineral Engineering

Mei-Chien Lu

ABSTRACT

A study of the mechanical behavior of metal/ceramic bonded systems is achieved by using a simple model system consisting of two ceramic bodies and a metal interlayer. The mismatch of the material properties across the interface strongly affects the stress fields in the system and thus the mechanical strength. Four important factors determine the mechanical strength of a bonded material; the yield strength of the metal, mismatch of material properties, the dimensionless thickness of the metal, d/h, and the defects at the interface.

The finite element method, in conjunction with the virtual extension technique, is used to evaluate the stress fields as well as the strain energy release rate and predict the possible failure strength. Edge dominated failure is found to be important when the yield strength of metal is large, whereas limit load failure may exist in the metal when the yield strength is small. Reduction of the thickness of the metal diminishes edge stress concentrations and increases

the limit load. Residual stresses and the crack blunting induced by metal plasticity also affect the failure.

The failure strength of diffusion bonded Al_2O_3/Au is evaluated by a bending test and the corresponding microstructure at the interface examined by scanning electron microscopy. The effect of the defects at the interface is then related to the stress fields, through the use of failure statistics.

A map including the general failure mechanisms is presented to summarize the mechanical behavior of the bonded systems.

ACKNOWLEDGEMENTS

I want to express my sincere gratitude and appreciation to Prof. Anthony G. Evans, who supervised my research work and gave excellent guidance to finish this work. I thank Prof. Robert O. Ritchie and Prof. Hari Dharan for their valuable comments and suggestions in reviewing the manuscript. I am also indebted to Prof. Robert L. Taylor who provided me with the software package and the guidance, which was essential for this research.

Taking this opportunity, I would like to thank the people in our group for their friendship and helpful discussion, especially, Dr. Chun-Huey Hsueh, Dr. Rowland Cannon, Dr. Brian Dalgleish, Heng-Chu Cao, Ellice Luh, Kathy Lewis, Tae-Son Oh, and Jei-Min Zhu.

I am very grateful to my parents, sisters and brother for their encouragement which sustains me throughout the years of my graduate study. Finally, I would like to give special appreciation to my husband, An-Chang, for his care, love, encouragement and patience.

TABLE OF CONTENTS

CHAPTER 1 : Introduction 1

Figure Captions 4

Figures of Chapter 1 5

CHAPTER 2 : Background 7

2.1 : Work of Adhesion 8

2.2 : Diffusion Bonding 9

2.3 : Stresses 10

2.4 : Fracture Parameters 12

Figure Captions 14

Figures of Chapter 2 15

CHAPTER 3 : Mechanical Behavior Under Linear Elastic Conditions 16

3.1 : Introduction 16

3.2 : Finite Element Considerations 17

3.3 : Results 20

3.4 : Remarks 24

Figure Captions 25

Figures of Chapter 3 27

CHAPTER 4 : Mechanical Behavior Under Elastic-Plastic Conditions 39

4.1 : Introduction 39

4.2 Limit Load 40

4.3 : Plastic Deformation Around An Interface Crack 43

4.4 : Concluding Remarks 44

Figure Captions 46

Figures of Chapter 4 49

CHAPTER 5 : Interfacial Strength : Experimental Observations
And Failure Statistics 65

5.1 : Experimental Observations 65

5.2 : Failure Statistics 69

Figure Captions 73

Figures of Chapter 5 76

CHAPTER 6 : Summary and Conclusions 96

Figure Captions 98

Figures of Chapter 6 99

REFERENCES 102

CHAPTER 1

INTRODUCTION

The successful technological utilization of ceramic components [1] often requires that methods be found to connect to other components [2-4], e.g. ceramic rotors bonded to a metal shaft in gas turbines. Metal/ceramic bonding is also important for metal thin films deposited onto ceramic substrates in VLSI circuits, as well as for metal conductors within ceramic substrates in electronic packages. The mechanical behavior of such bonded systems is usually influenced by the applied load and the geometry. A simple model (Fig.1-1) consisting of two ceramic bodies bonded by an intermediate metal is considered in the present work in order to understand the fundamental behavior. In general, a monolithic ceramic material fails catastrophically at room temperature [5] and exhibits a linear stress-strain curve (Fig. 1-2(a)). Conversely, an elastic perfectly plastic metal fails by ductile fracture at a limit load (Fig.1-2(a)). The stress-strain relation for a bonded system is likely to vary between these extremes (Fig.1-2(b)) and will be investigated in the present study.

Four characteristics are critical in metal/ceramic bonded systems. The mismatch both of elastic constants and of thermal expansion coefficients create a discontinuity of physical properties across the interface and induce concentrated stress fields. Metal plasticity can alter stress distributions and cause crack initiation. The bond geometry also affects the stress distribution and thus, the mechanical strength. Debonding at the interface can destroy the

fundamental properties, as well as induce mechanical failure.

The literature regarding metal/ceramic bonded systems can be divided into two groups. One emphasizes plane problems of bonded dissimilar media under different loading conditions [6-22]. Several issues are of importance in this context: the stress singularity at the tip of interface cracks and relations with the fracture criterion, the singularity at the edge of the interface, and the appropriate composite parameters that represent the degree of mismatch. The second group involves experiments, concerned mostly with trends in bonding [23-40] and simple bending tests to measure the strength. The present study constitutes a preliminary attempt to connect these approaches, leading to the development of quantitative relations between the measured strength and the mechanics of the system.

The main objective of the present work is thus to improve the fundamental understanding of the strength of metal/ceramic bonded systems, by incorporating such variables as the mismatch of physical properties, plasticity, geometry and interfacial microstructure. For this purpose coupled finite element and slip line field analysis are used to determine stress fields in the ceramic and metal close to the interface. The study of interfacial behavior also includes the experimental observation of interface cracks and the finite element calculation of the plastic zone, as well as the associated stress fields and strain energy release rate for interface cracks. The bulk interfacial strength is investigated by four point bending and a statistical analysis used to relate the microstructure to the observed strength.

A brief review of both the characteristics of bonded bi-material systems and the nature of adhesion is included in chapter 2, in order to establish a basis for the approach. The behavior of bonded strips under linear elastic condition is described in chapter 3, with emphasis on the importance of the edge.

The effect of metal plasticity is investigated in chapter 4, including limit load conditions and the reduction of stress concentrations by metal plasticity at an interface crack tip. Bending tests conducted to measure the strength, and to relate failure to the interface flaws are described in chapter 5. Finally, the last chapter summarizes the contribution of each factor to the strength of the bonded system.

Figure Captions

Fig.1-1

An illustration of the model system consisting of two blocks of ceramic bonded with an interlayer of metal in plane strain under uniaxial tension.

Fig.1-2

(a) Failure characteristics of monolithic ceramic and elasitc perfectly plastic metal in stress-strain curve. (b) A possible stress- strain curve for bonded sandwich material consisting of the materials in (a).

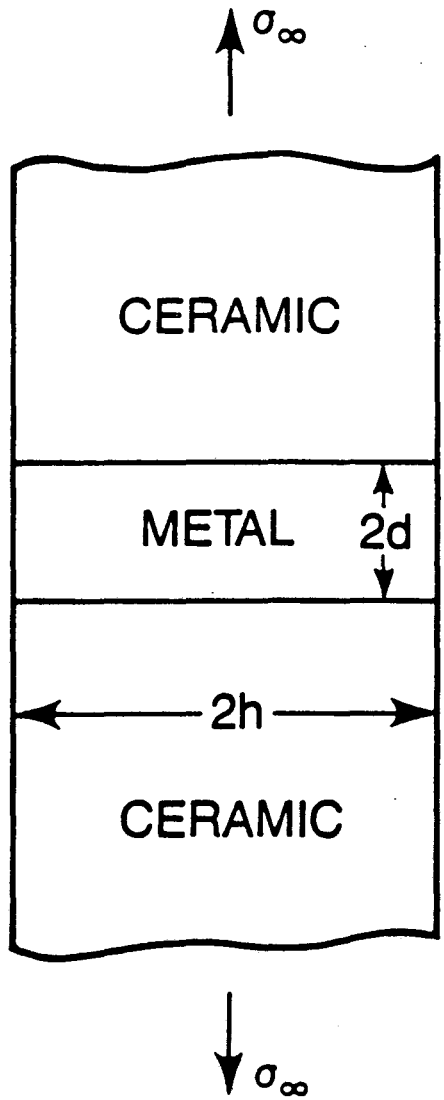

XBL 874-6284

Fig.1-1

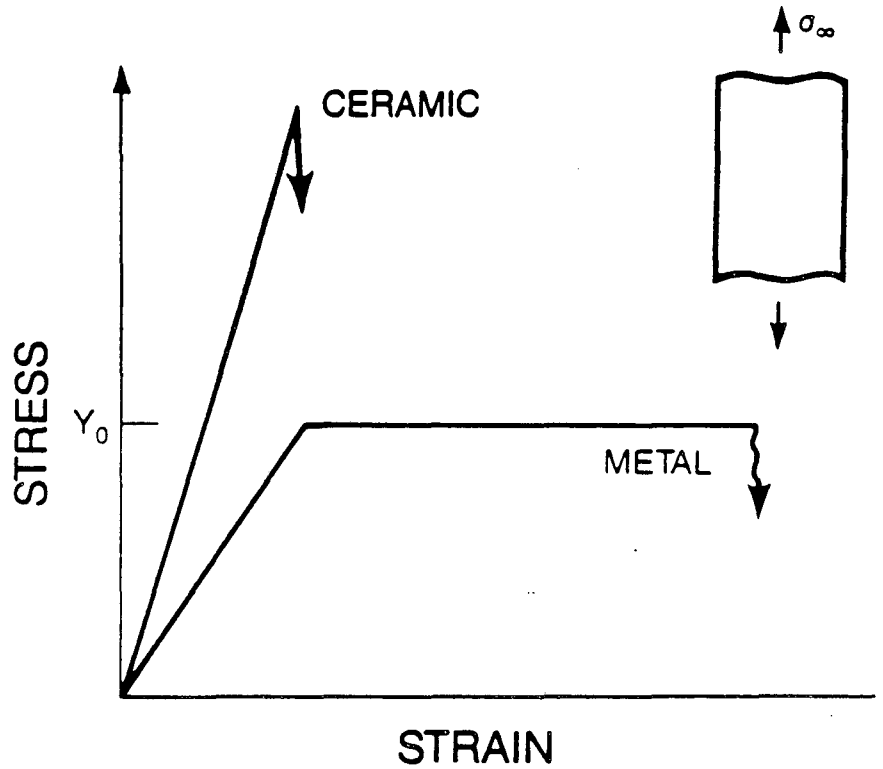

(a)

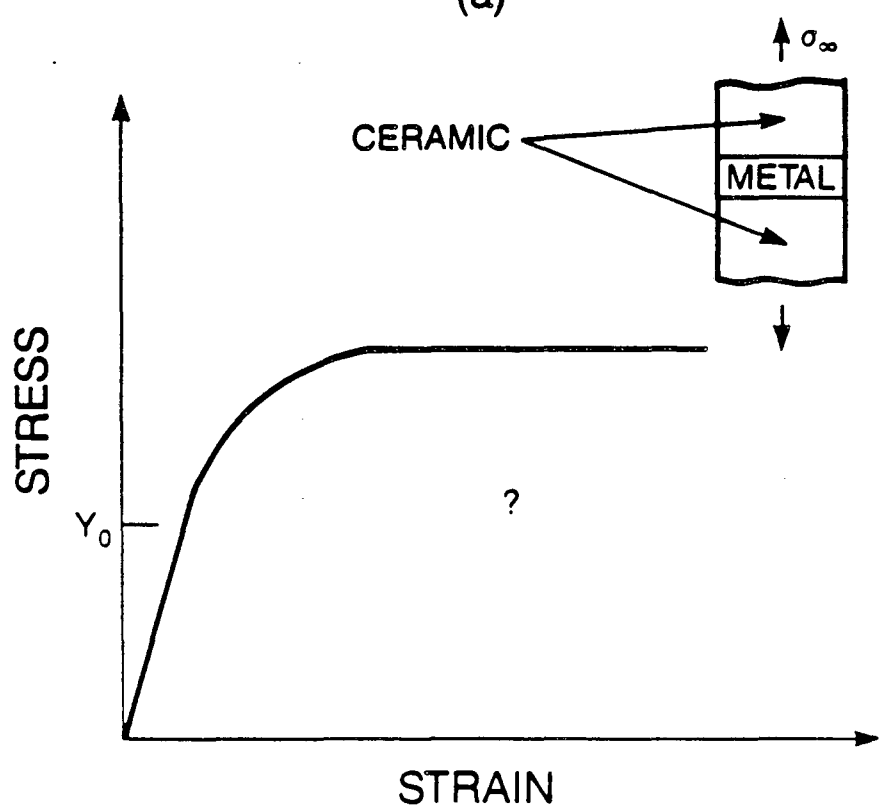

(b) XBL 874-6282

Fig.1-2

CHAPTER 2

BACKGROUND

Commonly used **adhesives** include organics, inorganic cements and glasses or glass ceramics. Organic adhesives are usually used at room temperature. Inorganic cements are composed of the silicates of Ca and Na, aluminum phosphate, calcium aluminate, magnesium oxychloride, etc., with or without an inorganic filler. However, their adhesion to metals is not good [37].

Glasses or glass-ceramics have wider applications. The method entails **glazing** both the metal and the ceramic by choosing the proper glass. Glazing is achieved by coating on a thin layer of powdered glass and melting. Then the bonding relies on the joining of the glazed surfaces. The parameters which affect the bonding strength are the wetting angle, the surface tension of the liquid glass and the viscosity. The strength is highly dependent of the temperature,via the viscosity of the glass.

In **metallizing,** a layer consisting of organic vehicles containing metallic and glass powders is placed on the ceramic. After heat-treatment, during which the organic is burned out and the glass melts, a glass-metal layer forms. Two glazed ceramic parts can then be adhered by using a proper brazing alloy [31].

Diffusion bonding [41-44] is a solid-state joining process by which two nominally flat surfaces are joined at an elevated temperature using an applied pressure. The temperature is usually in the region of 0.5 - 0.95 T_m , where T_m is the absolute melting point of the material being bonded. When two

different materials are bonded, the bonding temperature is determined by the constituent with the lower melting point. The applied pressure must be sufficiently low so that no large-scale deformation.

The advantages of the diffusion bonding technique are:

(1) low deformation, enabling machined parts to be joined without distortion

(2) the ability to join large areas

(3) possibilities for joining materials in non-conventional situations

When a metal and ceramic are bonded by this technique, two groups of bond result. A well-defined interface is observed for noble metals (e.g. Au ,Ag ,Pt ,Nb) bonded to Al_2O_3. In many other cases a reaction occurs between the ceramic and the metal (e.g. Zr bonded to Si_3N_4) producing a second phase at the interfacial zone. The second phase often weakens the interface.

1. Work of Adhesion

The work of adhesion, W_{ad} , as defined in the classical Young's formula, is simply the algebraic difference between the surface free energies of the two separate surfaces and the pre-existing interface [45-48].

$$W_{ad} = \gamma_m + \gamma_c - \gamma_{mc} \tag{2-1}$$

The reversible equilibrium work of adhesion, can be measured from the geometry of voids at the interface. When equilibrium is achieved (Fig.2-1), the interfacial free energy, γ_{mc} , is related to the dihedral angle by,

$$\gamma_{mc} = \gamma_c + \gamma_m \cos\theta \tag{2-2}$$

Hence,

$$W_{ad} = \gamma_m (1 - \cos\theta) \tag{2-3}$$

2. Diffusion Bonding

The work of Derby and Wallach [41-44] on the diffusion bonding of two identical metals provides insight regarding metal-to-ceramic systems. The mechanism is based on the assumption that diffusion bonding is analogous to pressure sintering; accordingly, mass transport may involve,

(1) surface diffusion from surface sources to a neck

(2) volume diffusion from surface sources to a neck

(3) diffusion along the bond interface from interfacial sources to a neck

(4) volume diffusion from interfacial sources to a neck

(5) power law creep

(6) plastic yielding.

Plastic yielding only occurs at the beginning when the local contact stresses due to the roughness are higher than the yield strength. The combined effects of microdeformation and diffusion operating at the interface are summarized in Table 2-1.

Table.2-1.

Some possible diffusion-bonding mechanisms

Mechanism	Effect
Plastic deformation	instantaneous deformation of surface asperities or collapse of interfacial voids
Surface diffusion	transfer of material along the void surface, pore volume unaffected
Interface diffusion	transfer of material from the interface to a void, decreased pore volume
Bulk diffusion	transfer of material through the bulk to a void;

Creep flow	deformation of surface asperities or collapse of interfacial voids

The regime of dominance of each mechanism is dependent on the bonding conditions; pressure, temperature, time and the surface roughness as well as the material properties. In general, high pressure and high temperature enhance the bonding process. Initial roughness results in inhomogeneous void elimination and related effects on the interfacial strength.

3. Stresses

Several methods have been used to solve plane elasticity problems in dissimilar materials, such as eigen-function expansions [9] and Hilbert problems [10]. The fundamental complex stress functions are formulated by Kolosov-Muskhelishvili [12]:

$$(\sigma_{xx})_j + (\sigma_{yy})_j = 4\mathrm{Re}[\phi_j(z)] \tag{2-4}$$

$$(\sigma_{yy})_j - (\sigma_{xx})_j + 2i(\sigma_{xy})_j = 2[\bar{z}\Phi_j'(z) + \Psi_j'(z)] \tag{2-5}$$

where j = 1,2 refer to materials 1 and 2 respectively, $z = x + iy$ ($\phi(z)_j'$ and $\psi(z)_j'$ be $\Phi(z)_j$ and $\Psi(z)_j$ respectively) and the potentials $\phi_j(z)$ and $\psi_j(z)$ satisfy the Airy stress function

$$U = \mathrm{Re}[\bar{z}\phi_j(z) + \psi_j(z)] \tag{2-6}$$

The corresponding displacements can be expressed as follows:

$$2G_j(u_{x\,j} + iu_{y\,j}) = \kappa_j\phi_j(z) - z\bar{\phi}_j(\bar{z}) - \bar{\psi}_j(\bar{z}) \tag{2-7}$$

where G_j denotes the shear modulus, $\kappa_j = 3-4\nu_j$ for plane strain and $\kappa_j = (3-\nu_j)/(1+\nu_j)$ for generalized plane stress, ν_j being Poisson's ratio.

A composite body consisting of two isotropic, elastic phases subject to prescribed surface tractions, has a stress field that depends on three parameters involving the elastic constants. However, for plane deformation without net forces on internal boundaries, two combinations of elastic constants characterize the stress. For bonded interfaces, with the displacements and tractions being continuous at the interface, the two appropriate constants, proposed by Dunders [8], are;

$$\alpha = \frac{\Gamma(\kappa_1+1) - (\kappa_2+1)}{\Gamma(\kappa_1+1) + (\kappa_2+1)} \tag{2-8}$$

$$\beta = \frac{\Gamma(\kappa_1-1) - (\kappa_2-1)}{\Gamma(\kappa_1+1) + (\kappa_2+1)} \tag{2-9}$$

where $\Gamma = G_2/G_1$. Another composite parameter, associated with interface cracks is called the bielastic constant [10],

$$\gamma = \left(\frac{\kappa_1}{G_1} + \frac{1}{G_2}\right) / \left(\frac{\kappa_2}{G_2} + \frac{1}{G_1}\right) \tag{2-10}$$

or [14]

$$\epsilon = \frac{1}{2\pi} \log\gamma \tag{2-11}$$

In engineering applications, parameter proposed by Elssner et al. [21] to express the effective modulus of elasticity for the bulk system is

$$E^* = 16\left[\frac{1+\kappa_1}{G_1} + \frac{1+\kappa_2}{G_2}\right]^{-1} \tag{2-12}$$

For dissimilar media, the modulus of the crack singularity remains proportional to the inverse square root of the distance from the tip, but also possesses an oscillatory character [9]

$$r^{-1/2} \sin (\epsilon \log r) \tag{2-13}$$

A sign change in the stresses thus occurs in the region very close to the crack tip. For example, in the glass-steel system, the region within which relative displacements oscillate is $0<(r/a)<10^{-7}$, implying contacting crack surfaces in this region [11].

First contact takes place at a distance δ from the ends of the crack

$$\log \left| \frac{2a-\delta}{\delta} \right| = \frac{\pi^2}{\log} \gamma \tag{2-14}$$

with a maximum occurring when $\gamma = 1/3$ *or* 3 . The value of the maximum is

$$\frac{\delta}{2a} \doteq 10^{-4} \tag{2-15}$$

The overlapping crack surfaces create ambiguity. However, since the irregularities are confined to small regions near the ends of the crack, it is often assumed that the linear elastic solution provides an adequate connection between the applied loads and the crack tip field, for purposes of fracture characterization.

4. Fracture Parameters

The stress intensity factors used in fracture mechanics constitute a measure of the strength of stress singularities. In dissimilar systems, the relevant stress intensity factors, defined by Rice and Sih [14] are

$$k_1 - ik_2 = 2\sqrt{2} e^{\epsilon\pi} \lim_{z \to 0} z^{(1/2 + i\epsilon)} \Phi_1(z) \tag{2-16}$$

Therefore, the explicit forms of the stress intensity factors for a small interfacial crack with symmetric and skew-symmetric loadings, σ_∞ , and τ_∞ are

$$k_1=\frac{\sigma_\infty[\cos(\epsilon\log 2a)+2\epsilon\sin(\epsilon\log 2a)]+\tau_\infty[\sin(\epsilon\log 2a)-2\epsilon\cos(\epsilon\log 2a)]}{\cosh\pi\epsilon}a^{1/2} \tag{2-17}$$

$$k_2=\frac{\tau_\infty[\cos(\epsilon\log 2a)+2\epsilon\sin(\epsilon\log 2a)]-\sigma_\infty[\sin(\epsilon\log 2a)-2\epsilon\cos(\epsilon\log 2a)]}{\cosh\pi\epsilon}a^{1/2} \tag{2-18}$$

where $2a$ is the crack length.

The corresponding strain energy release rate for unit crack extension along the interface is given by

$$\mathbf{G}=\frac{\sigma_\infty^2\pi a}{[4\cosh^2\pi\epsilon]\,(1+4\epsilon^2)}\left[\frac{(1-\nu_1)}{G_1}+\frac{(1-\nu_2)}{G_2}\right] \tag{2-19}$$

For present purposes, **G** is used as a fracture criterion. However, it is realized that this assumption is oversimplified and may be a poor choice, especially when k_2/k_1 becomes appreciable.

Figure Captions

Fig.2-1

The dihedral angle at the metal/ceramic bonded interface.

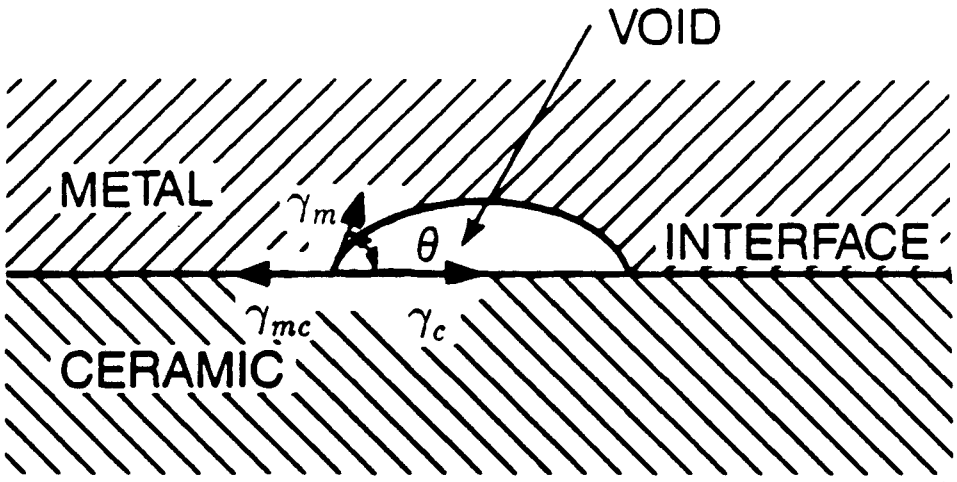

Fig.2-1

CHAPTER 3

MECHANICAL BEHAVIOR UNDER LINEAR ELASTIC CONDITIONS

1. Introduction:

The mechanical strength is determined by the stress state, the severity of pre-existent flaws, and the fracture toughness. Furthermore, high stress concentrations often occur at the interface near the edge induced by mismatch of elastic constants or thermal expansion coefficients. The effect of a mismatch in elastic constants is studied in this chapter and the corresponding effect of thermal expansion mismatch is estimated. A system consisting of a thin metal layer between two ceramic plates in plane strain and under uniaxial tension is chosen as a simple model to understand the strength of the singularity, the stress state around the singular point, and the strain energy release rate for edge cracks.

For the main purposes of fracture analysis, the stress state in the area around the interface is calculated for varying thicknesses of the metal layer. The corresponding change in the stress singularity at the interface edge is also addressed. The strain energy release rates for edge cracks are then evaluated numerically by using the virtual extension method, and finally, the strengths of the bonded systems are related to the strain energy release rates.

2. Finite Element Considerations

In homogeneous materials, the finite element approach to fracture mechanics [49-57] can be described as either direct or indirect. Two common direct methods [51] are the displacement method and the stress method, wherein the stresses or displacements in the vicinity of crack tip are fitted to the singular form. However, owing to the existence of the singularity, a relatively large number of near tip elements are needed and the error is usually about 10-20%.

In the indirect method [58-60], an energy release rate is calculated and stress intensity factors inferred from it. Several techniques for evaluating energy release rates have been described. These methods are based on either the change in potential energy for two crack lengths [52] or the change in compliance for sequential crack lengths [50]. The virtual crack extension method, originally suggested by Parks [53] and Hellen [54], is an efficient finite element procedure of the indirect type.

In bi-material systems, the most attractive approach combines a hybrid element with the virtual crack extension technique [20]. A method based on the crack closure integral also gives reasonable accuracy with only coarse grids [56].

2.1. Description of Method

When a crack extends by an amount Δa, conceptually, it may be visualized that the elastic body may be cut along the segment, $x = a$ to $x = a + \Delta a$, without releasing the stresses on the cut and then reducing their intensity by infinitesimally small increments until the segment Δa is stress free (Fig.3-1) The strain energy released is the work done in this process, by the stresses $\sigma_y(\Delta a - \beta^*, 0)$ acting through the displacements $u_y(\beta, \pi)$, provided that Δa is

very small, whereupon the conditions

$$u_y \rightarrow u_y^*, \qquad \beta \rightarrow \beta^* \tag{3-1}$$

are fulfilled. The work done at both ends of the crack is then

$$G = 2 \lim_{\Delta a \rightarrow 0} \frac{1}{2\Delta a} \int_0^{\Delta a} \frac{1}{2} \sigma_y (\Delta a - \beta, 0) u_y (\beta, \pi) d\beta \tag{3-2}$$

For an interface crack, the corresponding strain energy release rate is,

$$G = \lim_{\Delta a \rightarrow 0} \frac{1}{2\Delta a} \int_0^{\Delta a} \sigma_y (\Delta a - \beta, 0) [u_y^+(\beta,\pi) - u_y^-(\beta,\pi)] d\beta \tag{3-3}$$

$$+ \lim_{\Delta a \rightarrow 0} \frac{1}{2\Delta a} \int_0^{\Delta a} \sigma_{xy} (\Delta a - \beta, 0) [u_x^+(\beta,\pi) - u_x^-(\beta,\pi)] d\beta$$

In order to implement this concept within a finite element scheme [56], the crack tip stresses are replaced by nodal forces; therefore,

$$G = \lim_{\Delta a \rightarrow 0} \frac{1}{2\Delta a} \int_0^{\Delta a} F_c (u_y^c - u_y^d) \tag{3-4}$$

$$+ \lim_{\Delta a \rightarrow 0} \frac{1}{2\Delta a} \int_0^{\Delta a} T_c (u_x^c - u_x^d)$$

where the notation is indicated in Fig.3-2. Two sequential calculation with crack lengths a and $a + \Delta a$ are required to evaluate the nodal forces and crack opening, respectively, for every value of strain energy release rate.

2.2. Mesh Configurations

2.2.1. Singular Points

When a singular point exists in the system of analysis, a very fine mesh is usually used. Guydish and Fleming [57] studied the optimum mesh configuration for finite elements used in fracture mechanics. It was demonstrated that merely using smaller elements will not necessarily improve the solution accuracy. The general rules indicated three criteria. (i) It is necessary

that the elements immediately adjacent to the crack tip are very small in proportion to the crack length. The optimum size appears to be about $0.005a$ for the linear dimensions of these elements. (ii) The most efficient mesh results from a smooth progression of node spacing in all directions from the crack tip, and extending over a distance of at least one crack length. Beyond this distance there is no apparent limitation on element size. (iii) Very slender elements anywhere in the mesh produce errors. For best results, the aspect ratio of individual element should not exceed 50. The most essential and fundamental concept behind these rules is piece-wise interpolation. A discretization according to the gradient of the fields of solution can provide good accuracy. Therefore, a good estimation of the solution is important and useful.

Triangular and Quadrilateral linear displacement element are used. According to the rules discussed above, a fine mesh around each singular point, with the array of elements radiating from the singularity, accurately represents the angular stress and displacement gradient (Fig.3-3).

2.2.2. Virtual Crack Extension

A simple example of crack extension along the original crack plane is used to describe the mesh appropriate for the virtual crack extension calculations (Fig.3-4). A value of Δa is selected, as shown in Fig.3-4. Then, values of F_c and T_c are chosen to be the y- and x- forces, respectively, required to hold nodes c and d together. When evaluating F_c and T_c, it is convenient to maintain l_2 equal to Δa with elements 1,2,3 and 4 being the same size. The forces at the crack tip are obtained by placing very stiff springs between points e and f. Constraints are also applied in order to avoid the overlapping of elements. The ratio $\Delta a / a$ is selected to be less than 0.1. The accuracy of the strain energy release rate for each crack length is checked by using known solutions

in homogeneous materials. The error is less than 3%.

3. Results

3.1. Stress Concentrations

When a property mismatch exists in a system, edges and corners usually suffer high stress concentrations. The tensile and shear stresses in bonded Al_2O_3 and Nb under uniaxial tension in plane strain are shown in Fig.3-5(a) and (b). The interface tensile and shear stresses are similar to Bogy's calculation [22]. This high stress concentration decreases slowly in the ceramic normal to the interface. The resumption of uniform stresses occurs at a distance of about half the width, h.

The trend with the mismatch of elastic constants is shown in Fig.3-6(a) and Fig.3-6(b). The larger the mismatch, the larger is the stress concentration. Furthermore, the tensile stress concentration is much larger than the shear stress concentrations, indicating that mode I failure is preferred.

3.2. Stress Singularity

A pertinent form of the singular interfacial normal stress in the present system is

$$\sigma_{zz}^{i}/\sigma_{\infty} = Kr^{-\lambda} \tag{3-5}$$

where r=(h-y)/h. The proportionality constant K and the strength of singularity λ are functions of both geometry and material properties, as expressed by

$$K = f_1(d/h, \alpha, \beta) \tag{3-6}$$

$$\lambda = f_2(d/h, \alpha, \beta) \tag{3-7}$$

Remote from the edge, the tensile stress is rather uniform, in most cases, suggesting the simple form

$$\sigma_{zz}^{i}/\sigma_{\infty} = Kr^{-\lambda} \quad (r < r^{*}) \tag{3-8}$$

$$= A \qquad (r \geq r^{*}) \tag{3-9}$$

where r^{*} is the intersection of the two curves.

The exact value of λ in the present work is determined by fitting each stress distribution curve. The limiting case, $K \rightarrow 0$, and $\lambda \rightarrow 0$ should be reached when the thickness of metal layer becomes zero, with $A \rightarrow 1$ and $r^{*} \rightarrow 0$. An example of Al_2O_3/Au system with varying dimensionless thickness of metal interlayer is shown in Table 3-1.

Table.3-1.

Strength of edge singularities ($Kr^{-\lambda}$) for various metal thicknesses

d/h	K	λ	r^{*}
0.01	0.29	0.148	0.02
0.04	0.34	0.158	0.06
0.08	0.38	0.164	0.08
0.1	0.36	0.189	0.10
0.2	0.38	0.200	0.12
0.4	0.48	0.202	0.15
0.8	0.60	0.205	0.20

3.3. Strain Energy Release Rates

The stress concentrations that occur around the interface, near edges and corners, enhance the driving force on associated cracks. Strain energy release rates, calculated for small edge cracks, are required to assess the magnitude of

the effect. The important influence of the edge stress concentration is best revealed by plotting trends (with relative crack length, a/h) in the ratio of **G** for the bonded system to that for the homogeneous ceramic, $\mathbf{G}_h$. For this purpose, a quantity R is defined as

$$R = E^* \mathbf{G} / E_c \mathbf{G}_h \tag{3-10}$$

where E_c is the elastic modulus of the ceramic and

$$E_c \mathbf{G}_h = 1.12 \sigma_\infty^2 \pi a \tag{3-11}$$

Some typical results are plotted in Fig. 3-7. The solution for interface cracks between bonded planes reveals that R increases monotonically at small a/h, resulting in the singular form

$$R = (h/a)^n F(\alpha,\beta) + B(\alpha,\beta) \tag{3-12}$$

where the quantities n and F are tabulated in Table 3-2.

Table.3-2.

Edge fracture parameters for various material combinations

Materials	ν	G (GPa)	E^* (GPa)	α	β	n	F
Nb/Al_2O_3	0.39/0.25	38/147	163	0.554	0.154	0.237	0.667
Si/Al_2O_3	0.25/0.25	50/147	188	0.489	0.183	0.066	0.984
Cu/Al_2O_3	0.35/0.25	40/147	167	0.545	0.165	0.213	0.583
Al/Si	0.33/0.25	27/50	89	0.252	0.061	0.039	1.090
Al_2O_3	0.25	147	400	0.0	0.0	0.0	0.0

The strength of the singularity, n, increases as the mismatch in elastic properties (expressed by α and β) increases. Cracks in the ceramic adjacent to the interface also exhibit values of $R > 1$ (Fig.3-8). However, R decreases

rapidly with distance, z, from the interface. For small edge cracks in bonded metal strips, R increases with increase in the thickness d of the metal strip (Fig.3-9). Furthermore, for d<<h, R is independent of specimen width and varies only with a/d.

3.4. The Failure Stress

The strain energy release rates can be readily related to the failure strength by invoking eqn.(3-11) and eqn.(3-12) and by equating **G** and $\mathbf{G}_c$, whereupon

$$\sigma\,(1.12\pi/E\,\mathbf{G}_c)^{1/2}=[Ba+Fh^{n}\,a^{1-n}]^{-1/2} \tag{3-13}$$

For material combinations with n<1, the crack propagation stress decreases monotonically with increase in crack length, such that the fracture instability is indicated directly by eqn.(3-13) , (with a replaced by the initial crack length a_0). However, should material combinations exist with n>1, a stress maximum could develop upon crack propagation, given by ($d\sigma/da=0$)

$$\sigma_f=\left(\frac{E\,\mathbf{G}_c}{1.12\pi}\right)^{1/2}\left[\frac{(n-1)^{1-1/n}}{nhF^{1/n}B^{1-1/n}}\right]^{1/2} \tag{3-14}$$

occurring at a crack length,

$$a_m=h\,[F\,(n-1)/B\,]^{1/n}. \tag{3-15}$$

For such materials, the fracture strength σ_f is independent of initial crack size, (at least when $a_0<a_m$) and fracture is preceded by stable crack extension.

4. Remarks

The present work has emphasized the stress fields normal to the interface. The shear stress, which is relatively small, has been ignored especially in evaluating the strain energy release rate. Other loading conditions would require incorporation of shear effects and their interaction with tensile loads. Furthermore, singular stresses only exist in the linear elastic calculation. When metal plasticity is involved, the singular stresses are prohibited. The edge stress concentrations are then controlled by the yield strength of the metal. Therefore, edge dominated failure only occurs in systems consisting of high yield strength metals or low strength ceramics. Failure in a porous ceramic close to the interface has been reported by Pabst et al. [33], while failure at the interface or in the ceramic has been reported by Twentyman et al. [31].

When the edge stress is important, the property mismatch and the geometry, d/h, are important. Reduction of the edge stress concentration can be achieved by using a thin metal layer or multilayers with property gradients.

Figure Captions

Fig.3-1

An illustration of the crack closure integral method.

Fig.3-2

An illustration of the finite element grid and the corresponding notations around the crack tip for explaining the use of virtual crack extension technique.

Fig.3-3

A typical finite element grid for a system having a singular point for evaluating stress fields around it. (a) the whole system, (b) fine mesh around the singular point.

Fig.3-4

A typical finite element grid near crack tip for evaluating strain energy release rate by the virtual displacement method.

Fig.3-5

Finite element calculations of stress concentrations generated at edges in an edge bonded strip of metal and ceramic, (a) normal stresses, and (b) shear stresses at or near the interface in an Al_2O_3/Nb bonded system.

Fig.3-6

Finite element calculations of stress concentrations generated at the interface, (a) normal stresses, and (b) shear stresses for bonded systems with various property mismatch.

Fig.3-7

The strain energy release rates for interface cracks between various materials.

Fig.3-8

Strain energy release rates for small cracks in the ceramic adjacent to the interface.

Fig.3-9

Strain energy release rates for small cracks adjacent to the interface of bonded strips.

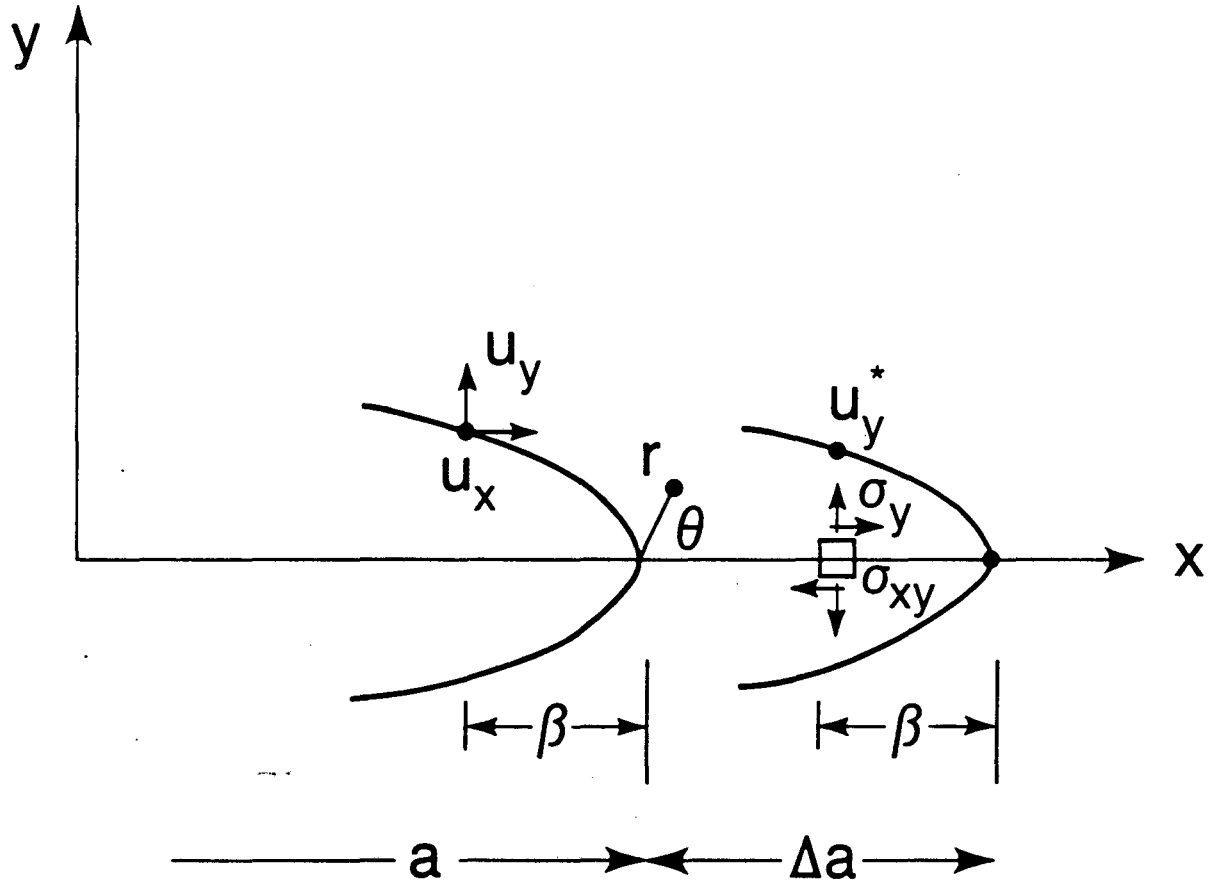

XBL 873-6213

Fig.3-1

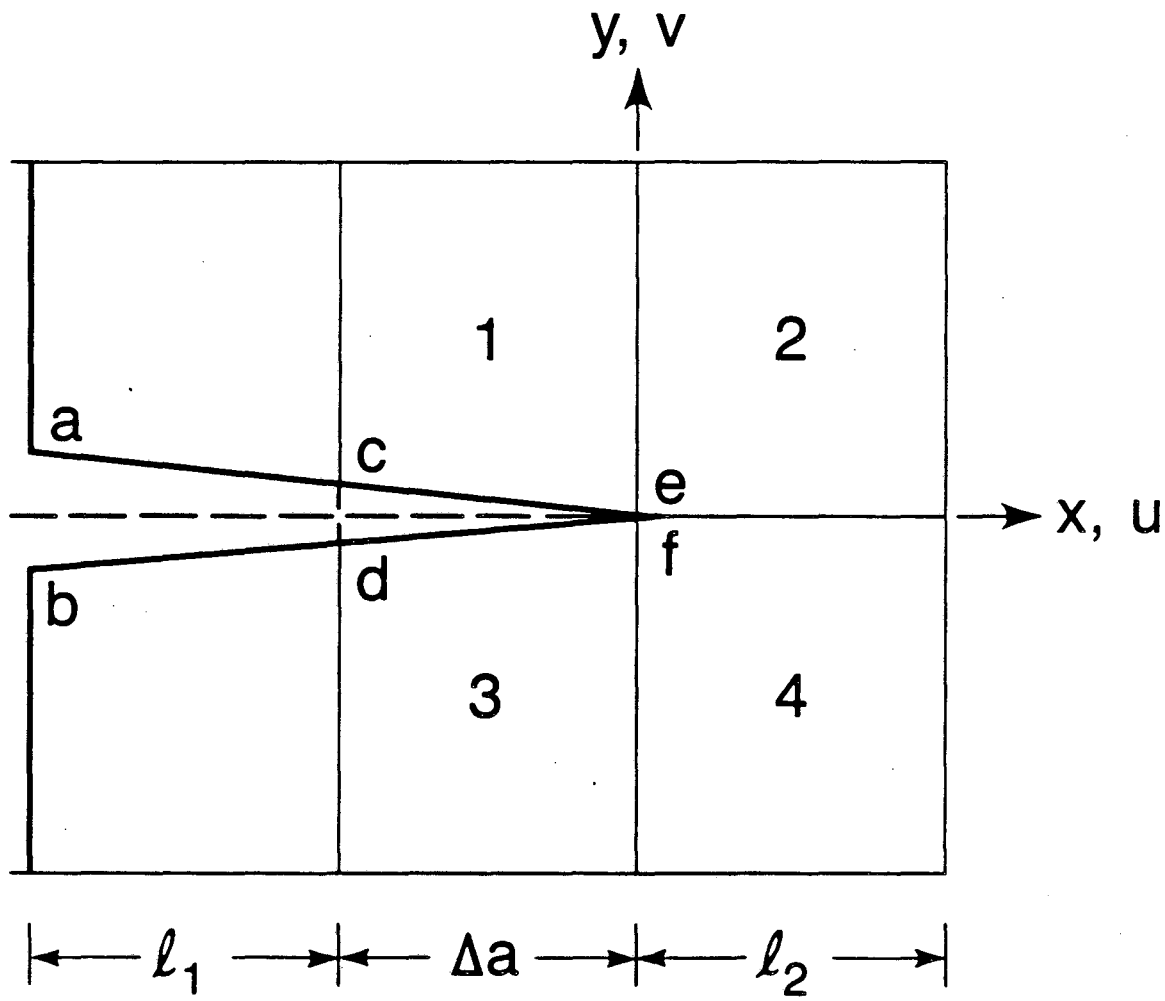

XBL 873-6224

Fig.3-2

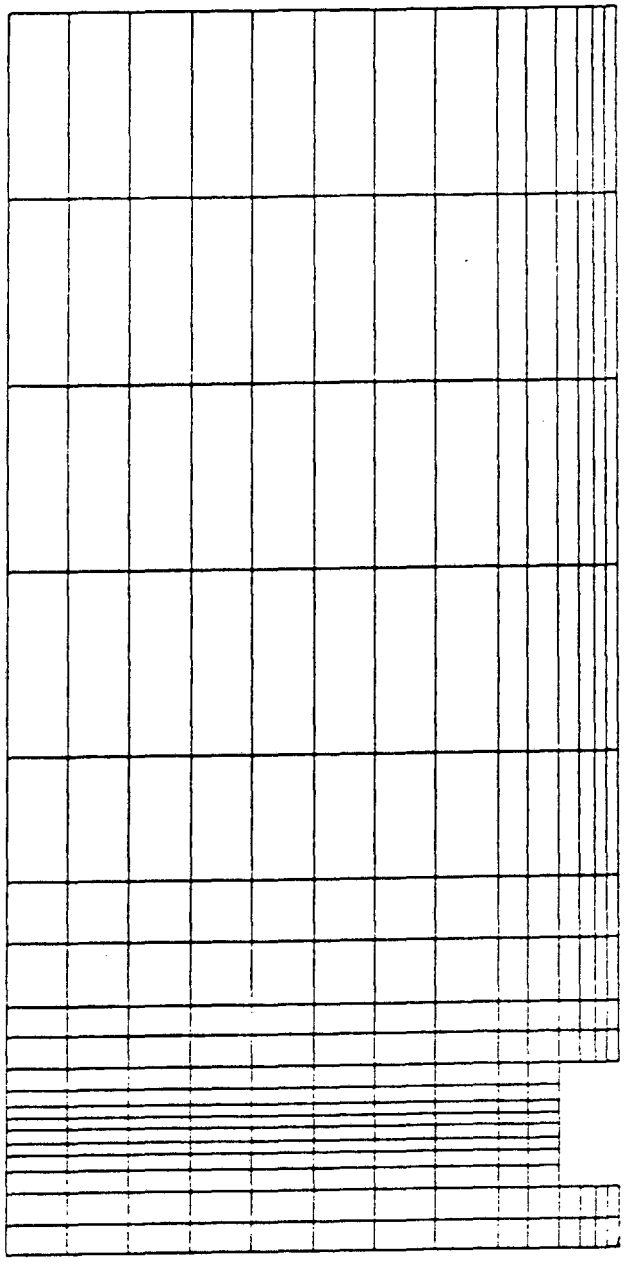

Fig.3-3(a)

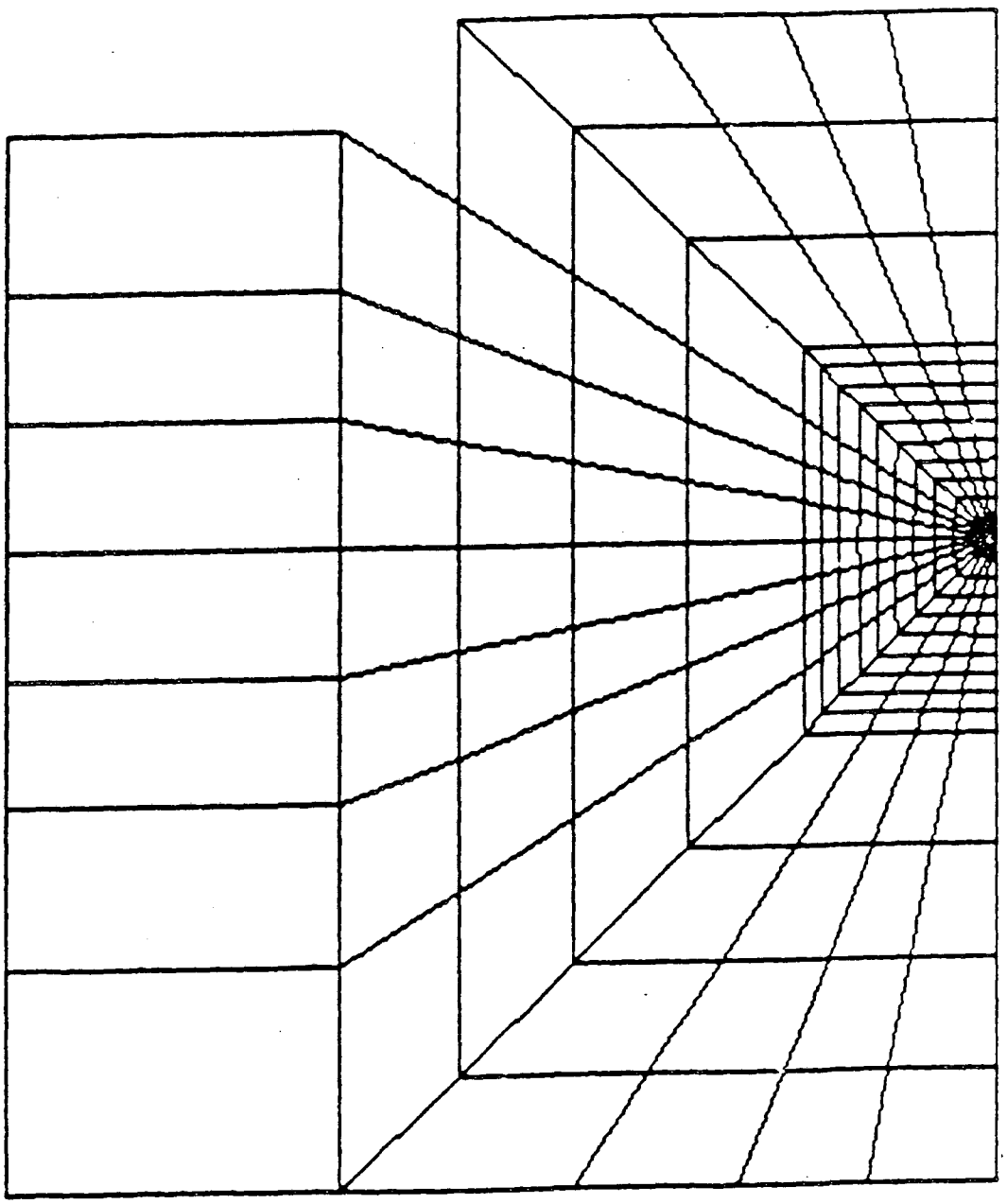

Fig.3-3(b)

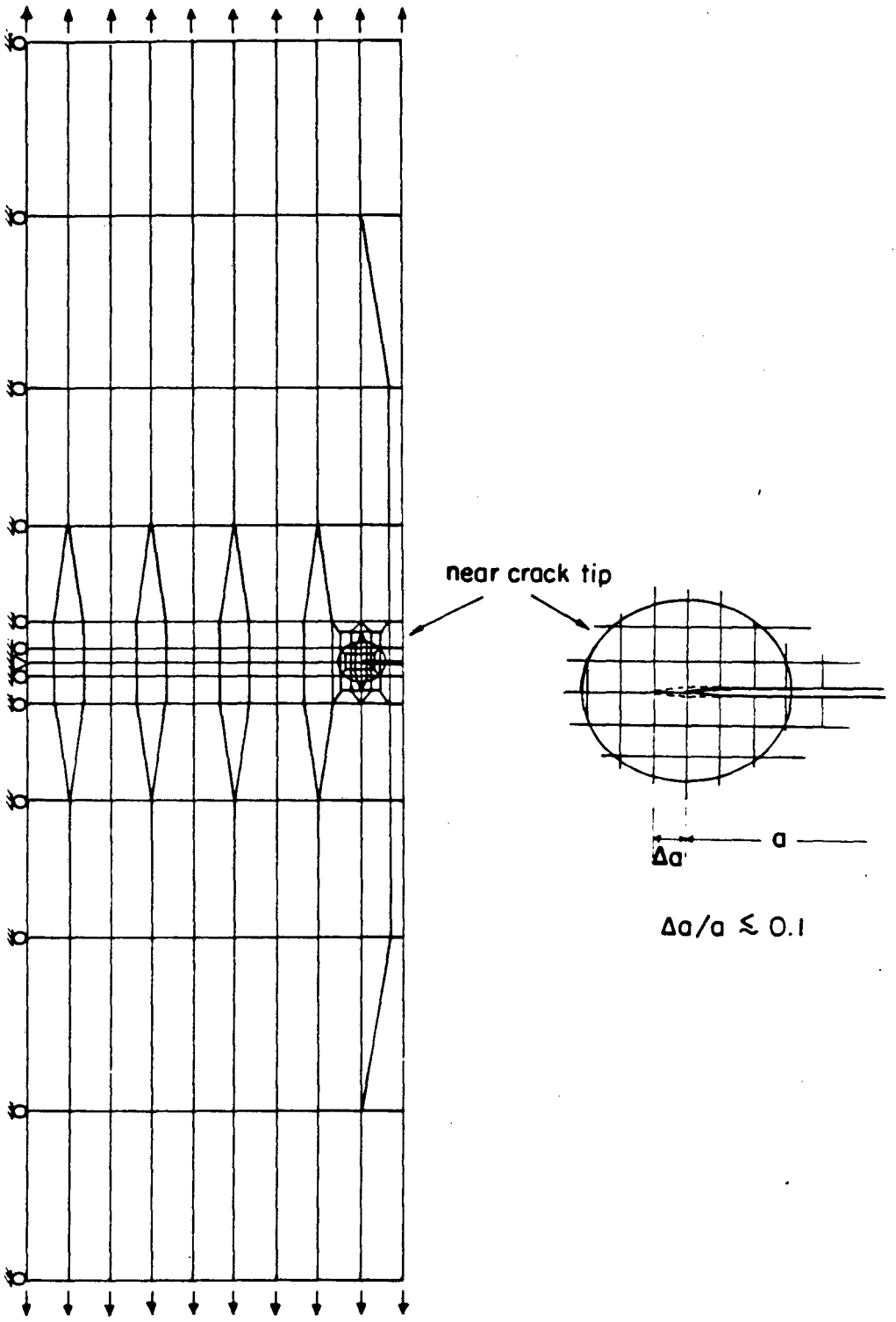

XBL857-6426

Fig.3-4

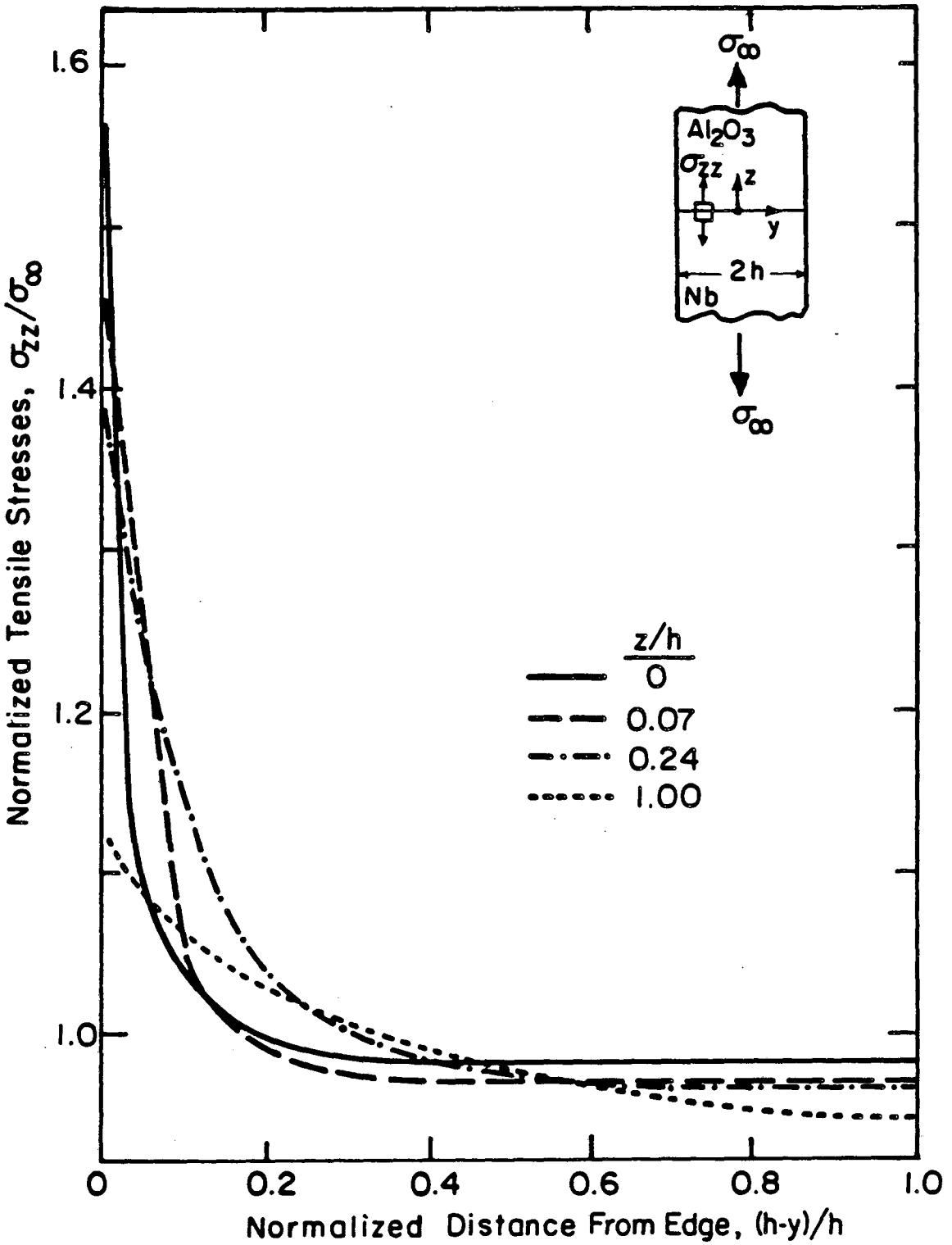

XBL 857-6430

Fig.3-5(a)

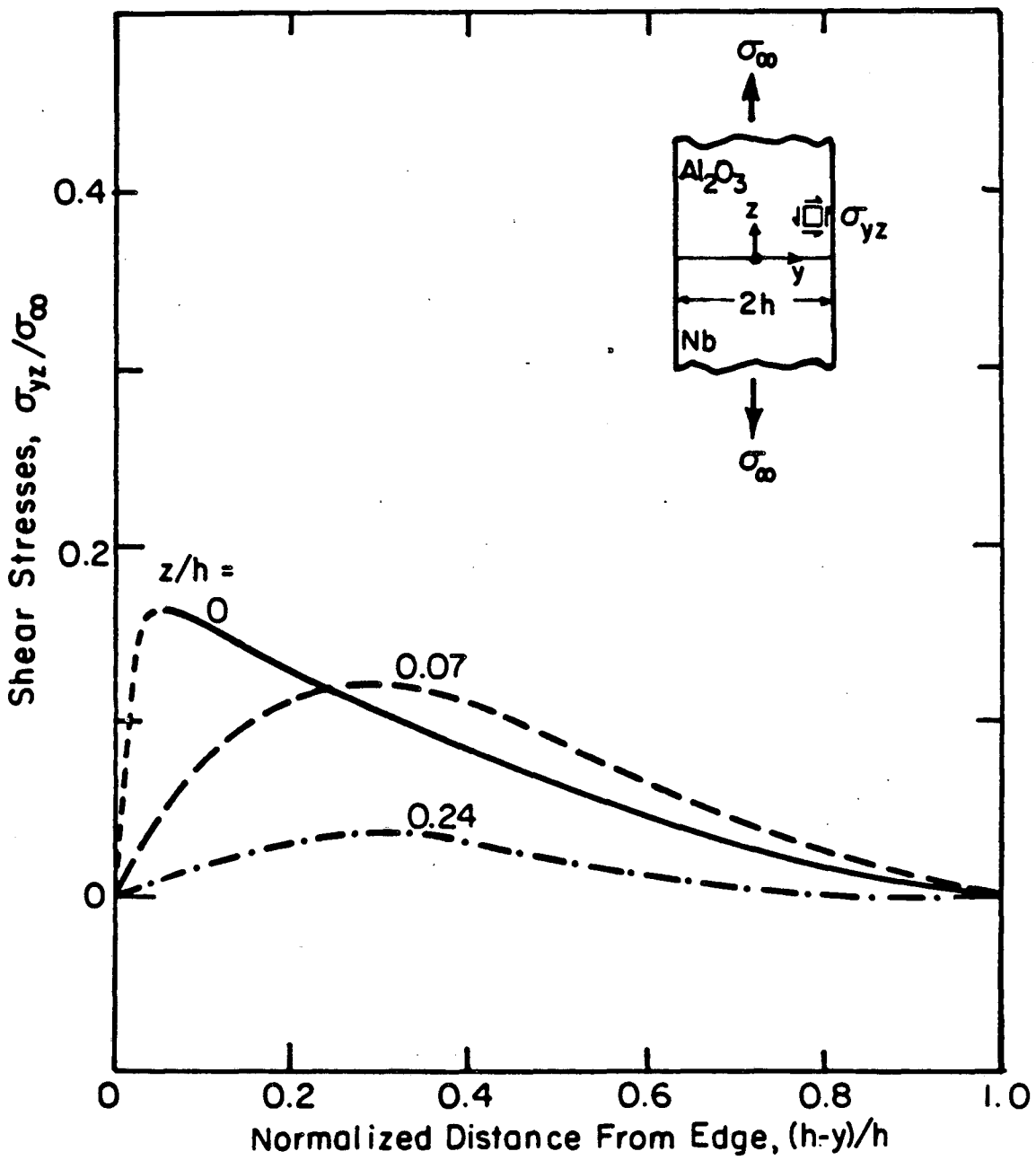

XBL857-6425

Fig.3-5(b)

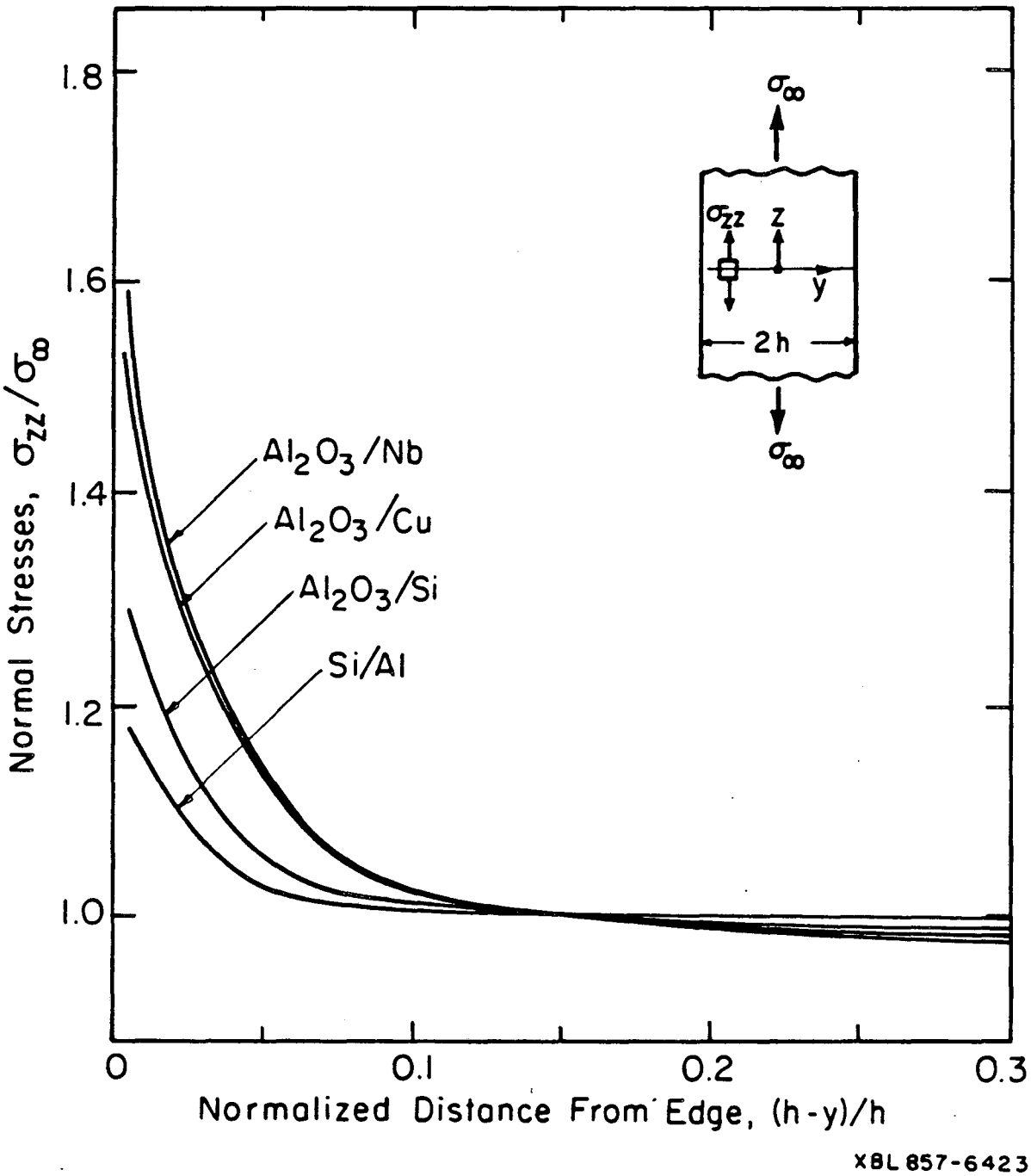
1.8
1.6
1.4
1.2
1.0
Normal Stresses, $\sigma_{zz}/\sigma_\infty$
Al_2O_3/Nb
Al_2O_3/Cu
Al_2O_3/Si
Si/Al
σ_∞
σ_{zz}
z
y
2h
σ_∞
0
0.1
0.2
0.3
Normalized Distance From Edge, (h-y)/h
XBL 857-6423

Fig.3-6(a)

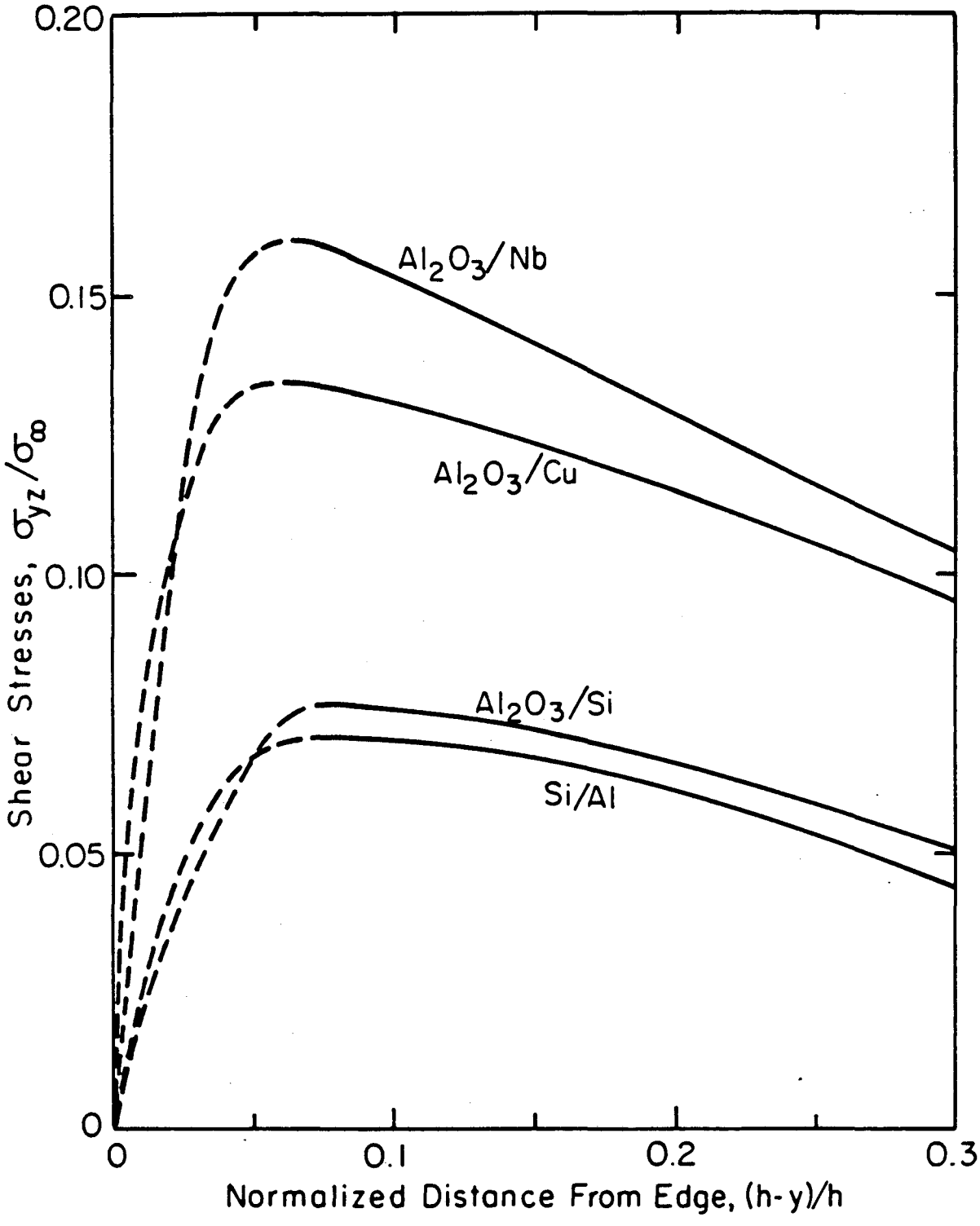

XBL 857-6424

Fig.3-6(b)

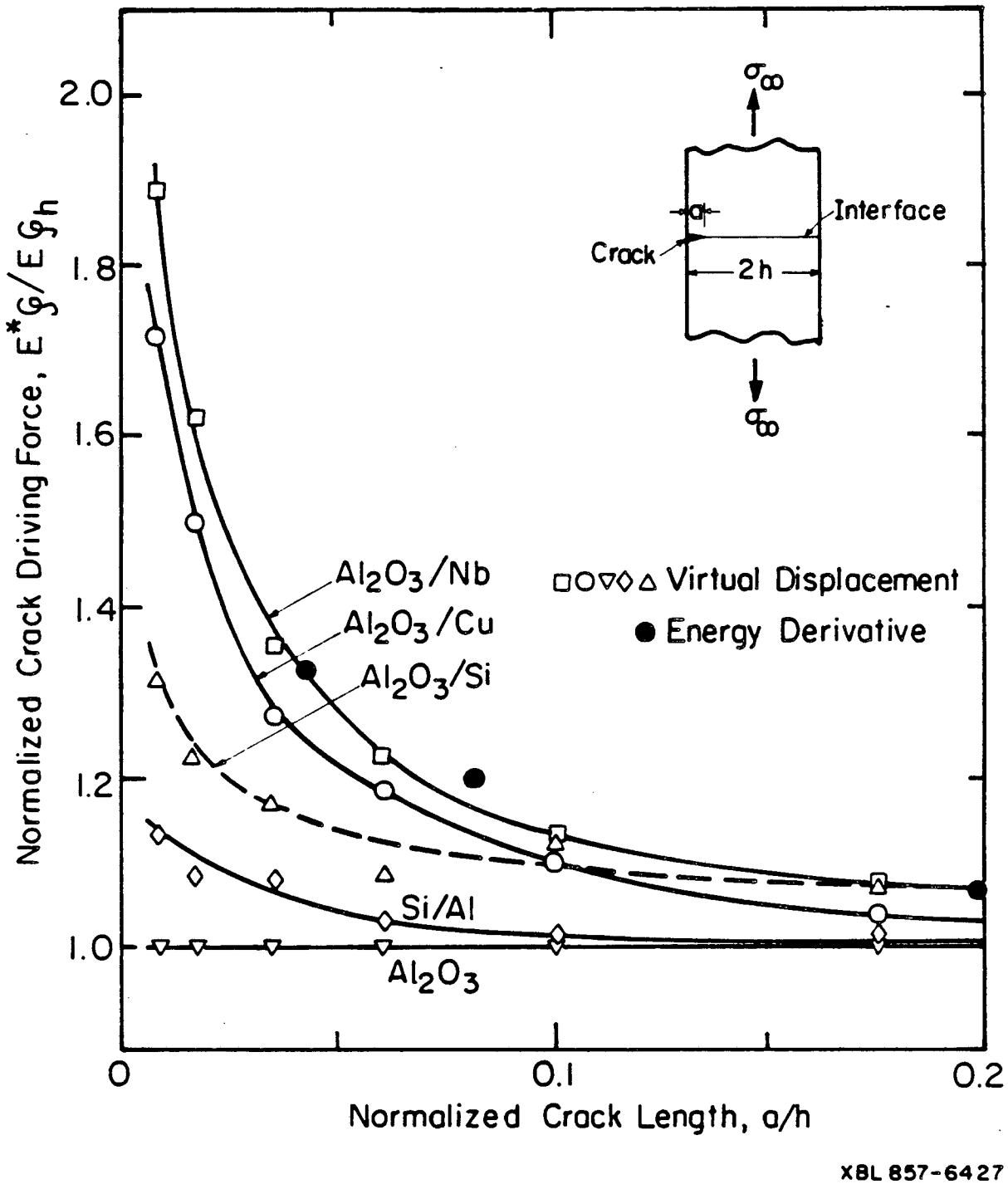

XBL 857-6427

Fig.3-7

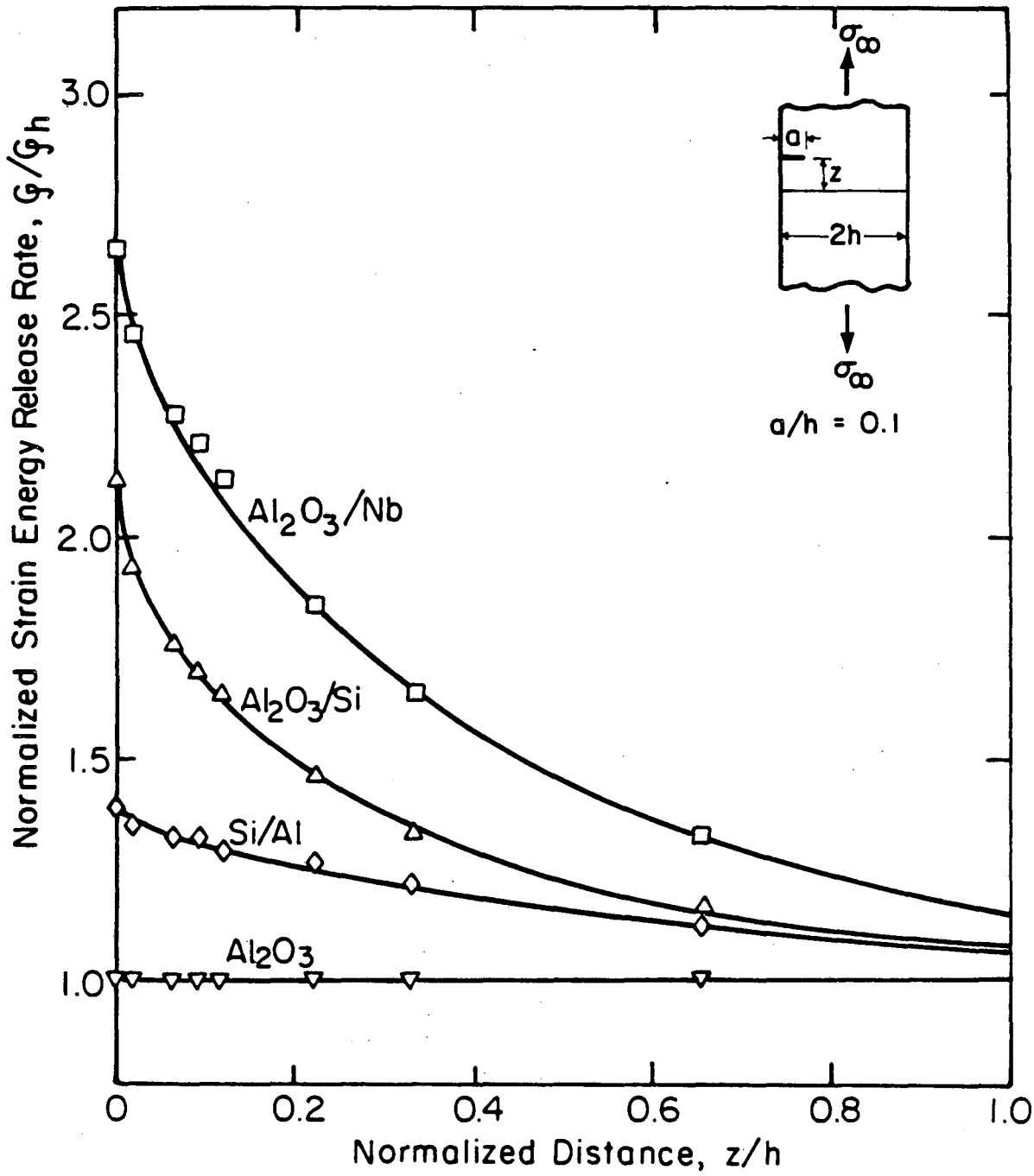

XBL 857-6428

Fig.3-8

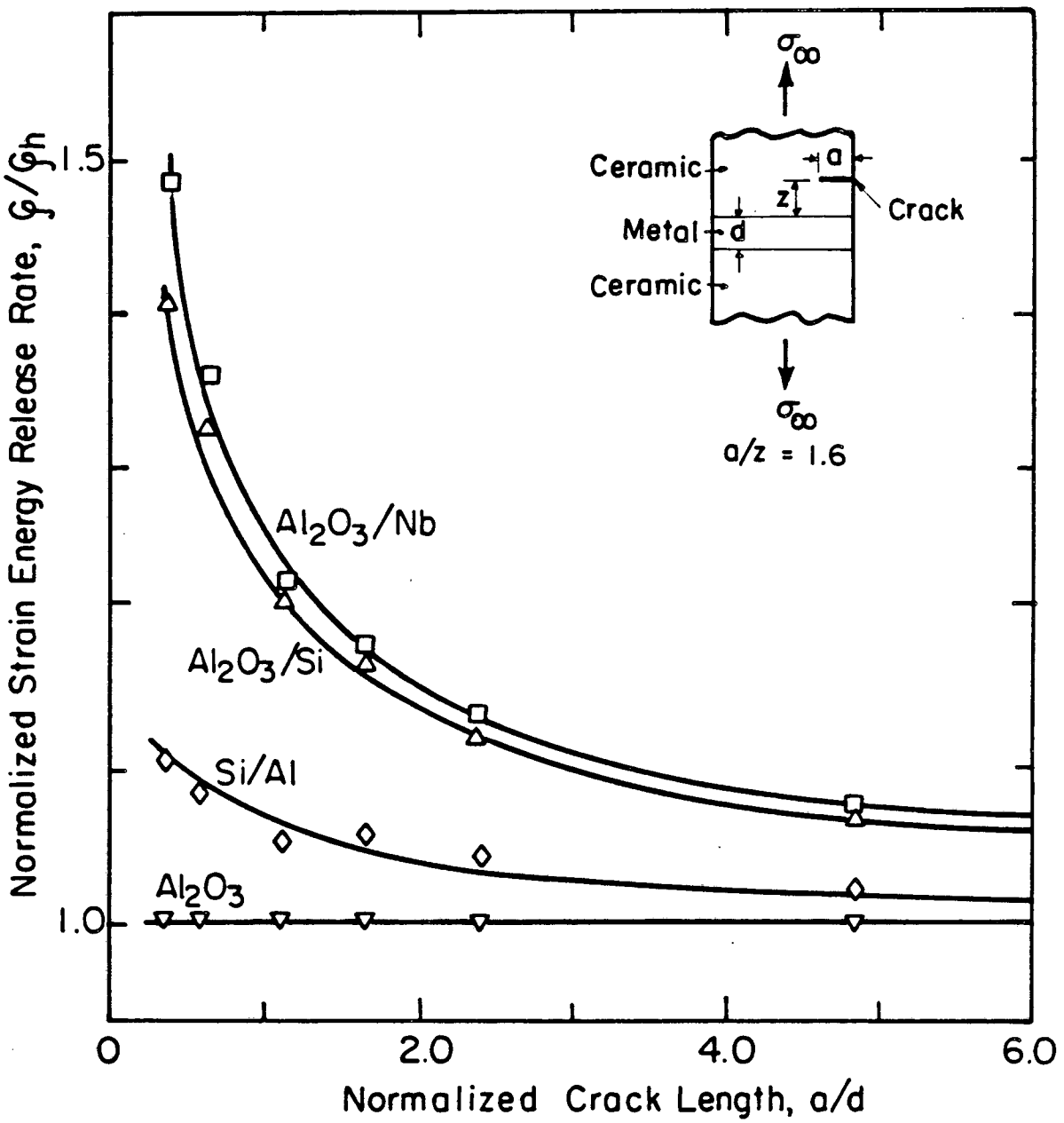

XBL857-6429

Fig.3-9

CHAPTER 4

MECHANICAL BEHAVIOR UNDER ELASTIC-PLASTIC CONDITIONS

1. Introduction

The stress concentrations that arise when the metal has elastic characteristics have been studied in the previous chapter. These studies revealed that singular stresses exist at the free surface and that the strength of the singularity depends upon the elastic mismatch as well as the geometry. Consequently, plastic deformation inevitably occurs within the singular field and the elastic calculations have restricted utility. Elastic/plastic behavior of the metal strip is thus emphasized in the present study.

The edge stresses are no longer infinite, due to yielding, and the stress maximum translates toward the center The dominant failure mechanism is then dictated by such properties as the flow stress of the metal, the metal layer thickness and the elastic properties of both materials, as well as the flaw distributions in the ceramic, and at the interface.

Slip line solutions provide insights regarding the expected trends, while finite element analysis establishes detailed characteristics. The Prandtl field and limit load revealed by the slip line solution in a rigid plastic material are briefly described as background [61], and the finite element procedures are then explained. The results lead to a prediction of those property/geometry characteristics that optimize the mechanical strength.

The effect of metal plasticity not only prohibits the singular stress but also can blunt the interface crack. The stress fields and the plastic zone sizes are studied at the vicinity of a single edge interface crack. These stress fields in conjunction with the fracture toughness at the interface dictate crack propagation, which is also affected by the thickness of the metal interlayer.

2. Limit Load

2.1. Slip Line Solution

For a rectangular block of plastic-rigid material bonded between rigid parallel plates with a tensile load applied, plastic zones initiate at the edges and spread inwards. The plastic zones first meet in the center of the block, with a zone near the middle still rigid. The associated slip line field, in conjunction with the interfacial tensile stress are shown in Fig.4-1. The external plastic-rigid boundary passes through the edges, intersecting the horizontal axis of symmetry at 45° . Considerations of the equilibrium around the edge then dictate that the mean normal stress be equal to shear yield strength (k , or $\frac{1}{2}Y_0$) along OA. The mean tensile stress on OB is thus $k(1+\frac{\pi}{2})$. This is also the value of the normal tensile stress acting on the interface. The stress distribution in the center is more difficult to predict. When the ratio of thickness to width is between 0.01 and 0.8, the tensile stress as well as the corresponding pressure distribution can be obtained from the slip line field (Fig.4-1). However, since the state of stress within the rigid wedge is unknown, only the average tensile stress between the interface and the wedge can be obtained.

The average pressure P is;

$$\frac{P}{Y_0}=\frac{3}{4}+\frac{h}{4d} \tag{4-1}$$

where d' is the deformed thickness. This pressure dictates the limit load for a perfectly plastic metal bond.

2.2. Finite Element Procedure

One material couple chosen as reference has the material properties, $\nu_c = 0.25$, $E_c = 400{,}000$ MPa and $Y_0 = 100{,}000$ MPa for the ceramic and $\nu_m = 0.4$, $Y_0/E_m = 1/670$, and $E_m/E_c = 0.25$ for the metal, in order to approximately simulate the Al_2O_3/Nb system. The other couple simulates Al_2O_3/Au , and has the metal properties, $Y_0/E_m = 1/615$, and $E_m/E_c = 5$. Plane strain, isoparametric quadrilateral elements are used in the present analysis. The nonlinear problem is linearized by specifying small load increments and iterating within each increment for good convergence. Displacement boundary conditions are chosen in order to facilitate convergence.

For perfectly plastic material, the tangent stiffness finite element solution exhibit too stiff a response in the fully plastic range. This makes the solution often exceed the limit load by substantial amounts, and in some cases have no limit load at all. It is shown that incremental deformation fields are highly constrained at or near the limit load, causing inaccuracy [62]. Three approaches reduce this inaccuracy. A special mesh configuration is designed based on the slip line field, in order to release the excess constraints. A variational principle for mixed field approximation [63] is used to separate the deviatoric and dilatational strain increments.

2.3. Elastic/Plastic Solutions

An estimation of plastic zone size along the interface in small scale yielding is obtained from the elastic field. The elastic stresses normal to the interface σ_{zz}^{i} are described by Eq.(3-8) as

$$\sigma_{zz}^{i}/\sigma_{\infty} = K\ r^{-\lambda}+A \tag{4-2}$$

where K , λ, and A are functions of d/h and of the elastic properties (Table.3-1). Consequently, since σ_{zz} at the edge in a non-hardening system is limited to $(Y_0/2)(1+\pi/2)$, the extent of the plastic zone along the interface, r_p , in small scale yielding (Fig.4-2) is of the order,

$$r_p = (K\sigma_{\infty} \ / \ [\ (Y_0/2)(1+\pi/2) - A\ \sigma_{\infty}\ ]\ )^{1/\lambda} \tag{4-3}$$

As the Von-Mises yield criterion is chosen in the present work, the corresponding shape of the plastic zone should reflect trends in the equivalent stress with orientation θ about the interface plane. The elastic equivalent stress σ_e is thus evaluated for the Al_2O_3/Nb system (Fig.4-3) in order to compare with the results from the elastic- plastic calculation. The plastic zones derived from finite element calculation (Fig.4-4) are in reasonable agreement with those predicted from the elastic equivalent stresses.

Subsequently, extension of the plastic zones meet at the center and spread inwards. The side wedges are the last regions to be plastic deformed. The growth of the plastic zones and the rate of deformation determines the engineering stress-strain curve. A representative engineering stress-strain curve (Fig.4-5) with d/h =0.2 can apparently be divided into three regions. In the first region, small scale yielding conditions prevail and the system is linear. When the plastic zones from both edges meet at the center, small scale yielding is no longer applicable and a deviation from linearity initiates. Subsequently, the entire metal strip yields, leading to a limit load.

Full numerical solutions for the elastic/plastic stresses have again been obtained for the material combination Al_2O_3/Nb , but are then generalized based on comparisons with the slip line field and elastic solutions. Engineering

stress-strain curves with different d/h (Fig.4-6) show that the limit load is in very good agreement with that predicted from the slip line field. Consequently, an effective criterion for plasticity limited failure can be indicated by Eq.(4-1), at least when the elastic modulus of the metal is smaller than that of the ceramic (typical of most metal/ceramic combinations of practical interest). It is also noted that the plastic strain at saturation ϵ_p^s varies inversely with the relative metal layer thickness

$$\epsilon_p^s = 3h / d \tag{4-4}$$

This result can be used in conjunction with Eq.(4-1) to provide a reasonable estimation of the stress-strain behavior expected for a wide range of layer thickness and yield strength levels.

Normal stresses along the interface have also been determined for the same material combination (Al_2O_3/Nb), as plotted on Fig.4-7. For the fully plastic limit, the computed result agrees closely with the slip line solution. Also, for the small scale yielding region, the stresses are closely simulated by truncating the elastic solution at $r = r_p$. However, at intermediate loads, the stress field is relatively complex and not readily derived from either the elastic or fully plastic solutions.

The interfacial normal stress fields for the material combination Al_2O_3/Au system with various d/h are shown in Fig.4-8-10. The comparison of Fig.4-7 and Fig.4-9 reveals the effect of property mismatch in the small scale yielding region.

3. Plastic Deformation around an Interface Crack

A calculation of the plastic zone size for Au bonded to Al_2O_3 is shown in Fig.4-11. In small scale yielding, the shape of the plastic zone resembles that

of the homogeneous material, but the angles of the maximum extension of the plastic zone are changed. When this maximum extension reaches the other side of the metal layer, the plastic zone starts to spread towards the edges. A comparison of the plastic zones in homogeneous material and bonded material is shown in Fig.4-12 . The plastic zone in the bonded system is apparently smaller than that of the homogeneous material.

3.1. Stress Fields Around The Crack Tip

Contours of the maximum principal stress are shown in Fig.4-13 for different load levels. In small scale yielding (Fig.4-13(a)), the asymmetrical stress field is apparently caused by the mismatch of the material properties. However, when the load levels are increased, the degrees of the asymmetry increase substantially. The reduction of the stress concentrations at the crack tip is revealed by the tensile stress fields normal to the interface (Fig.4-14).

4. Concluding Remarks

The thickness of metal interlayer is important in both the strength of the singularity and the plasticity induced limit load. The reduction of the strength of the singularity is apparently caused by the increase of the constraint from the ceramic. This smaller strength of the singularity reduces the corresponding size of the plastic zone in small scale yielding. Similarly, the constraints at the sides of metal retard the growth of the plastic zone, and consequently, the corresponding limit load is increased.

The edge dominated failure described in chapter 2 can be eliminated by plastic deformation in the metal. Furthermore, a specific magnitude exists for the maximum value of the stress concentration. This makes the estimation of edge effects straightforward.

A low yield strength metal blunts the crack at the interface when the interfacial strength is relatively strong. The plastic zones are also different for the homogeneous material and the bonded material even when the applied stress intensity factors are the same. This implies that the plastic zone size is strongly affected by the corresponding stress fields at the crack tip and thus by the geometry indirectly.

Figure Captions

Fig.4-1.

A slip line field in the metal interlayer in junction with the interfacial normal stress predicted by Prandtl stress field.

Fig.4-2.

Interfacial normal stress fields under different load levels in small scale yielding region and the corresponding plastic zone size along the interface.

Fig.4-3.

The contours of effective stress fields with different values of effective stress to applied stress, σ_e / σ_∞, The parameter σ_∞ / Y_0 is the predicted applied load to have the corresponding plastic zone.

Fig.4-4.

The growth of the plastic zones from the singularty point at a bonded edge.

Fig.4-5.

The engineering stress-strain curve in conjunction with the corresponding plastic zones; small scale yielding in the linear elastic region, large scale yielding in the 'harding' region, and the fully plastic deformation in saturation region.

Fig.4-6.

Engineering stress-strain curve for various thickness of metal interlayer, d/h. The asymptomic values from slip line field are indicated for comparison.

Fig.4-7.

The interfacial normal stresses under different load levels for material combination Al_2O_3/Nb with d/h = 0.2. The dashed line is the interfacial normal stress predicted from slip line field.

Fig.4-8.

The interfacial normal stresses under different load levels for material combination Au/Al_2O_3 with d/h= 0.01.

Fig.4-9.

The interfacial normal stresses under different load levels for material combination Au/Al_2O_3 with d/h =0.2.

Fig.4-10.

The interfacial normal stresses under different load levels for material combination Au/Al_2O_3 with d/h = 0.8.

Fig.4-11.

(a) An illustration of the model system for calculation of the stress fields and the plastic zone around an interface crack. (b) The mesh configuration around an interface crack tip in the region outlined by dashed lines in (a). (c) The growth of the plastic zones around the crack tip.

Fig.4-12.

The comparison of the plastic zone sizes between nomogeneous material, Au, and a bonded material, Al_2O_3/Au, under the same loading condition..

Fig.4-13.

The contours of the maximum principal stress, σ_1/σ_∞ at the vinicity of an interface crack under different load levels. (a) $\sigma_\infty/Y_0 = 0.04$, (b) σ_∞/Y_0

$= 0.28$, and (c) $\sigma_\infty / Y_0 = 0.4$.

Fig.4-14.

The interfacial normal stresses at the vinicity of an interface crack tip under different load levels for the material combination Al_2O_3/Au.

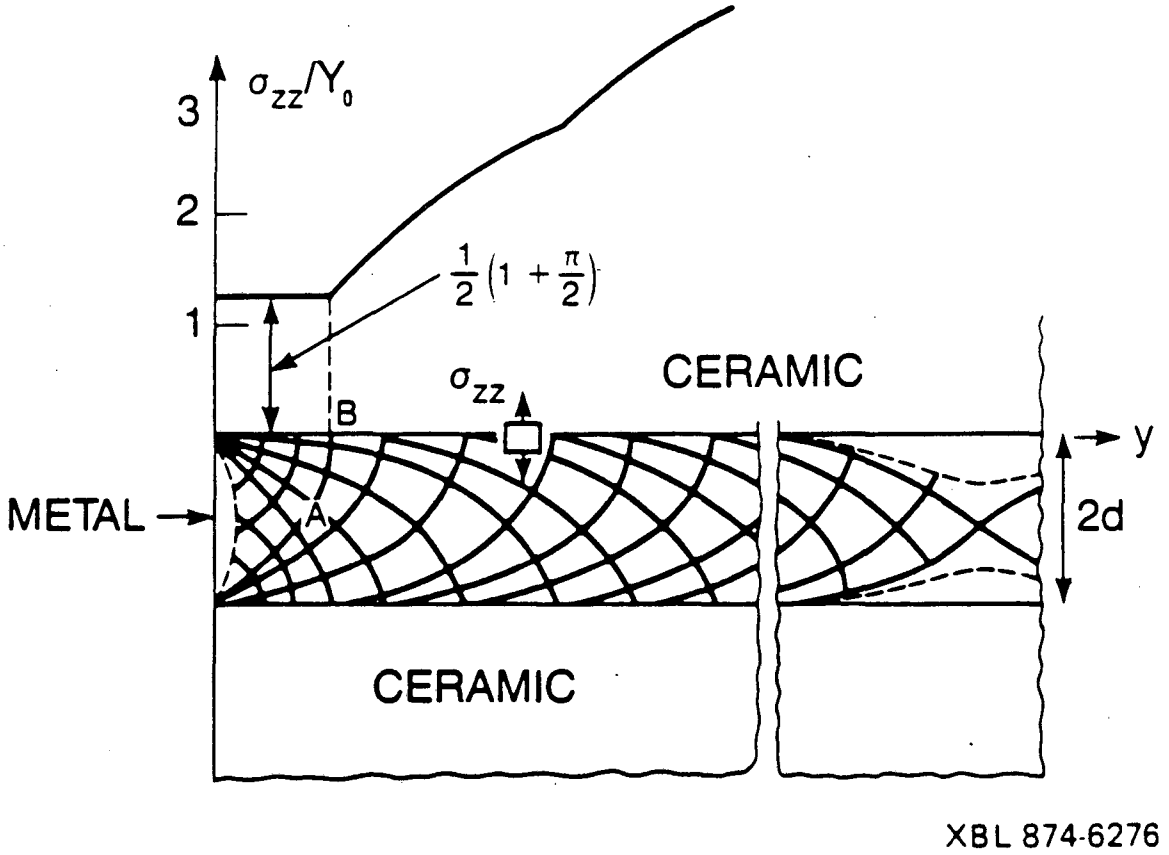
σ_{zz}/Y_0
3
2
1
$\frac{1}{2}\left(1+\frac{\pi}{2}\right)$
σ_{zz}
CERAMIC
B
A
METAL
y
2d
CERAMIC
XBL 874-6276

Fig.4-1

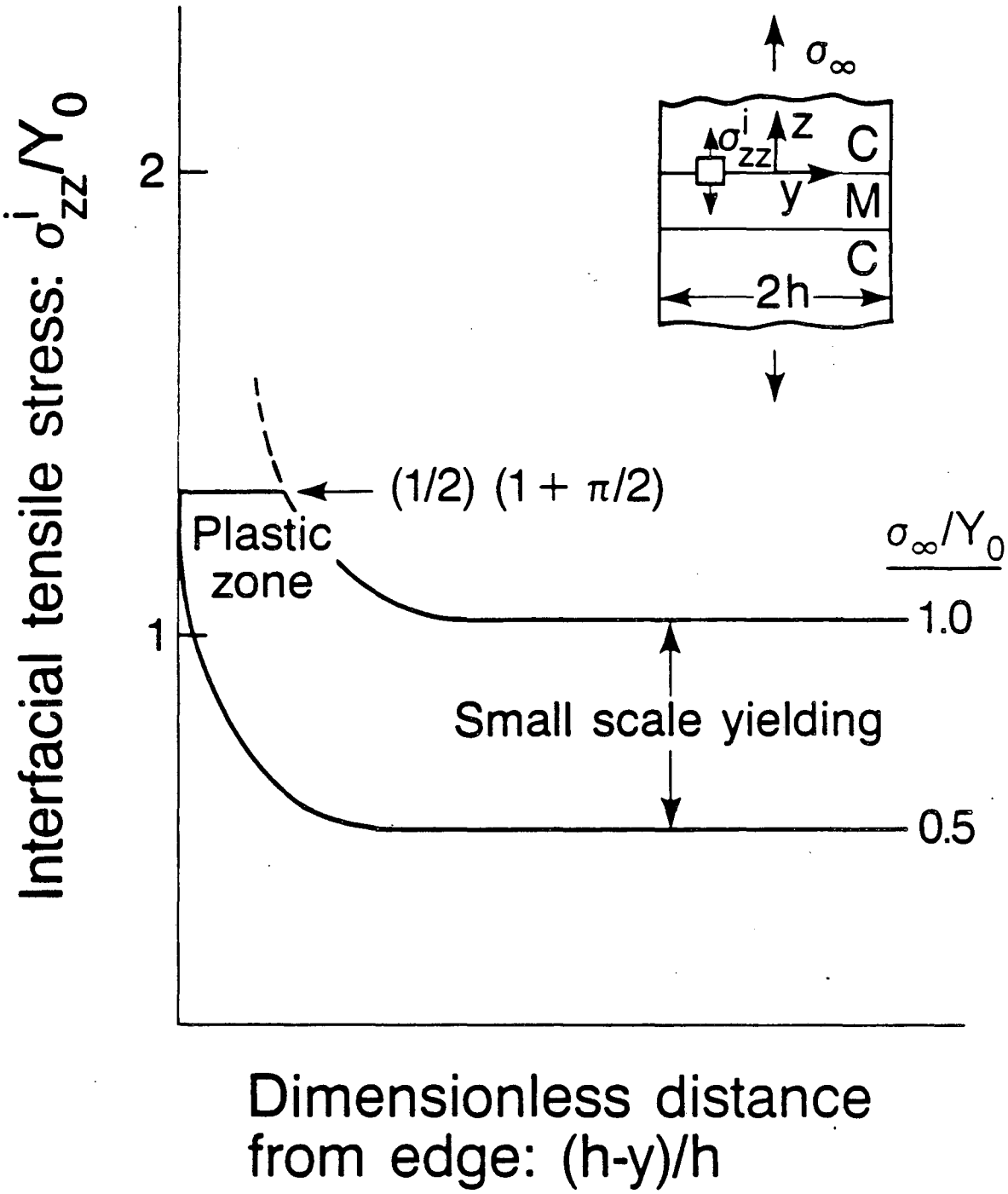

XBL 873-6212

Fig.4-2

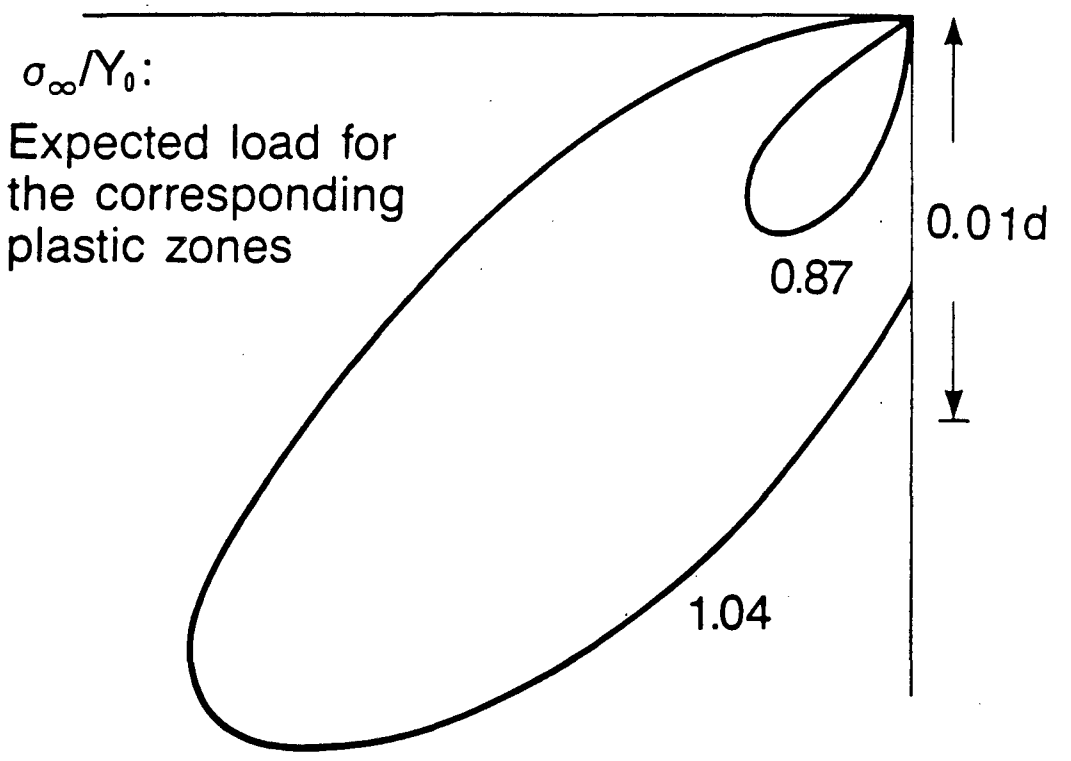

XBL 874-6281

Fig.4-3

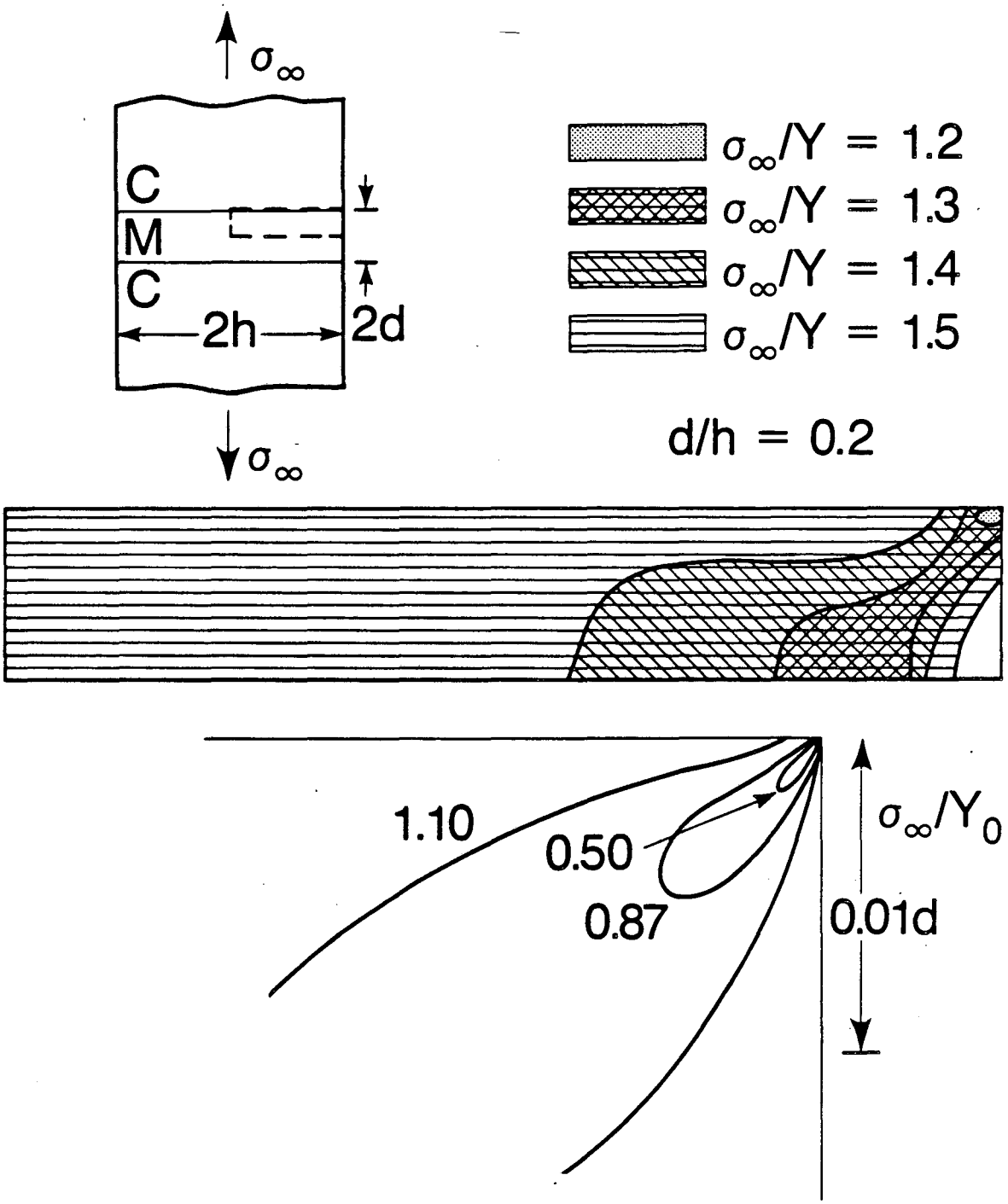

XBL 873-6210

Fig.4-4

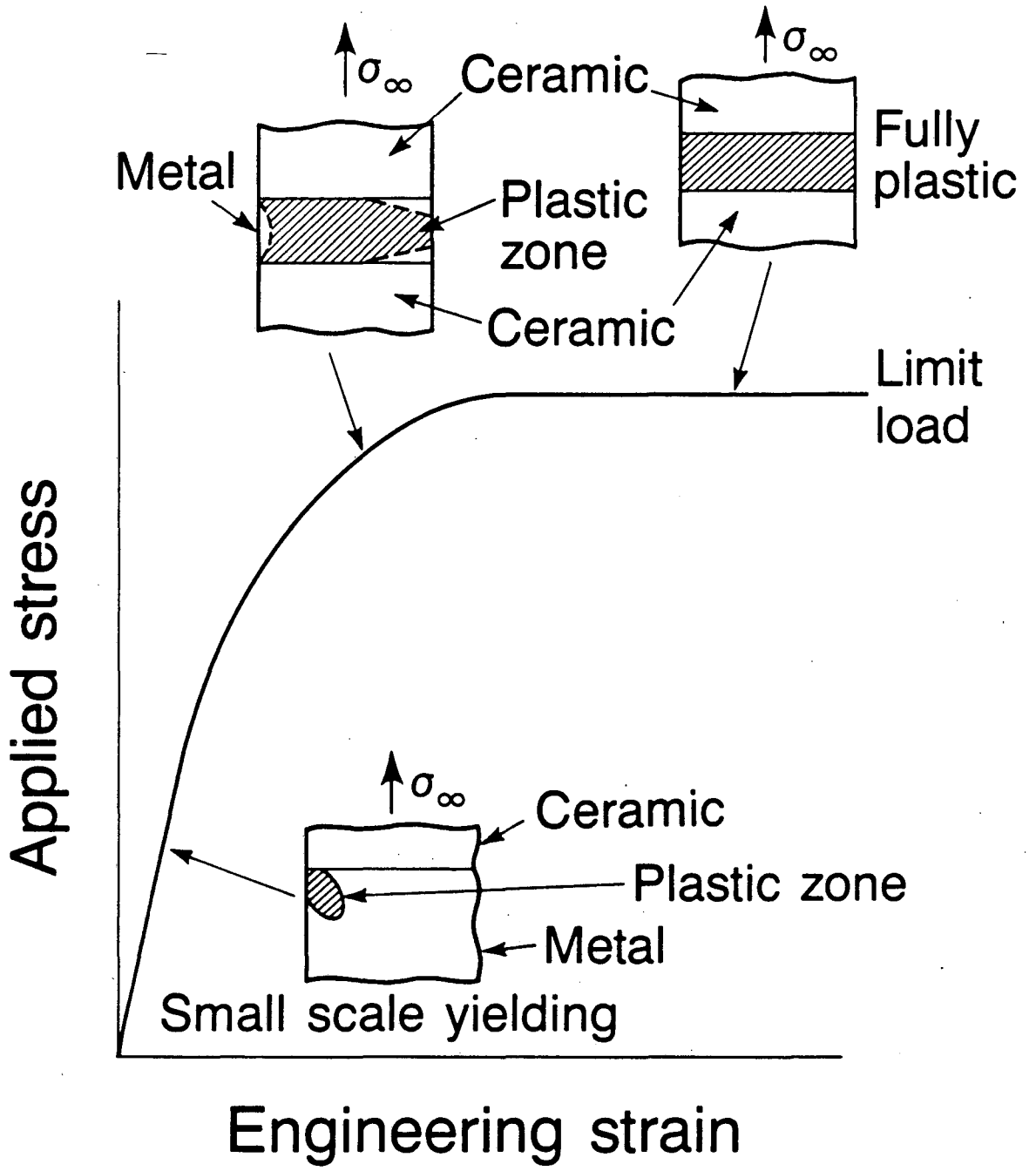

XBL 873-6211

Fig.4-5

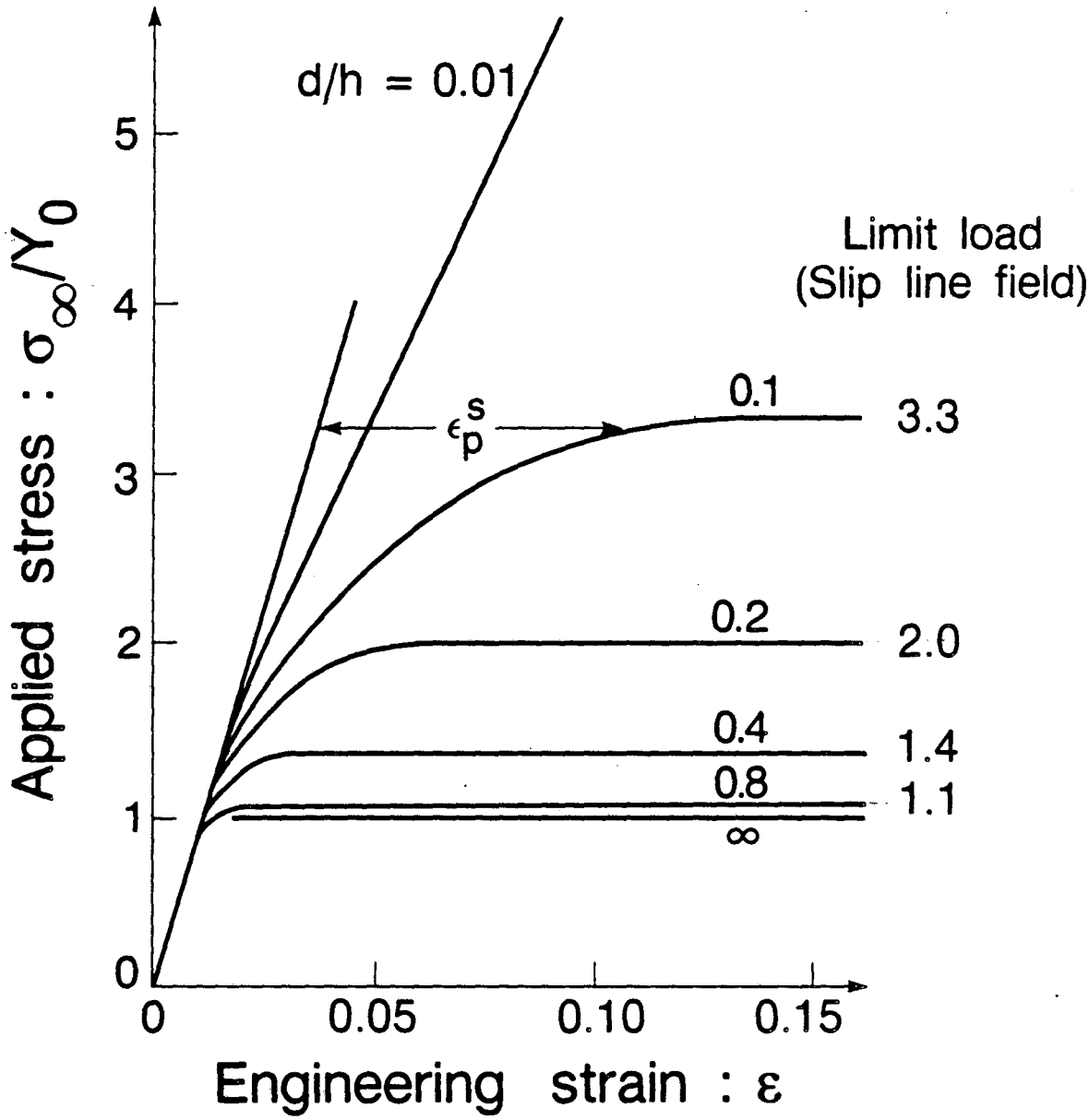

XBL 873-6223

Fig.4-6

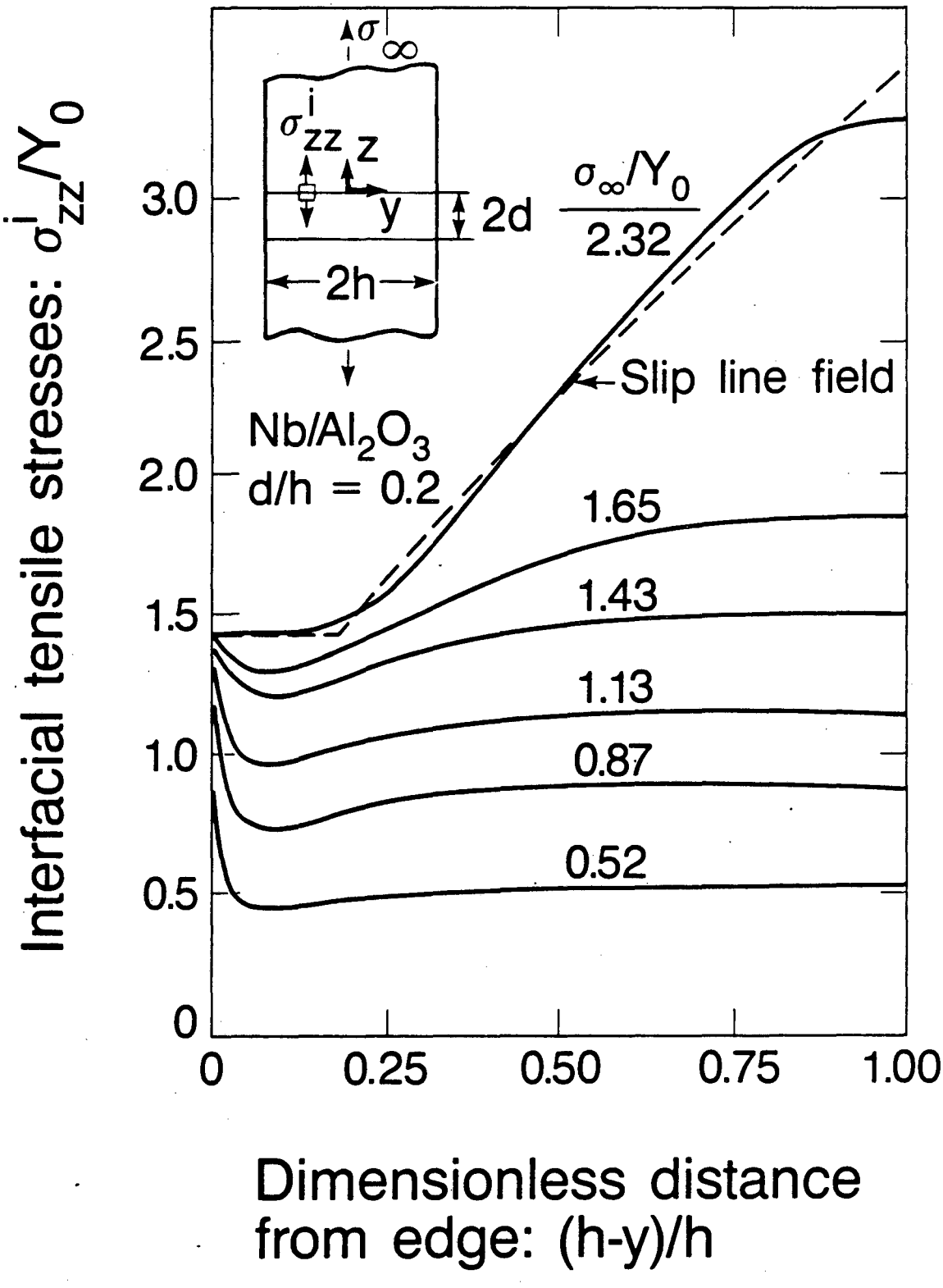

XBL 873-6215

Fig.4-7

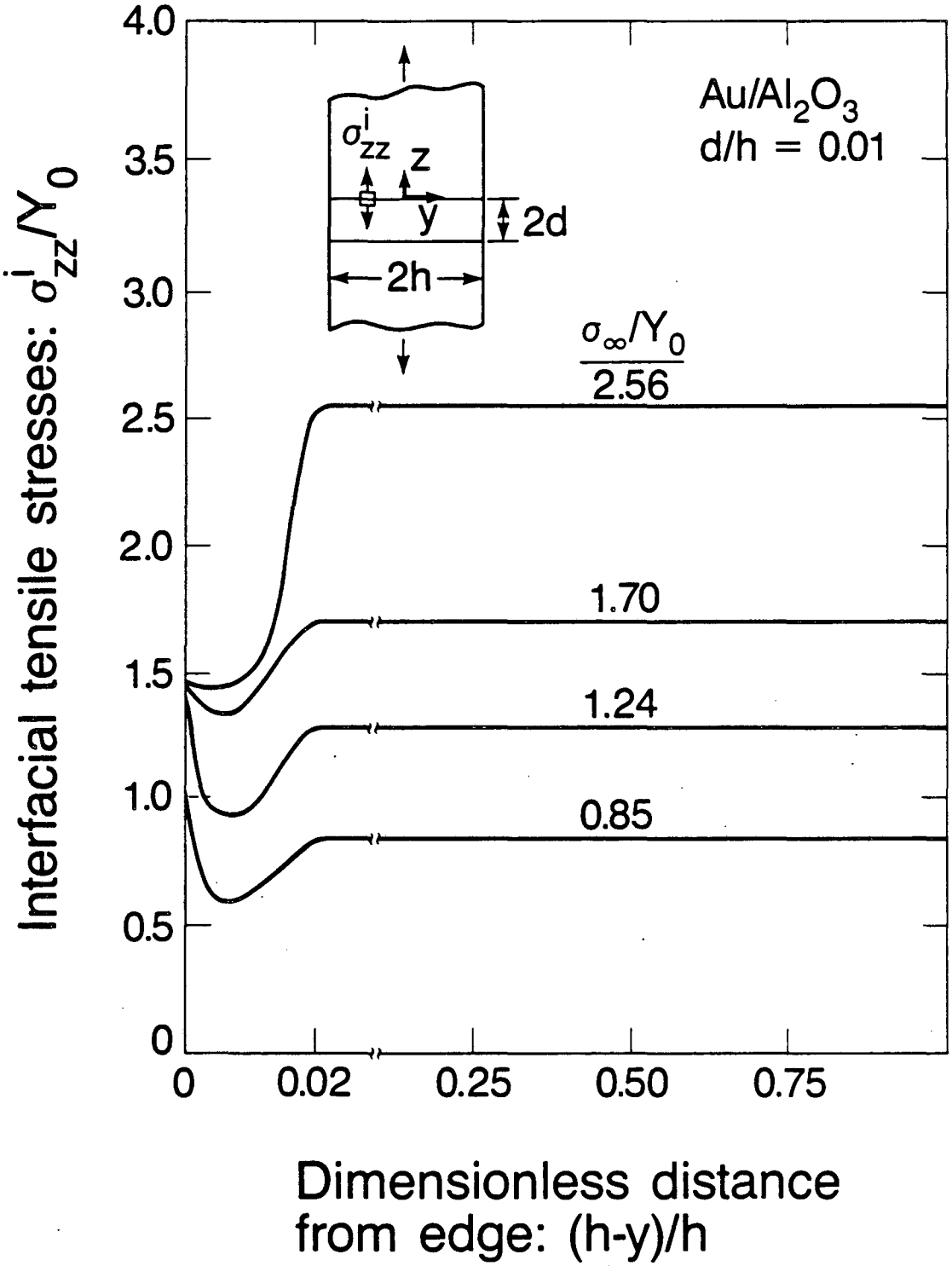

XBL 873-6221

Fig.4-8

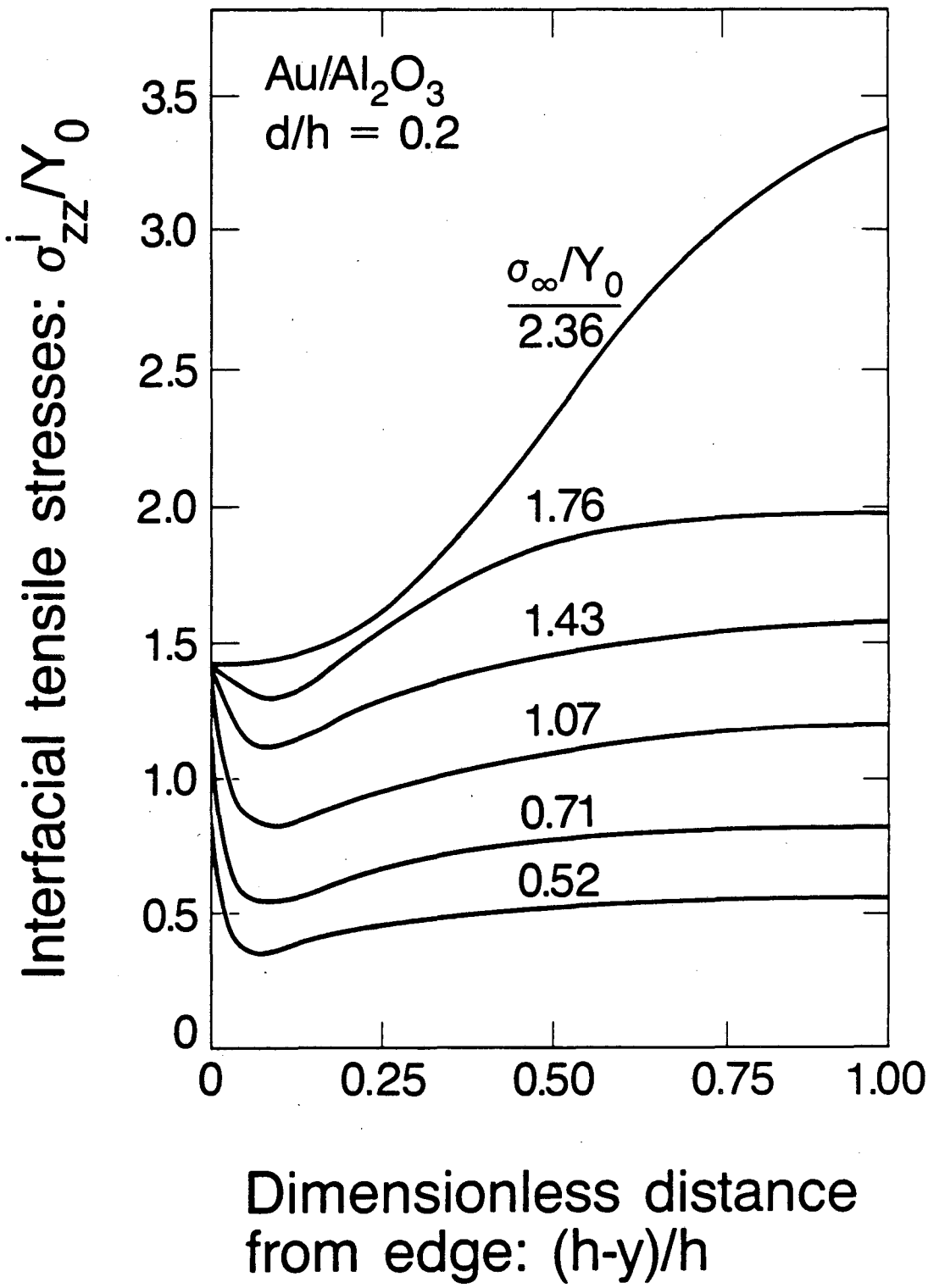

XBL 873-6216

Fig.4-9

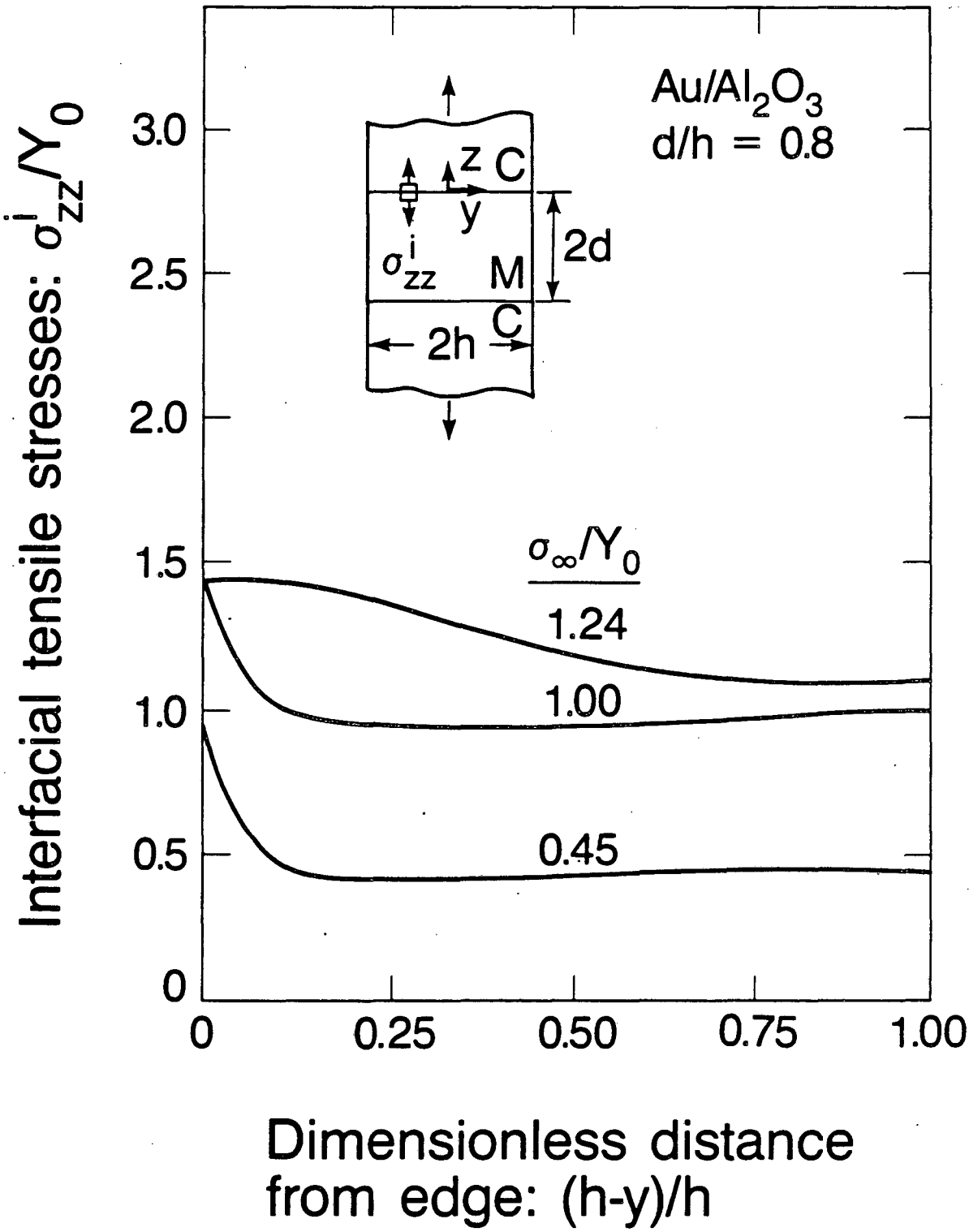

XBL 873-6220

Fig.4-10

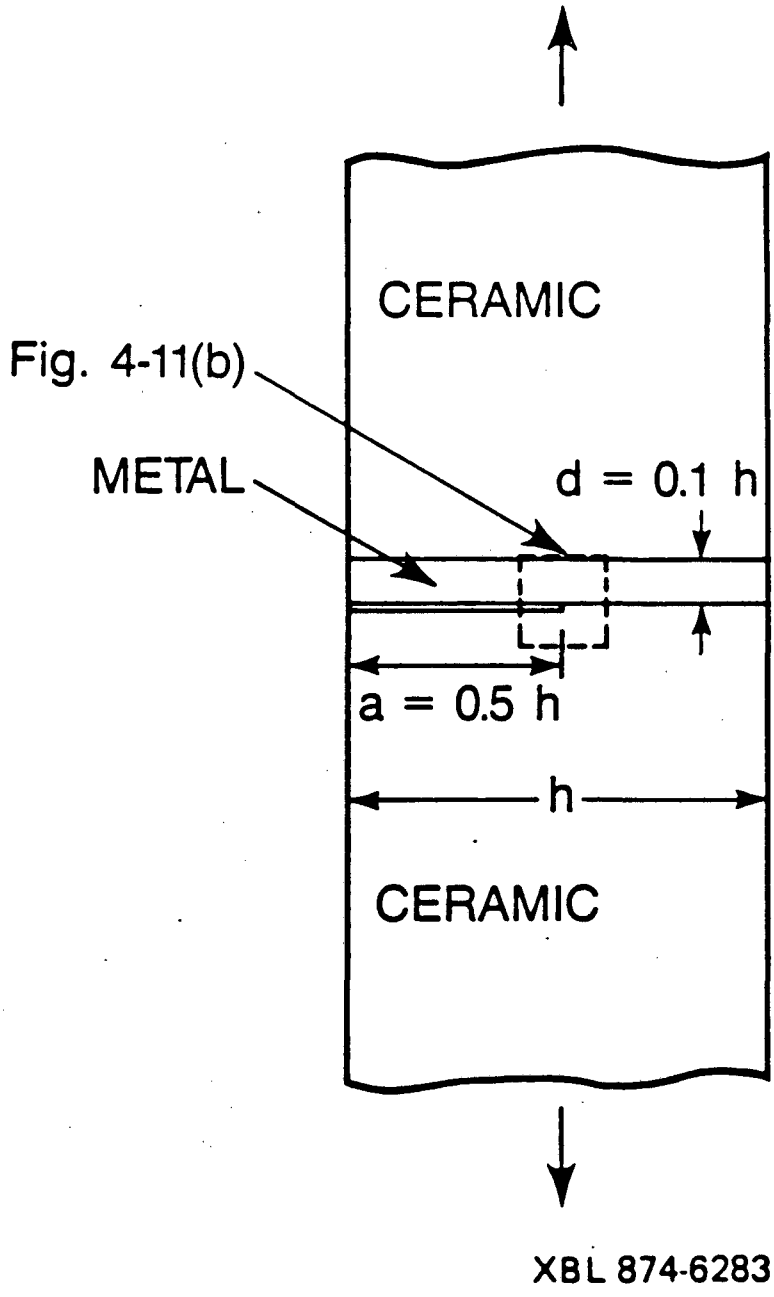

Fig.4-11(a)

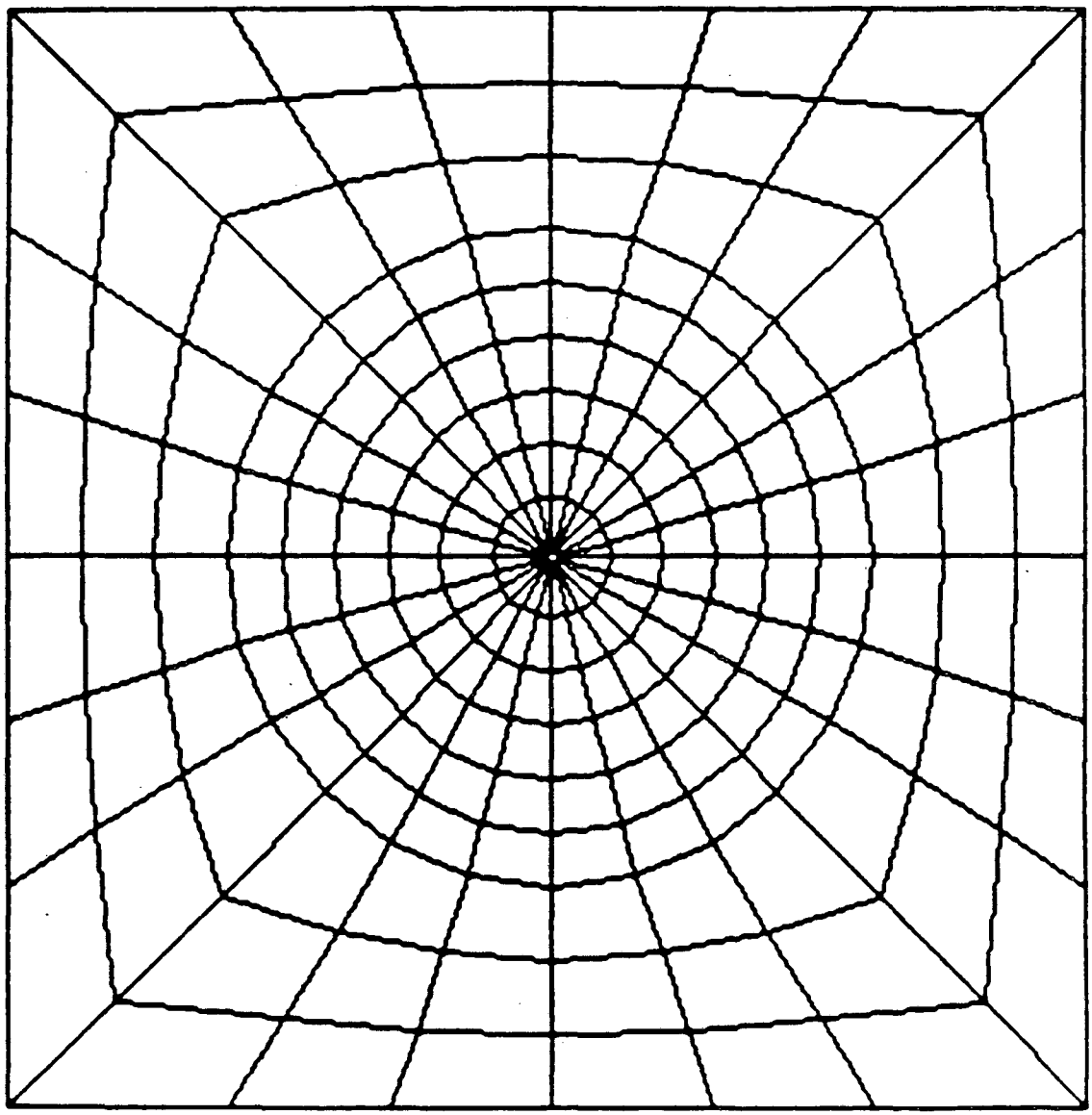

Fig.4-11(b)

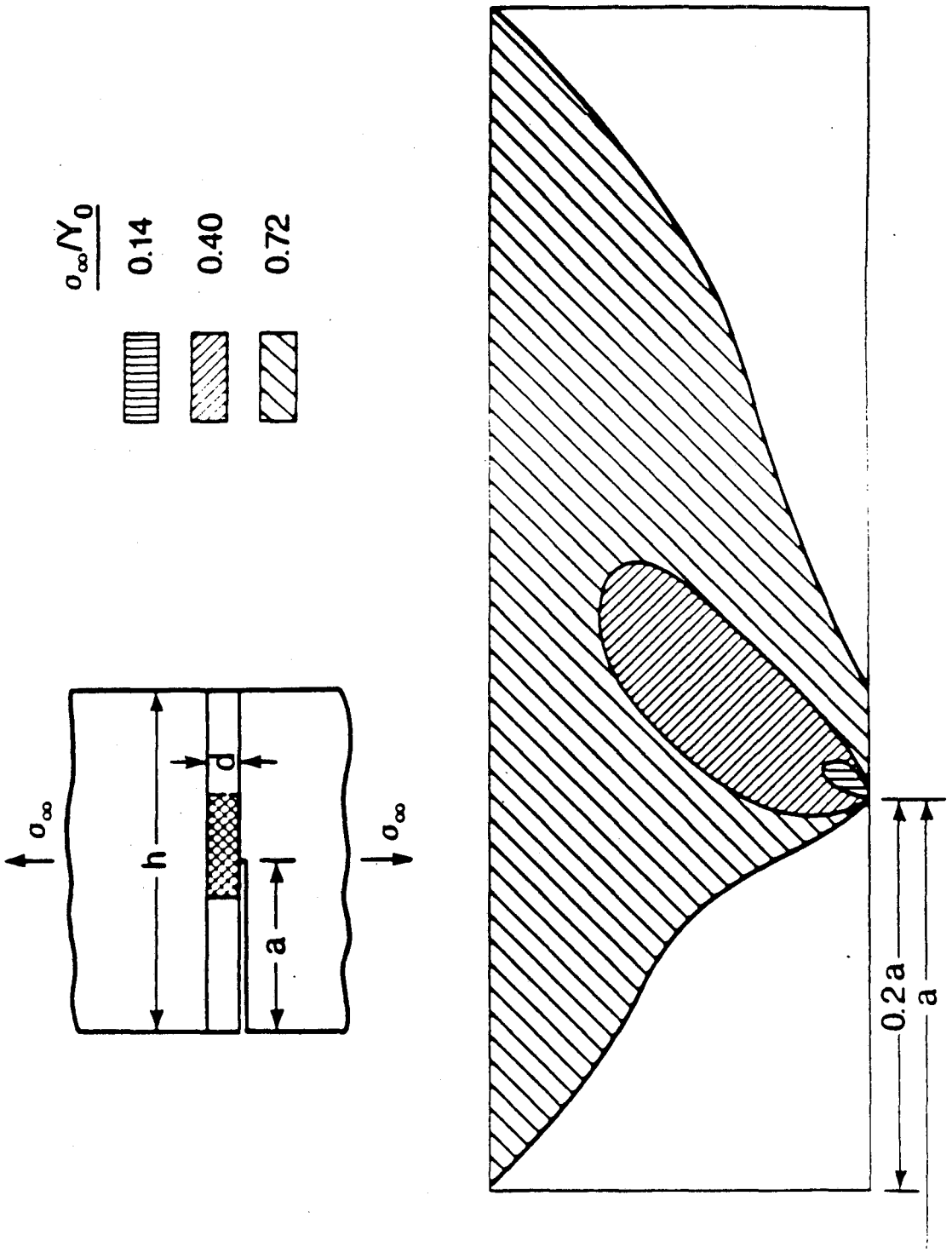

XBL 874-6267

Fig.4-11(c)

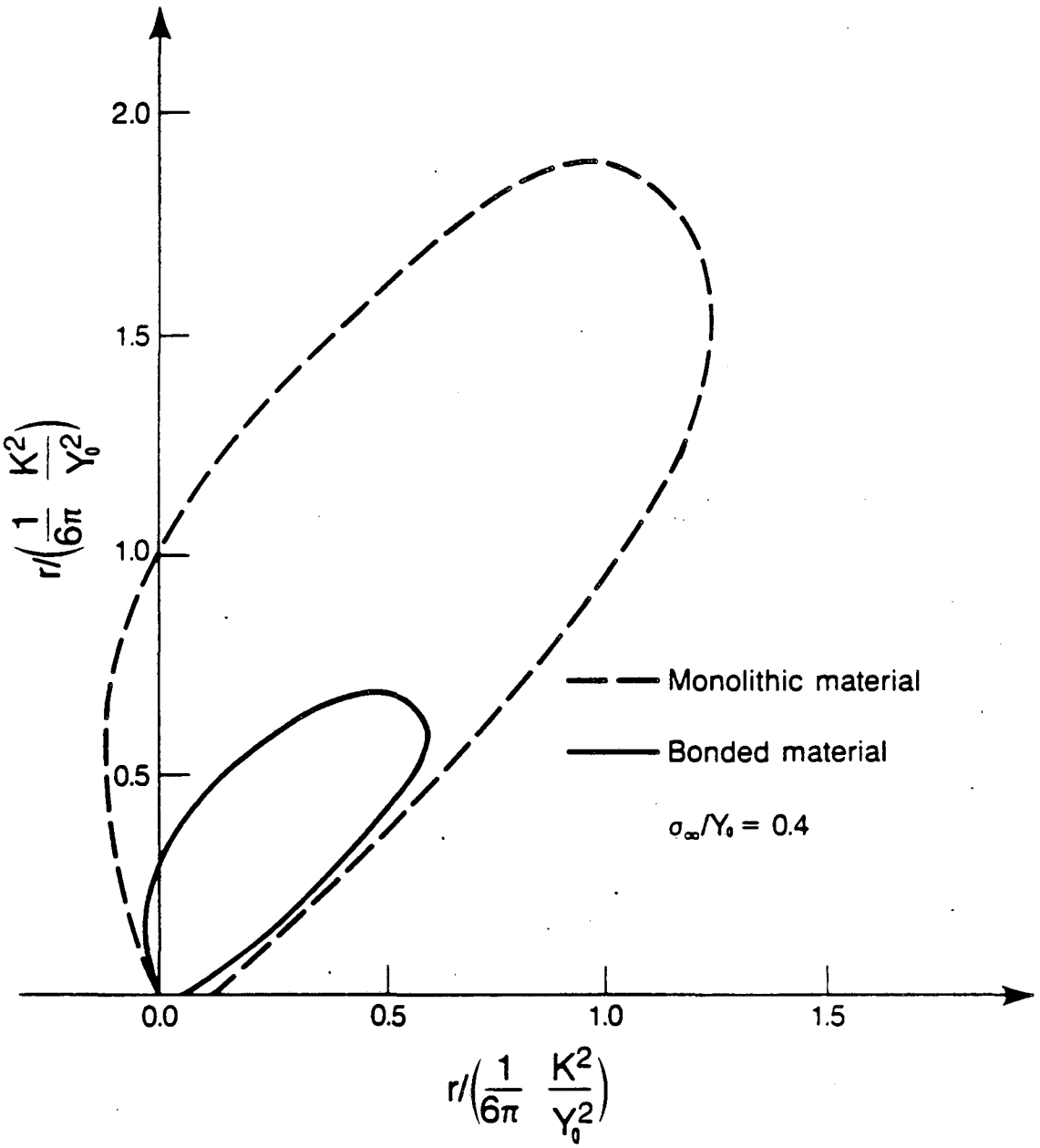

XBL 874-6280

Fig.4-12

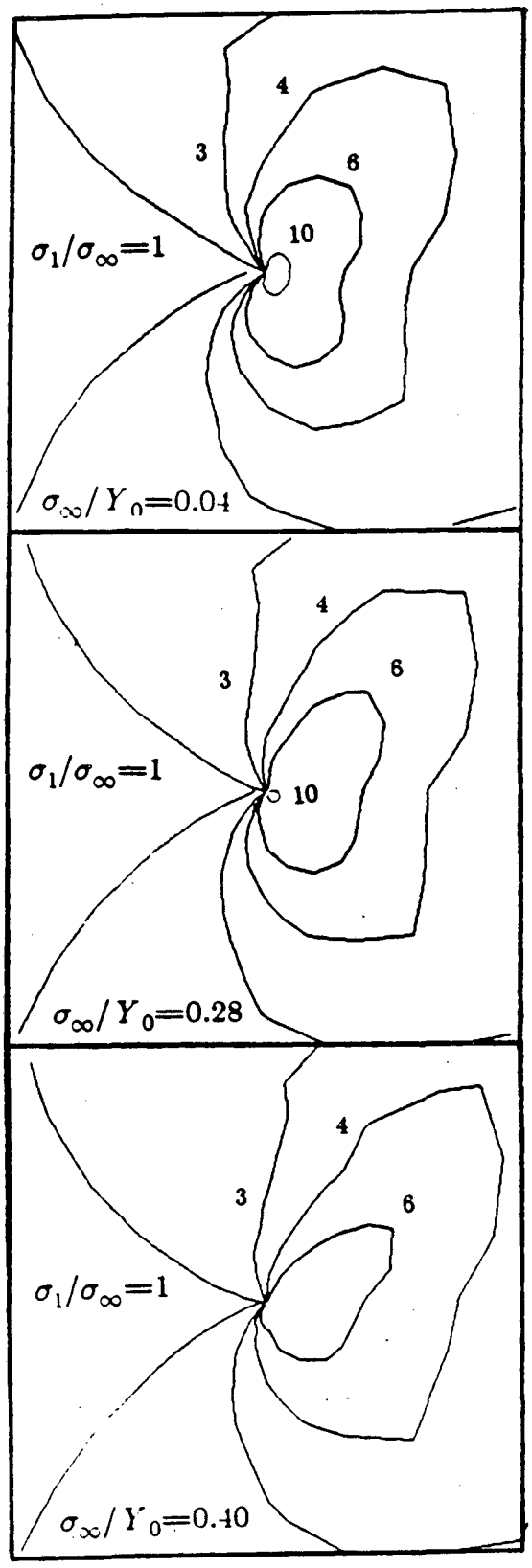
4
3
6
10
$\sigma_1/\sigma_\infty=1$
$\sigma_\infty/Y_0=0.04$
4
3
6
10
$\sigma_1/\sigma_\infty=1$
$\sigma_\infty/Y_0=0.28$
4
3
6
$\sigma_1/\sigma_\infty=1$
$\sigma_\infty/Y_0=0.40$

(a)

(b)

(c)

Fig.4-13

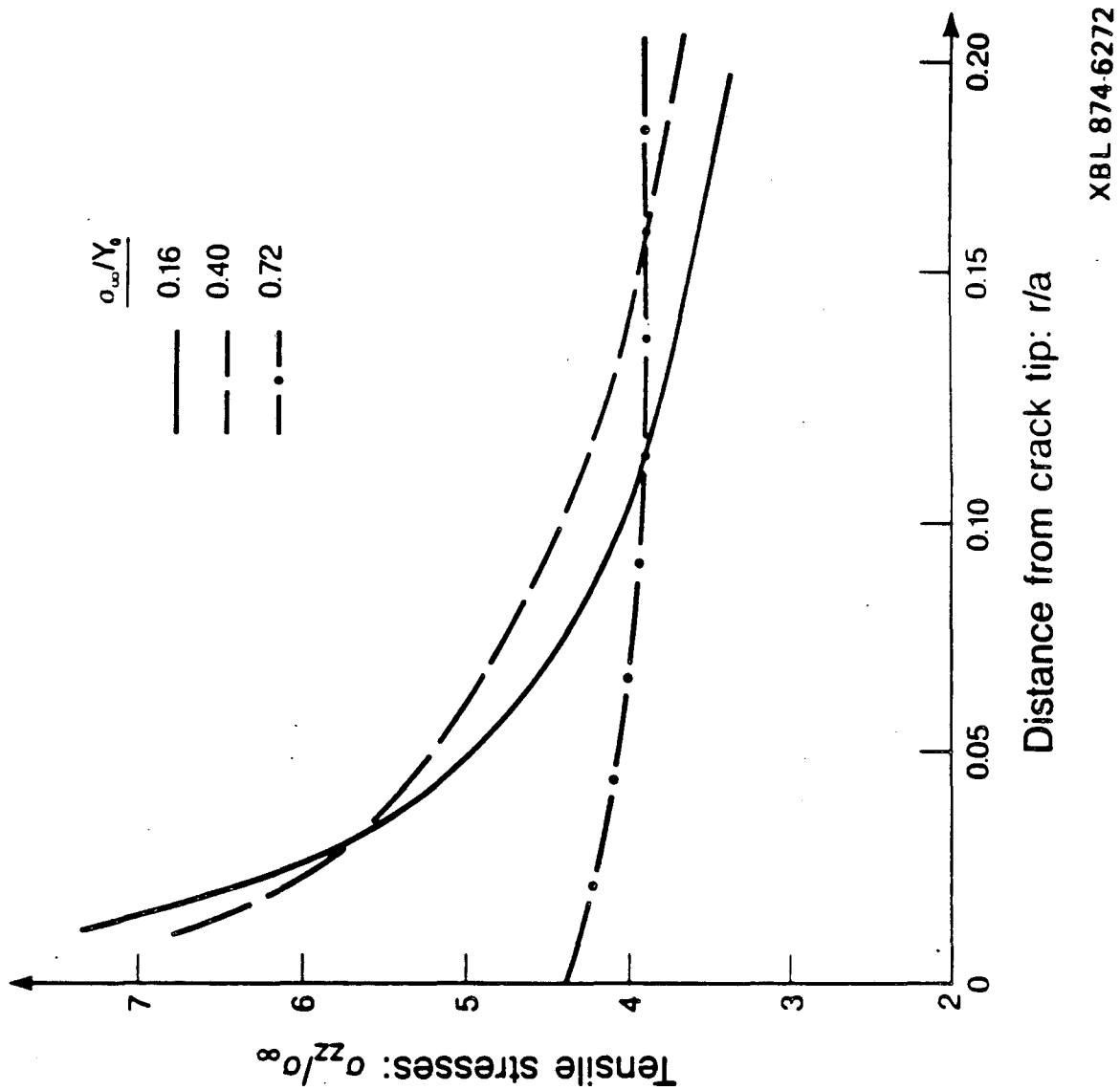
σ_∞/Y_0
0.16
0.40
0.72
Tensile stresses: $\sigma_{zz}/\sigma_\infty$
7
6
5
4
3
2
0
0.05
0.10
0.15
0.20
Distance from crack tip: r/a
XBL 874-6272

Fig.4-14

CHAPTER 5

INTERFACIAL STRENGTH: EXPERIMENTAL OBSERVATIONS AND FAILURE STATISTICS

The strength of a brittle material is dependent of the stress state, flaw size, and fracture toughness. The interfacial strength is evidently a function of the interfacial void distribution. The purpose of the present chapter is to study the interfacial microstructure and the corresponding interfacial strength.

1. Experimental Observations

1.1. Procedures

Commercially available polycrystalline alumina is prepared for bonding by sawing and grinding into blocks, 25.4 mm x 12.5 mm x 37.5 mm. The ground specimens are then polished on one end by optical finishing techniques using $15\mu m$,$9\mu m$,$6\mu m$, and $1\mu m$ diamond pastes sequentially. Gold foils (99.9% purity) having five thicknesses, ($25\mu m$,$51\mu m$,$127\mu m$,$254\mu m$, and $381\mu m$) are cut into sections having dimensions a little larger than 25.4 mm x 12.5 mm.

Prior to bonding, both the ceramic and gold are cleaned in acetone by ultrasonic agitation. The specimens are then rinsed in water and allowed to air dry. As a final pre-treatment both the ceramic and gold are pre-baked to $1000^o\ C$ for 1 hour in air. It is considered that such a treatment effectively removes hydrocarbons that may remain after the solvent cleaning procedure.

The bonding arrangement is shown in Fig.5-1. The specimen is assembled and placed between these two rams using a fixture that adjusts and aligns the load. This fixture consists of an alumina pressure plate with a hole in one side and a hemi-spherical alumina ball. The ball can rotate to align the load and provide uniform pressure to the specimen. Contact pressures between 2.7 to 5 MPa are applied using this arrangement.

The rate of heating is $0.5^o\ C/s$ followed by holding at the selected temperature ($1000^o\ C$ *or* $1045^o\ C$: the melting point of gold is $1064^o\ C$) in an air atmosphere for 10 to 15 hours. The load is only partially removed during cooling to inhibit thermal stress induced debonding. A complete pressure and temperature history during bonding is shown in Fig.5-2.

Three main sets of operating conditions are selected as shown in Table.5-1.

Table.5-1.

Bonding conditions

	(A)	(B)	(C)
Bonding temperature(C)	1000	1045	1045
Bonding time(hr)	10	10	15
Contact pressure(MPa)	2.7	3	3

In some cases 1 Kg indentations are placed in the gold before bonding in order to investigate the bonding mechanism. The bonding conditions used in such studies are $1045^o\ C$, 5 MPa, and 10 hours.

The blocks are cut and surface ground into beams, 3 mm x 3 mm in cross section and about 40 mm in length, with the gold layer at the center. Then two neighboring sides are polished by using $15\mu m$,$9\mu m$,$6\mu m$, and $1\mu m$

diamond pastes, sequentially. The mechanical properties are then measured in four point flexure (Fig.5-3) using a displacement rate of $10^{-2} mm/s$.

Most fractures initiated at the interface. However, the crack arrests without complete separation of the specimens. The profile of the arrested crack at the interface is observed using the scanning electron microscope. Then, the specimens are reloaded to separation and the fracture surfaces examined by scanning electron microscopy. The fracture surface topography is also investigated using a surface profilometer.

1.2. Measurements

The plastic flow strength of Au is estimated by indentation, and using, Y=H/3 [64]. Gold foils after heat treatment give Y=70 MPa, whereas after bonding Y=130 MPa. The different yield strengths suggest hardening due to the mismatch of thermal expansion coefficients during cooling. The value of 130 MPa is used for the calculation of the failure strength. The dihedral angles are also measured by a profilometer on fracture surfaces of the metal. The angle for is about 17° at 1000° C and 30° at 1045° C. The surface energy for Al_2O_3 is 1.81 J/m^2 at 1850° C and 1.99 J/m^2 at 1000° C. The reported values of surface energy for solid gold are 1.25 J/m^2 at 1000° C and 1.4 J/m^2 at 1120° C [47,48]. The interfacial energy of Au/Al_2O_3 is reported by Pillar [46] to be 1.75 J/m^2 at 1000° C. Therefore, the work of adhesion is 0.5 J/m^2. The value derived from the dihedral angles is about 0.3 J/m^2. This discrepancy could be caused by impurities (such as SiO_2) in the Al_2O_3.

Bonding at 1000° results in relatively large voids (Fig.5-4(a)), while at 1045° C only small voids exist (Fig.5-4(b)). Further analysis with Vickers indentations placed before bonding provides additional insights. The diagonal of the indent, originally 300 μ, reduced to a 45 μ circular region after bonding

at 1045° C for 10 hours subject to a pressure of a 5 MPa (Fig. 5-5).

The strengths exhibited by systems bonded in accordance with condition A and B have very different characteristics. For condition (A) the strengths (Fig.5-6) exhibit appreciable variability, and effects of thickness are not discerned. On the contrary, the strengths provided by condition (B) exhibit minimal variability and the mean strength tends to increase for bonds produced using thinner metal layer.

The stress state and fracture toughness for conditions (A) and (B) are essentially the same. However, the severity of flaws at the interface differs. Specimens from condition (B) exhibit crack paths that periodically deviate from the interface (Fig.5-7). Fracture in the ceramic (Fig.5-8), initiating at the interface (Fig.5-9), is also observed for condition (C). Examination of a small section of the fracture surface located along the interface, reveals a few, small voids. The strength, microstructure at the interface and the fracture behavior are listed in Table 5-2.

Table.5-2.

Relation between bonding conditions and the corresponding fracture behavior.

Bonding conditions	(A)	(B)	(C)
	1000° C	1045° C	1045° C
	2.7 MPa	3 MPa	3 MPa
	10 hrs	10 hrs	15 hrs
Failure Strength (MPa)	40-110	130-190	260-280
Mean void size μm	15	1.5	0.5
Failure origin	interface	interface	ceramic or interface (but soon deviating

into ceramic)

Examination of the profile of the bonded interface, reveals that the gold appears to perfectly duplicate the ceramic surface. Indeed, the gold even extends into pores within the ceramic (Fig.5-10). In specimens with metal layers having thickness of 25 μ, 51μ, and 127μ the failure path alternates between the two interfaces (Fig.5-11). This alternation is seemingly associated with the pull-out of metal ligaments from porosity in the ceramic. In the specimens with a thicker metal layer (254μ, 381μ) (Fig.5-12) the crack propagates simultaneously along both interfaces.

The failure of the specimens is macroscopically brittle, as evident from the load-deflection curves. However, the cracks arrested during propagation, with a blunt crack observed upon arresting (Fig.5-13(a)). Initial reloading caused further blunting (Fig.5-13(b)). However, at larger loads, a metal ligament is apparent at the arrest site, that pulled-out from the pores within the ceramic. This observation suggests that the crack is, in fact, locally arrested by a metal ligament (Fig.5-13(c)). Occasionally, however, interfacial crack blunting is observed (Fig.5-14), when fracture occurred in the ceramic, but the interface also debonded.

2. Failure Statistics

2.1. Theoretical Background

Brittle fracture governed by a distribution of interfacial flaws is a statistical problem [65-68], wherein the fracture probability can be related to the flaw size distribution. However, the development of appropriate relationships is contingent upon an interfacial fracture criterion. Presently, a universal criterion does not exist. For present purposes, it is simply assumed that a critical strain

energy release rate $\overline{\mathbf{G}_c}$ determines the onset of fracture. Then, for fracture dominated by the local normal stress σ_{zz} , as appropriate for the present problem ($\sigma_{zz} >> \sigma_{zy}$ Fig.3-5) the normal stress, at fracture, **S** , is related to the flaw radius, **a** , by;

$$\mathbf{S}^2 = (4\cosh^2\pi\epsilon)\,\overline{\mathbf{G}_c}\,(1+4\epsilon^2)\,[(1-\nu_1)/G_1 + (1-\nu_2)/G_2]^{-1} / \pi\,\mathbf{a} \qquad (5\text{-}1)$$

where G is the shear modulus and ν the Poisson's ratio, and the subscripts 1 and 2 refer to the two materials. At the very simplest level,

$$\overline{\mathbf{G}_c} = \lambda\, W_{ad} \qquad (5\text{-}2)$$

where W_{ad} is the work of adhesion and λ is a coefficient governed by crack tip plasticity in the metal, microstructure interactions etc. The flaw size distribution, **g(a)da** , can converted into flaw strength distribution, **g(S)dS**, using equation 5-1 and 5-2, with λ as an unknown variable.

It is further assumed that weakest link statistics obtain, whereupon the survival probability is

$$1-\mathbf{P} = \exp[-\int_A dA \int_0^{\sigma_{zz}(y)} \mathbf{g(S)dS}\,] \qquad (5\text{-}3)$$

where A is the total interface area and **g(S)dS** is the number of flaws in unit area having strength between **S** and **S+dS**. Present measurements of flaw size distributions (Fig.5-15) suggest the simple statistical form

$$\int_0^{\mathbf{S}} \mathbf{g(S)dS} = (\mathbf{S}/S_0)^m\, A_0^{-1} \qquad (5\text{-}4)$$

where m is a shape parameter and S_0 and A_0 are scale parameters. Therefore, from equations (5-3) and (5-4)

$$1-\mathbf{P} = \exp[-(4bh/A_0)\int_0^1 [\sigma_{zz}^i(t)/S_0]^m\, dt\,] \qquad (5\text{-}5)$$

where t=y/h and b is the specimen width.

2.2. Flaw Strength Distribution

Flaw size distributions have been obtained by examining the fracture surfaces (Fig.5-4) and evaluating the equivalent flaw radius, **a** from the cross sectional area, A; $\mathbf{a}=\sqrt{A/\pi}$. The flaw density parameter, **g(a)da** , is obtained from histograms (Fig.5-16), as the number of flaws in unit area having radii between **a** and **a+da** . The size distributions are then converted into strength distribution, **g(S)dS**, using equations (5-1) and (5-2) for choices of $\lambda = 1,2,5$ ($W_{ad} = 0.5\ J/m^{-2}$) as depicted in Fig.5-5. The results are fitted to equation (5-4) giving the values of m and S_0 indicated in Table.5-3.

Table.5-3.

Parameters of flaw strength distribution.

Bonding conditions		(A)	(B)	(C)
m		3	6	9
S_0 (MPa)	$\lambda=1$	69	160	281
S_0 (MPa)	$\lambda=2$	101	226	397
S_0 (MPa)	$\lambda=5$	197	358	628

2.3. Failure Statistics

The experimental results reveal failures around the transition from region I to region II (Fig.4-4), such that slight non-linearity precedes the ultimate load. The stress distributions $\sigma_{zz}^{i}(y)$ within this region (Fig.4-6) can thus used in conjunction with equation(5-5) to calculate failure probabilities, based on the values of m and S_0 obtained in the previous section. The results can be conveniently expressed in the non-dimensional form;

$$-ln\,(1-\mathbf{P})=(\frac{4bh}{A_0})(\frac{\sigma_\infty}{S_0})^m\ f\ (m\ ,d\ /h\ ,\sigma_\infty/Y_0) \qquad (5\text{-}6)$$

where f is the function plotted in Fig.5-18.

A comparison between measured and predicted median strengths (Fig.5-18), based on equation (5-6) and using values of m and S_0 from Table.5-3 reveal good correspondence for $\lambda=1$, indication of negligable crack tip plasticity.

Figure Captions

Fig.5-1.

An illustration of the experimental set-up and the alignment of specimen.

Fig.5-2.

The variation of the bonding conditions, temperature and pressure , along time.

Fig.5-3.

The relative position of the specimen to the four-point bend fixture.

Fig.5-4.

The representive void distributions induced by bondition conditions (A), (B), and (C) are shown in (a), (b), and (c) respectively.

Fig.5-5.

The effect of diffusion by Au is shown by the remaining small void in (b) through the mass transfer of material during bonding to the initial indent in (a).

Fig.5-6.

Failure strengths measured by four-point bending test varied with the thickness of metal interlayer and the different bonding conditions.

Fig.5-7.

A sideview of the fracture surface shows that the crack initiated at the interface can deviate into the ceramic.

Fig.5-8.

Failure of specimen bonded under the condition (C) occurs in the ceramic.

Fig.5-9.

A fracture surface of specimen bonded under the condition (C) showing the failure initiated at the interface soon deviates into the ceramic.

Fig.5-10.

A strong effect of diffusion makes a perfect match at the interface. The metal can even intrude into the very end of the pore.

Fig.5-11.

Fracture paths exchange from one side to the other side of the metal in specimen bonded under the condition (A) with thin metal layer.

Fig.5-12.

Fracture paths in both sides of the metal occur in the specimen bonded under the condition (A).

Fig.5-13.

A crack front stopped by an intruded metal stub is observed. (a) a blunted interface crack, (b) the crack opening increased by reloading, (c) a pulled-out metal stub is observed by further reloading.

Fig.5-14.

An interface crack is blunted by substantial plastic deformation of the metal.

Fig.5-15.

The relation of void distribution to the strength distribution by using equation (5-1) as well as the determination of the Weibull shows the appropriate choice of the form of the Weibull distribution.

Fig.5-16.

Histograms of void distribution for specimens bonded under (a) condition (A), (b) conditon (B), (c) condition (C).

Fig.5-17.

The value of function f(m, d/h, σ_∞ / Y_0) varying along the σ_∞ / Y_0.

Fig.5-18.

The comparison of failure strengths between values measured by experiments and predicted by statistical analysis.

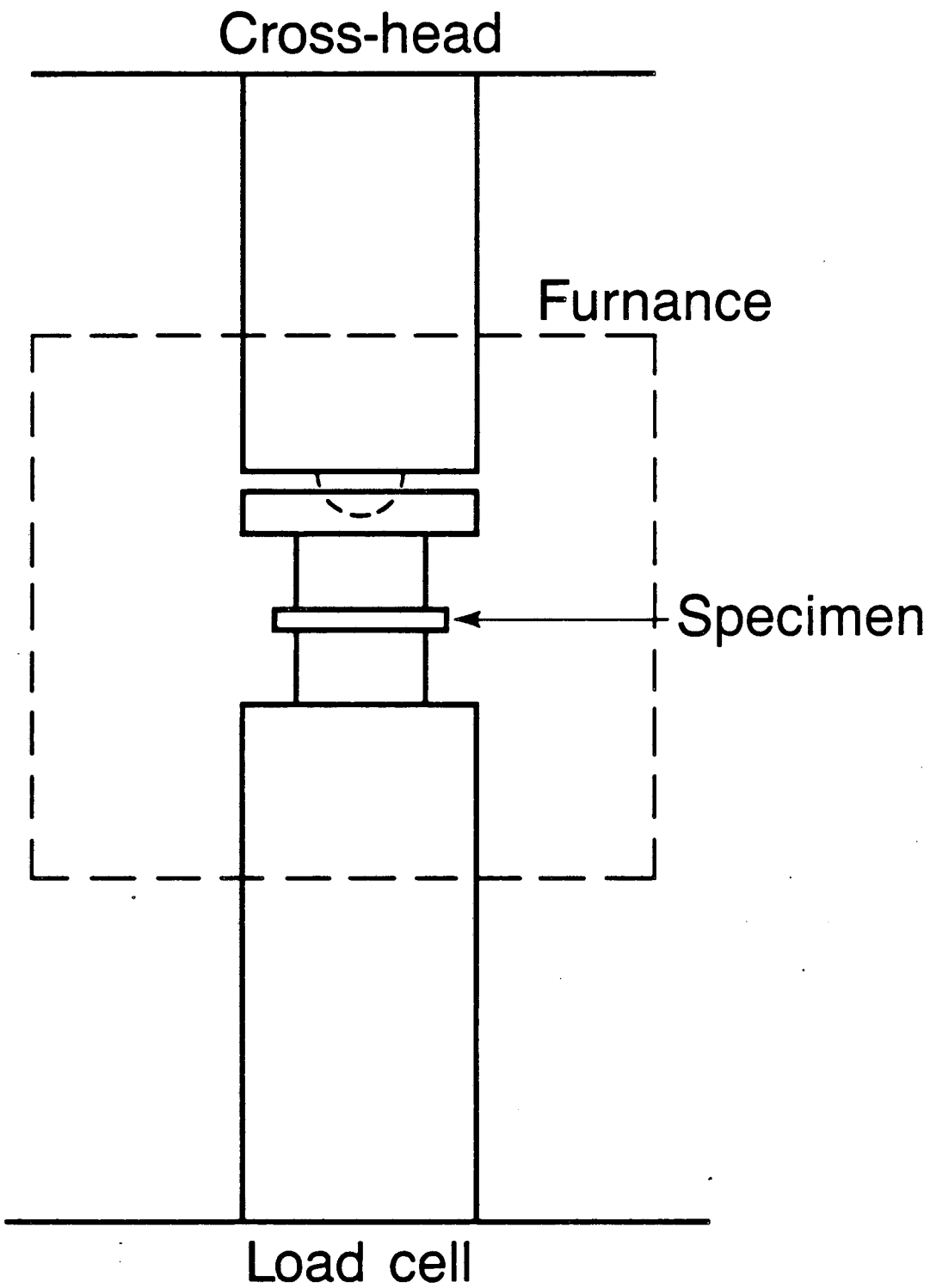

XBL 873-6226

Fig.5-1

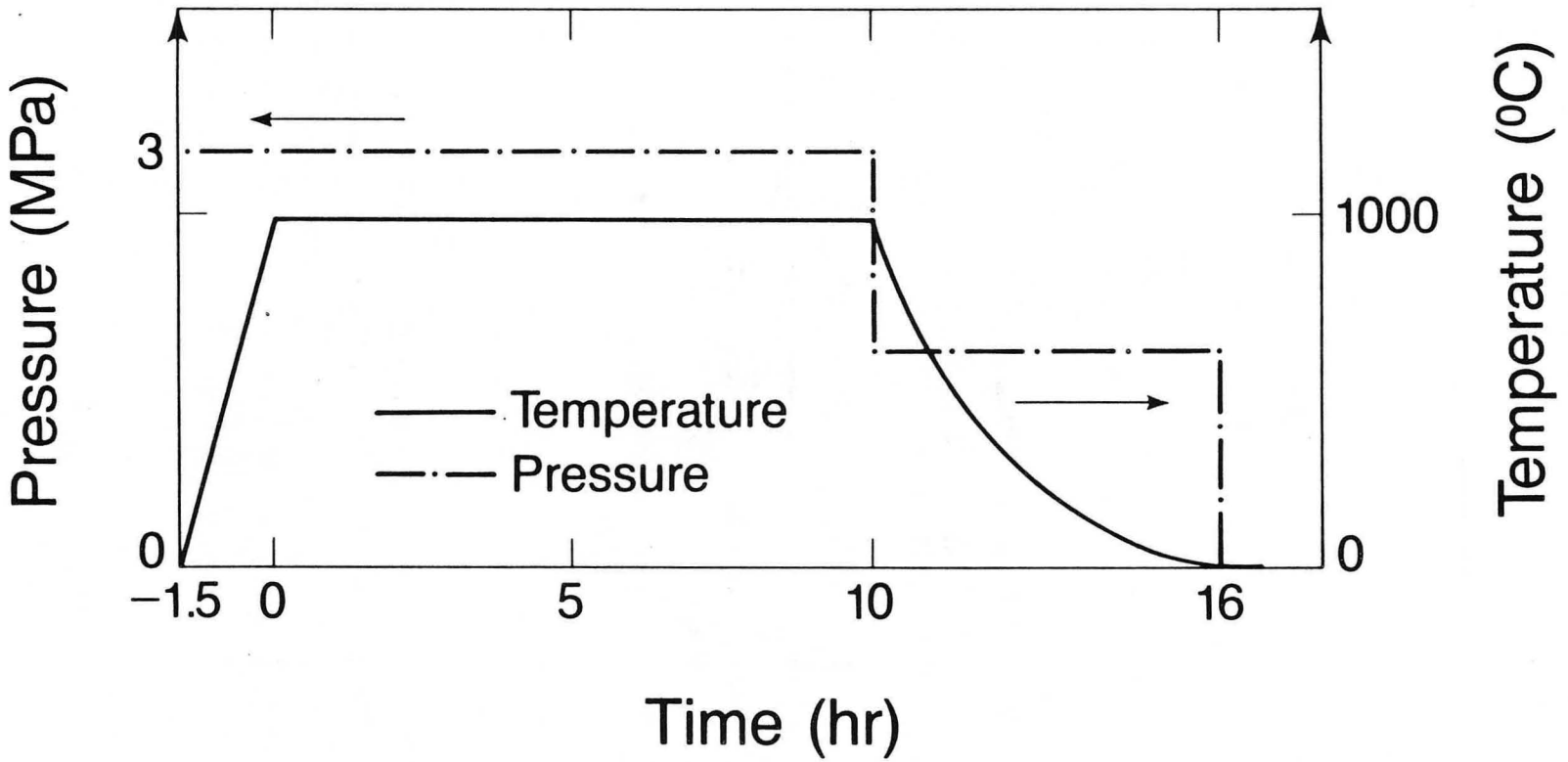

XBL 873-6214

Fig.5-2

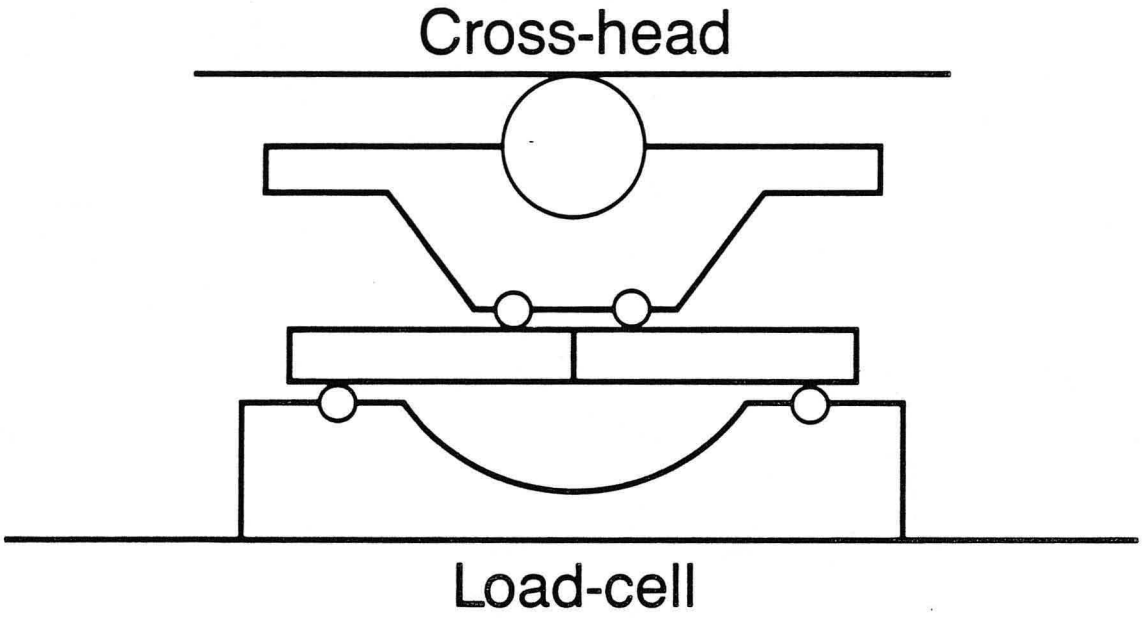

XBL 873-6225

Fig.5-3

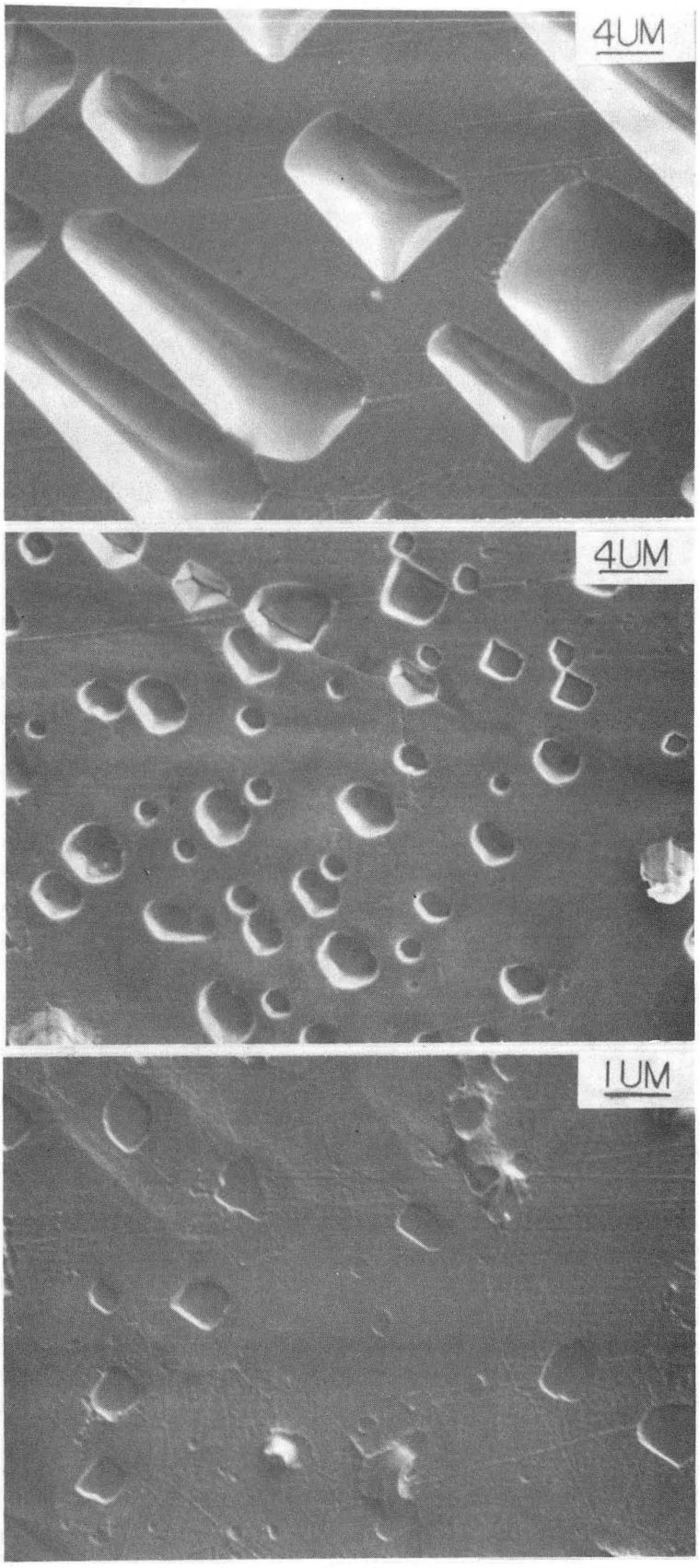

(A)
1000°C
2.75MPA
10HRS

(B)
1045°C
3.0MPA
10HRS

(C)
1045°C
3.0MPA
15HRS

XBB 874-2788

Fig.5-4

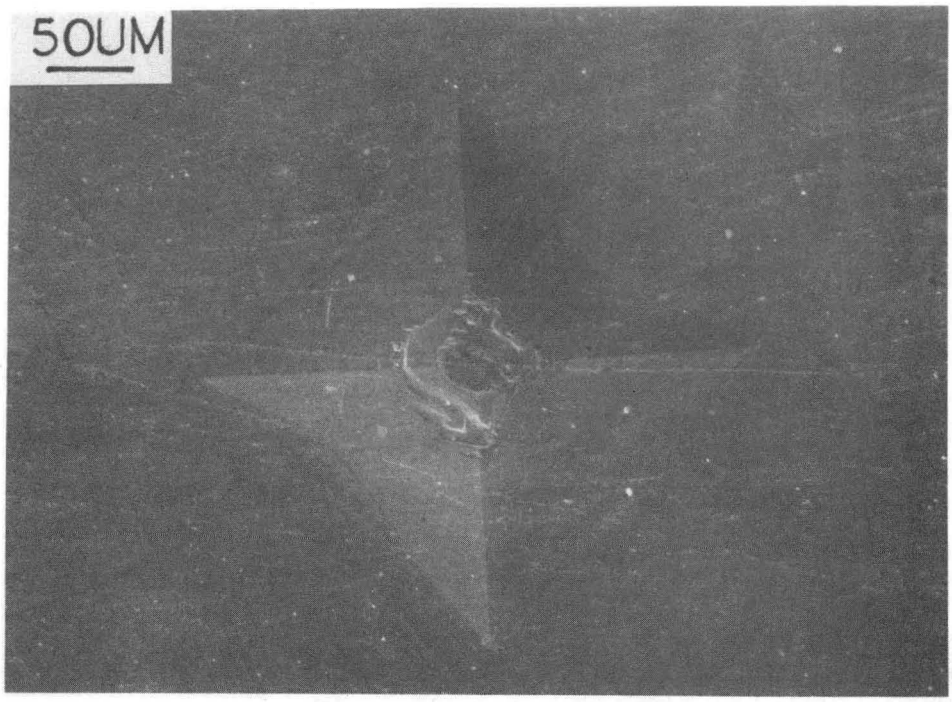

(A)

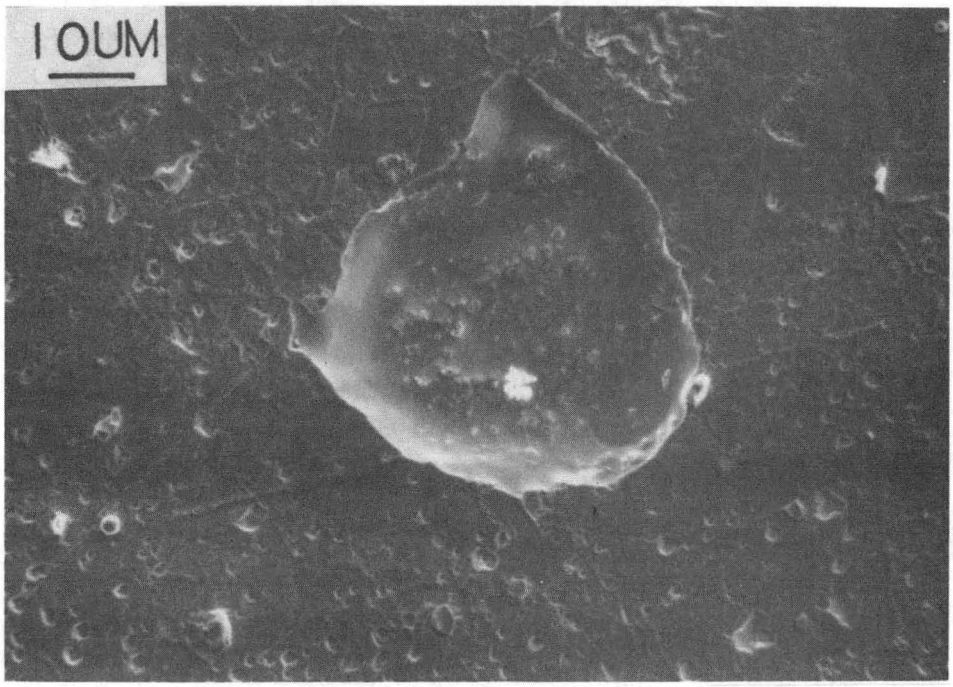

XBB 874-2786

(B)

Fig.5-5

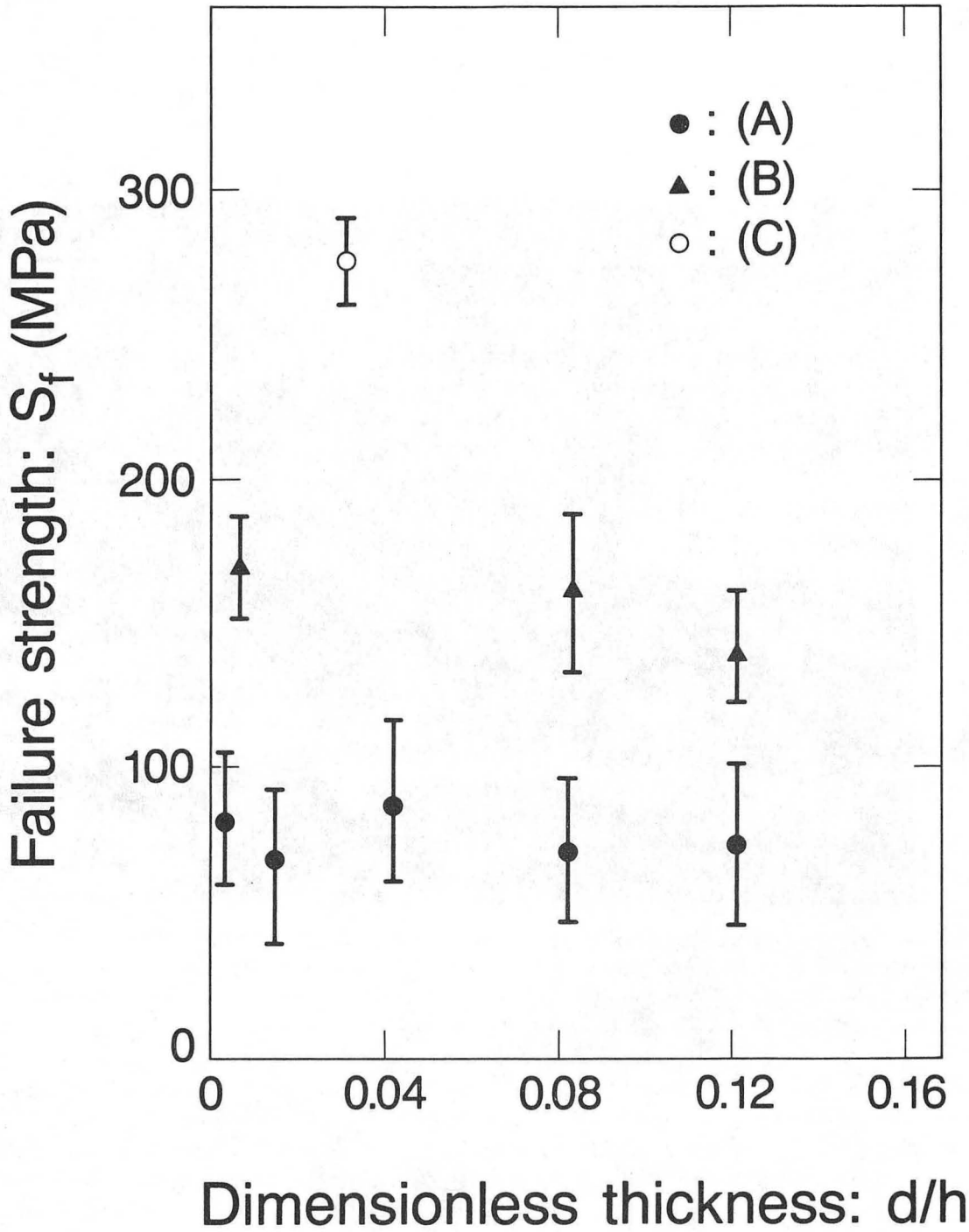

XBL 873-6219

Fig.5-6

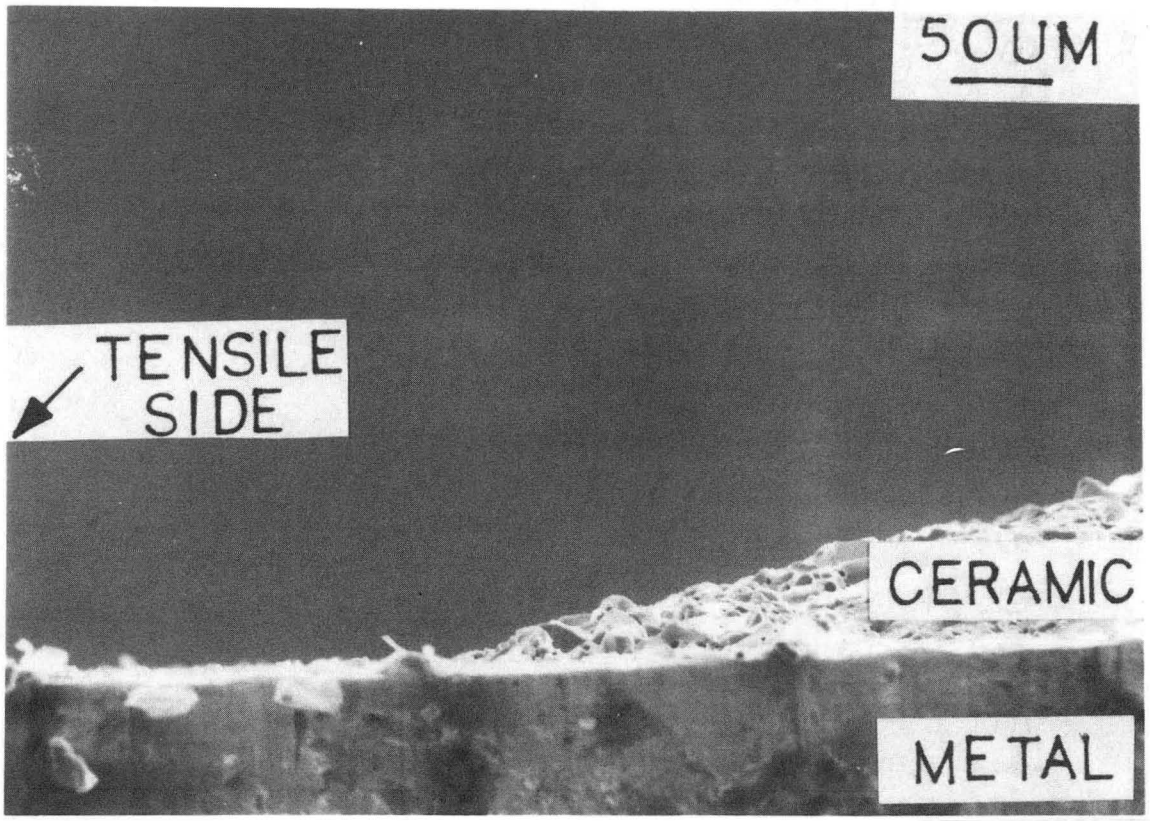

XBB 874-2775

Fig.5-7

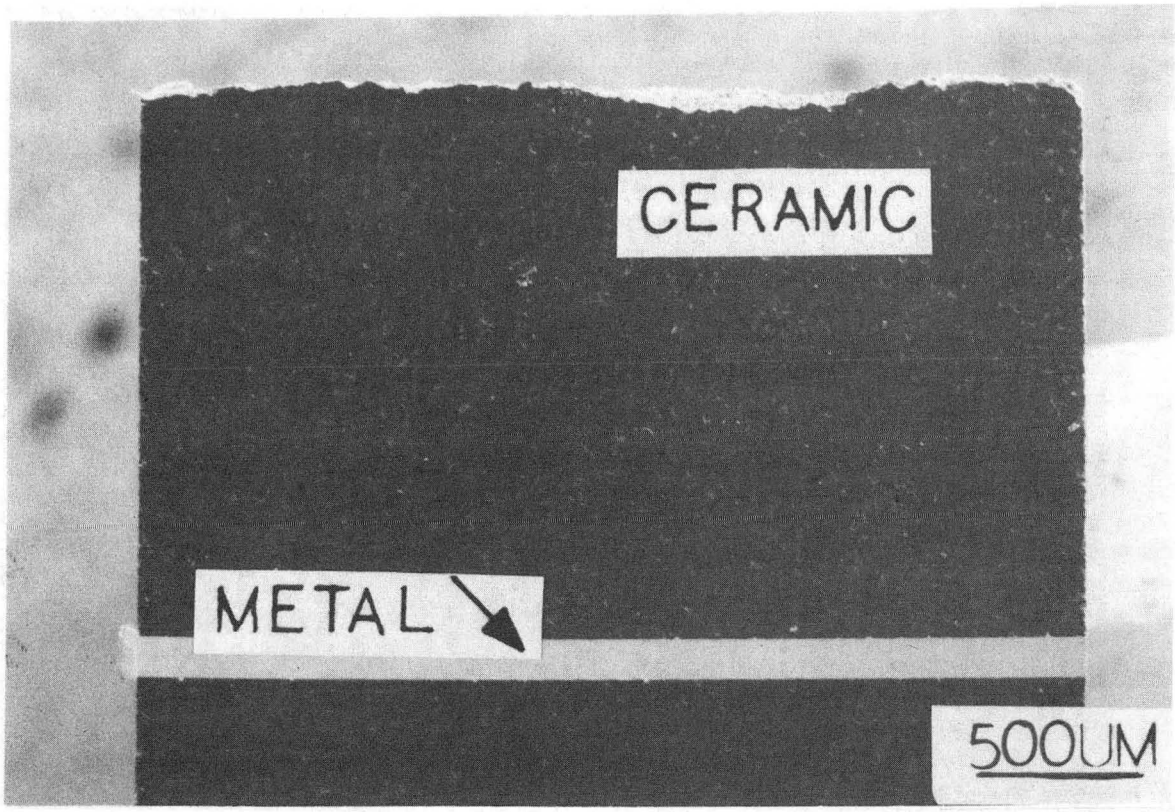

XBB 874-2785

Fig.5-8

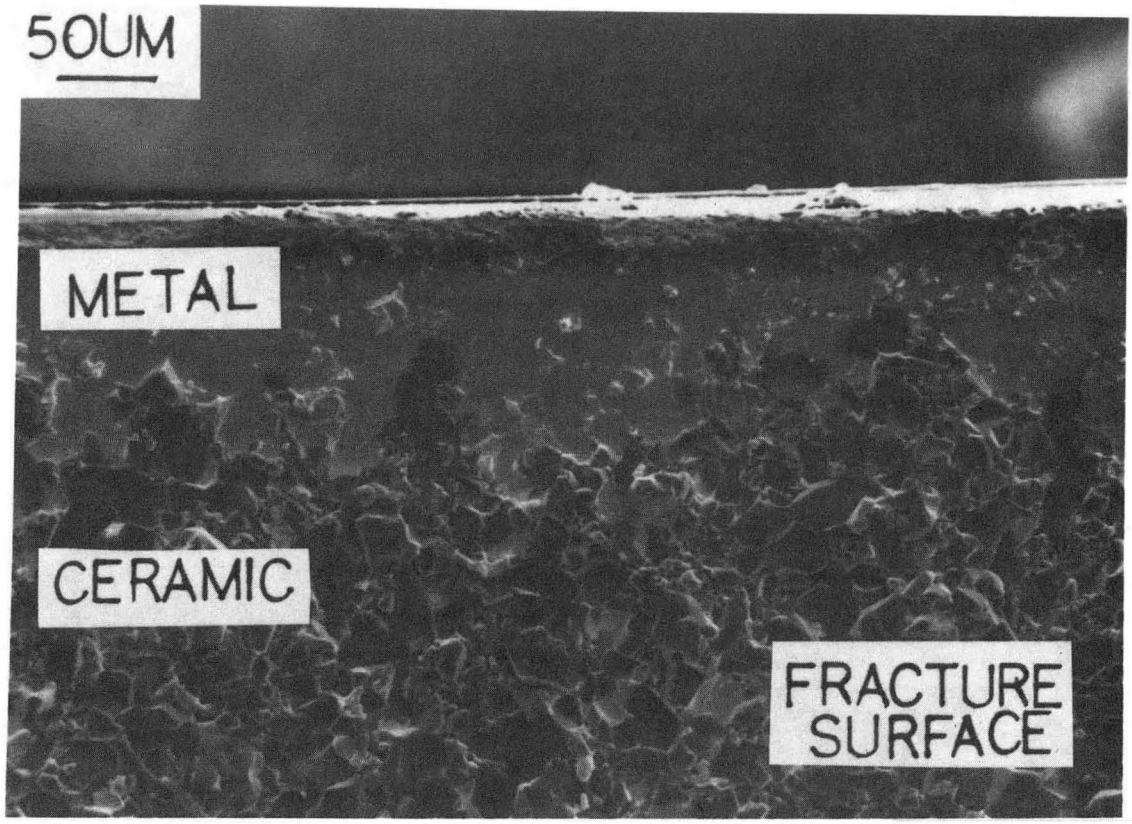

XBB 874-2784

Fig.5-9

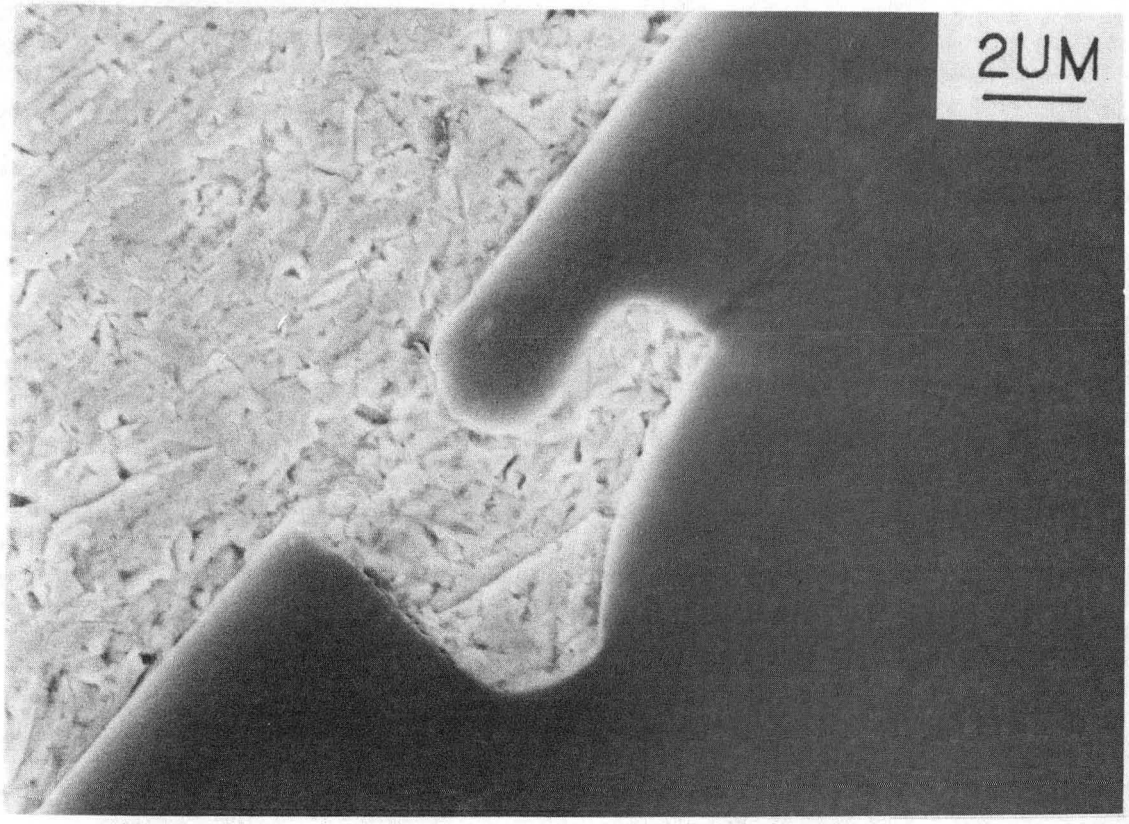

XBB 874-2777

Fig.5-10

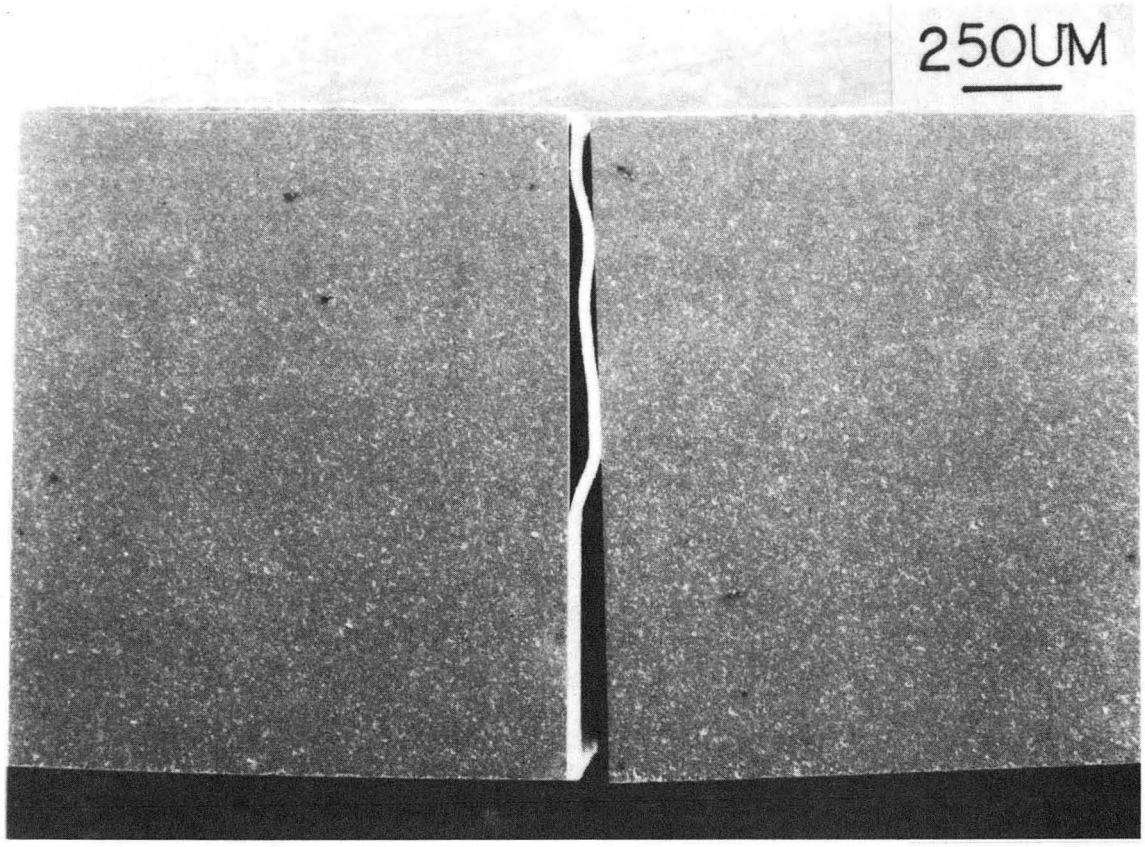

XBB 874-2776

Fig.5-11

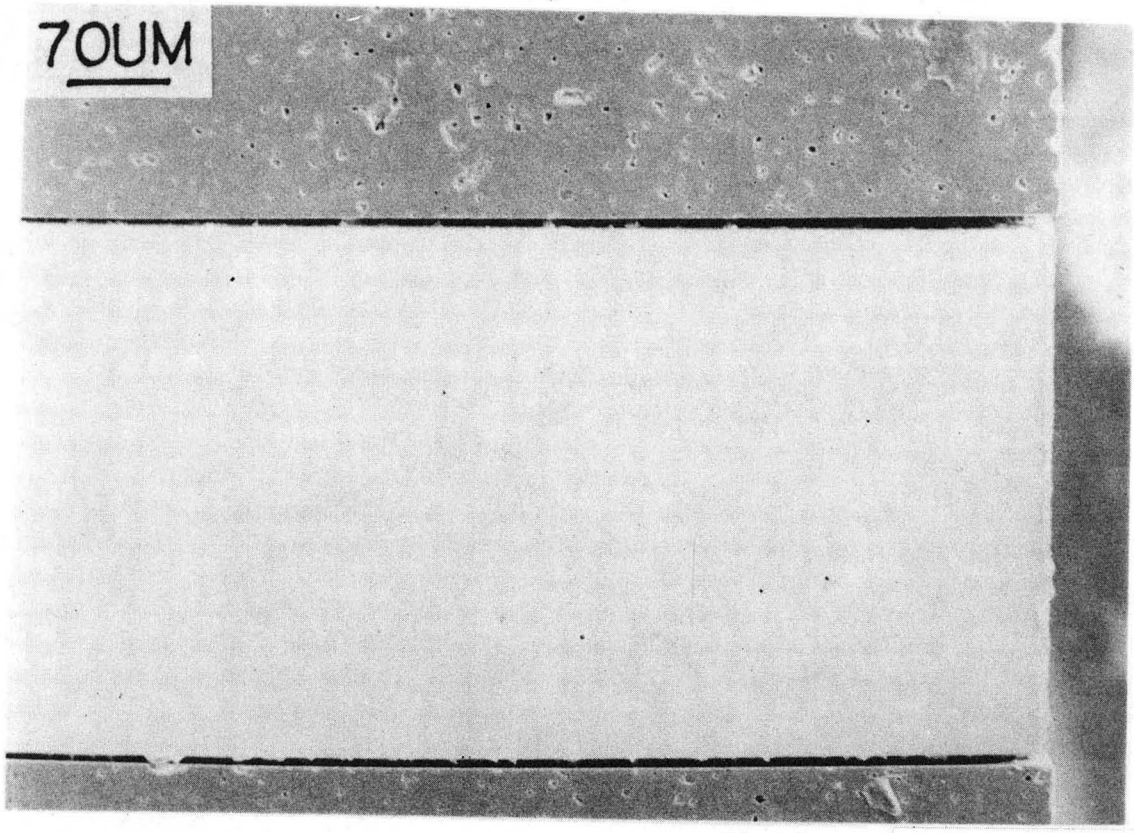

XBB 874-2779

Fig.5-12

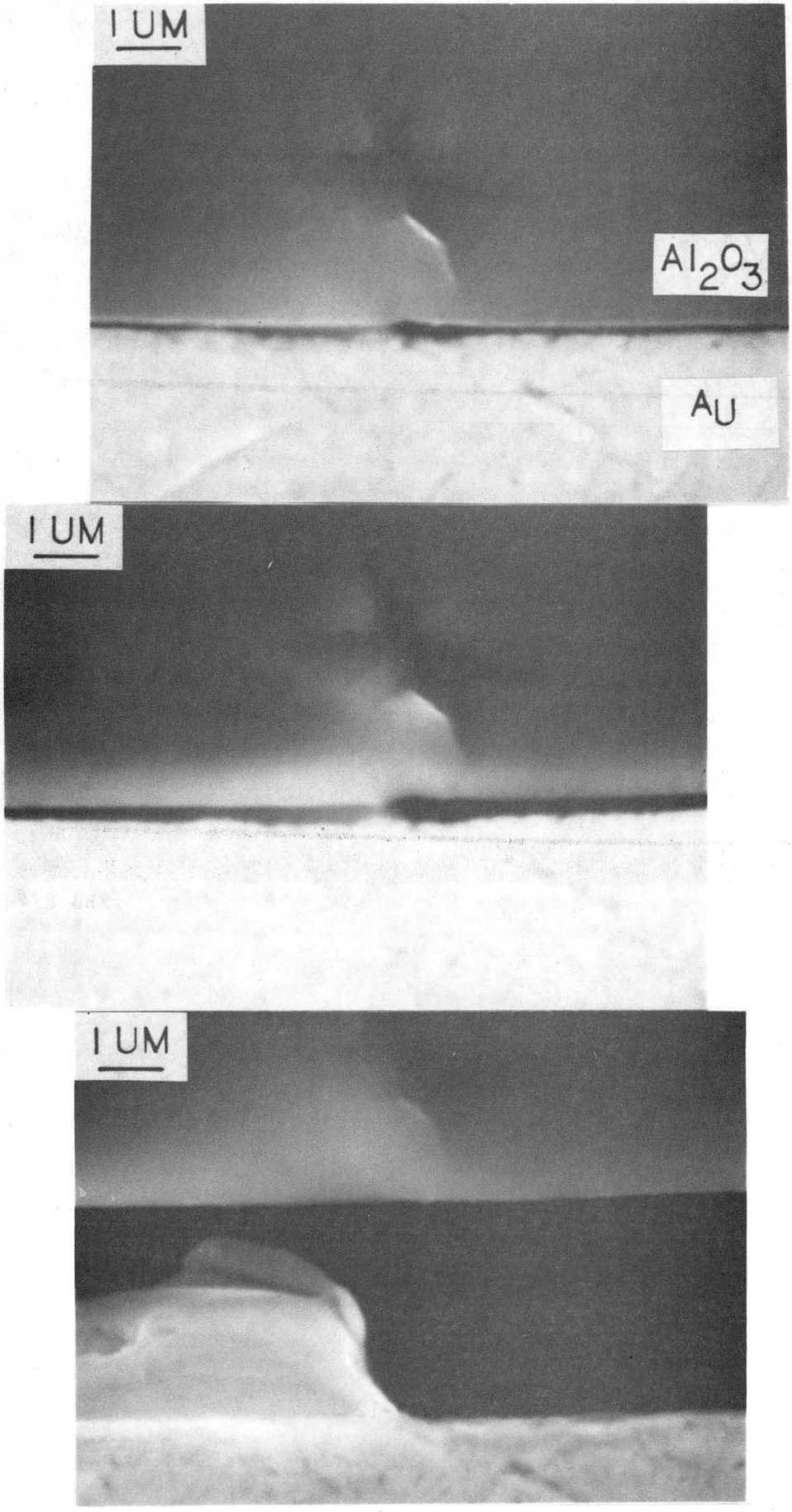

XBB 874-2787

Fig.5-13

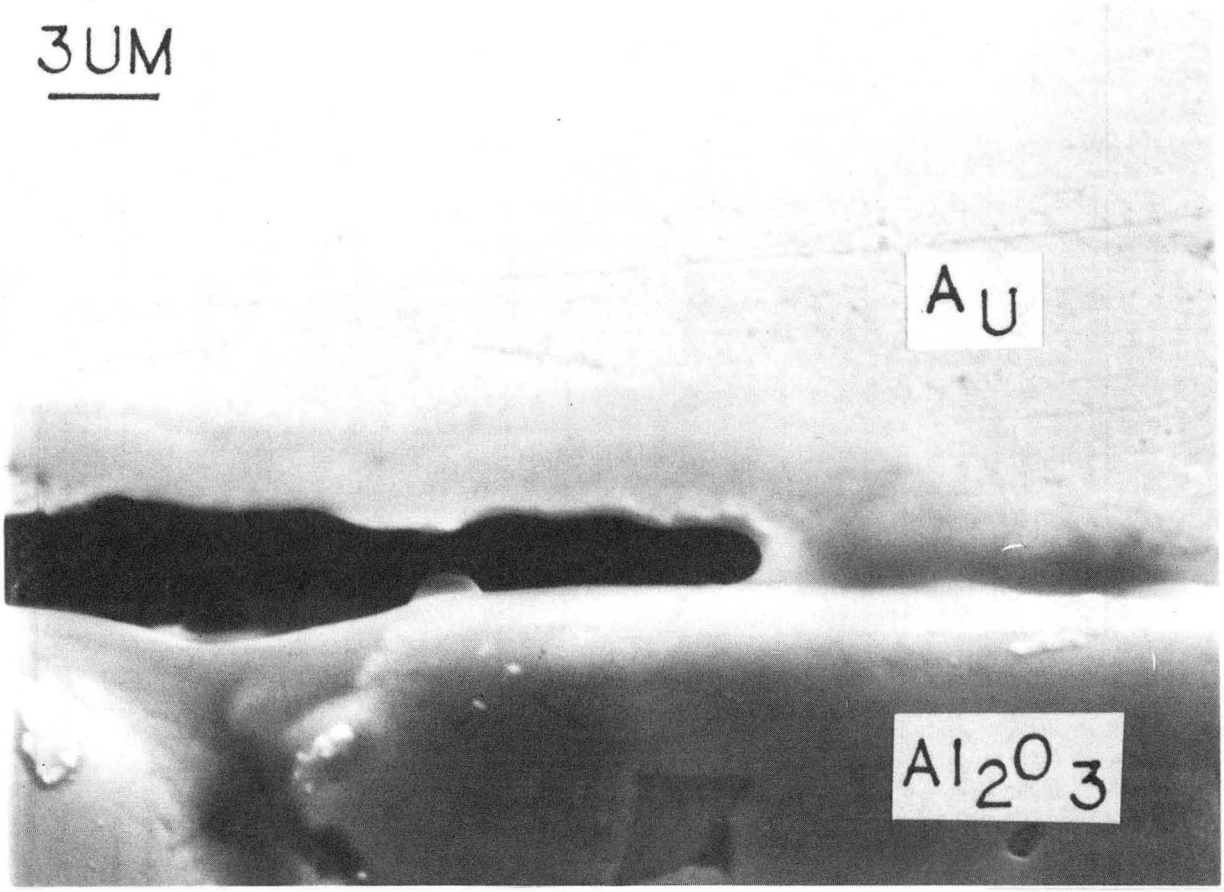

XBB 874-2783

Fig.5-14

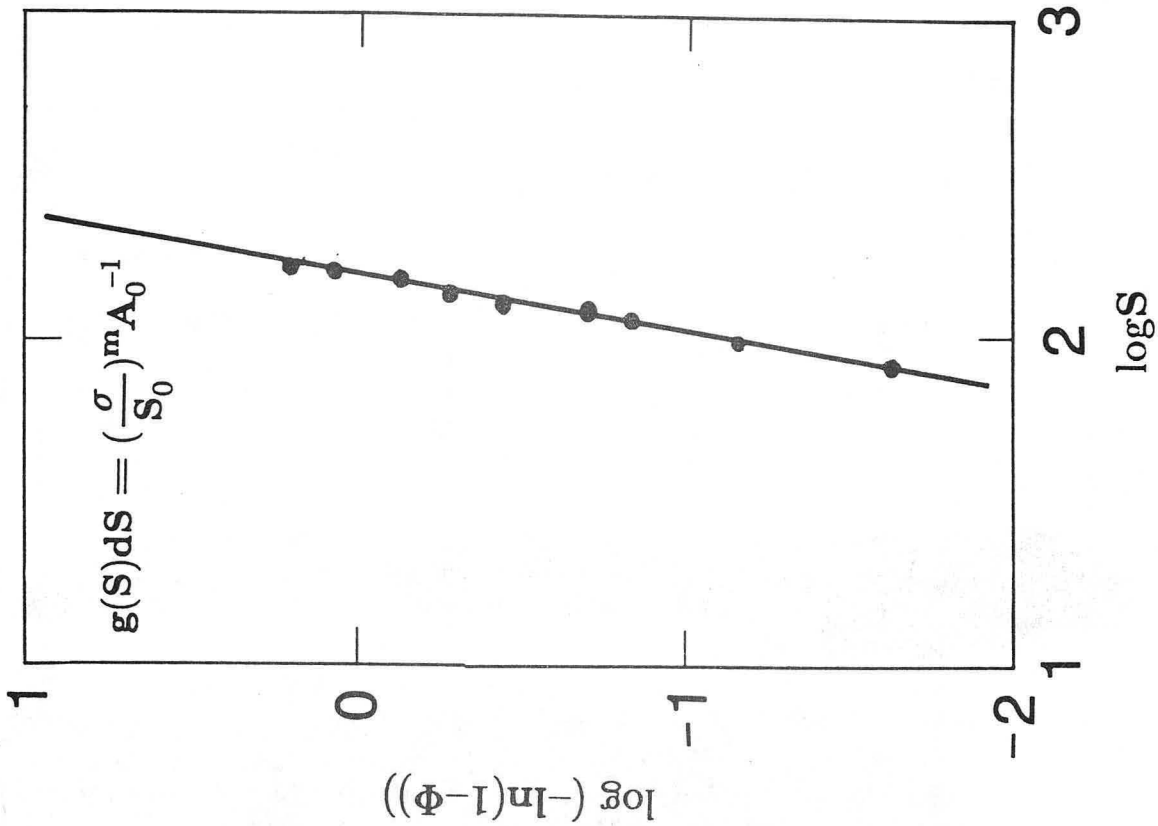

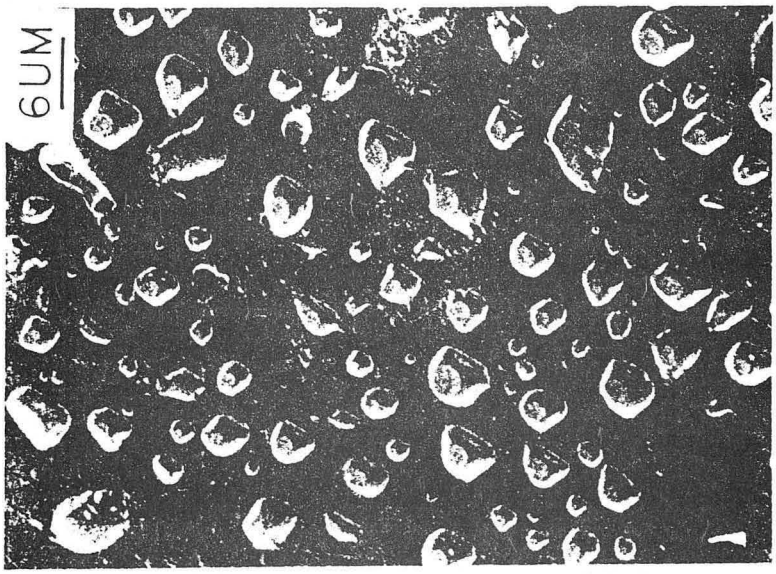

Fig.5-15

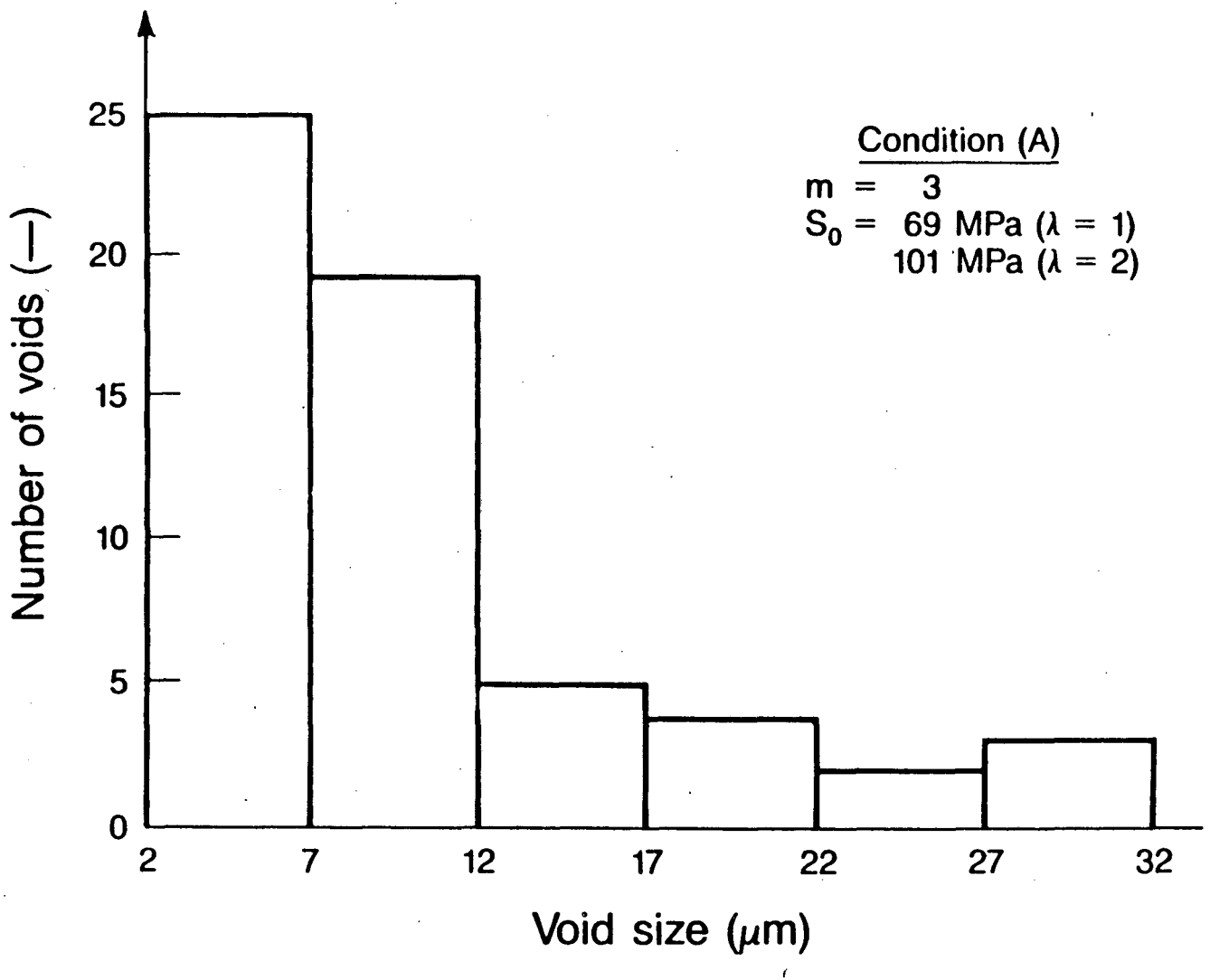

XBL 874-6268

Fig.5-16(a)

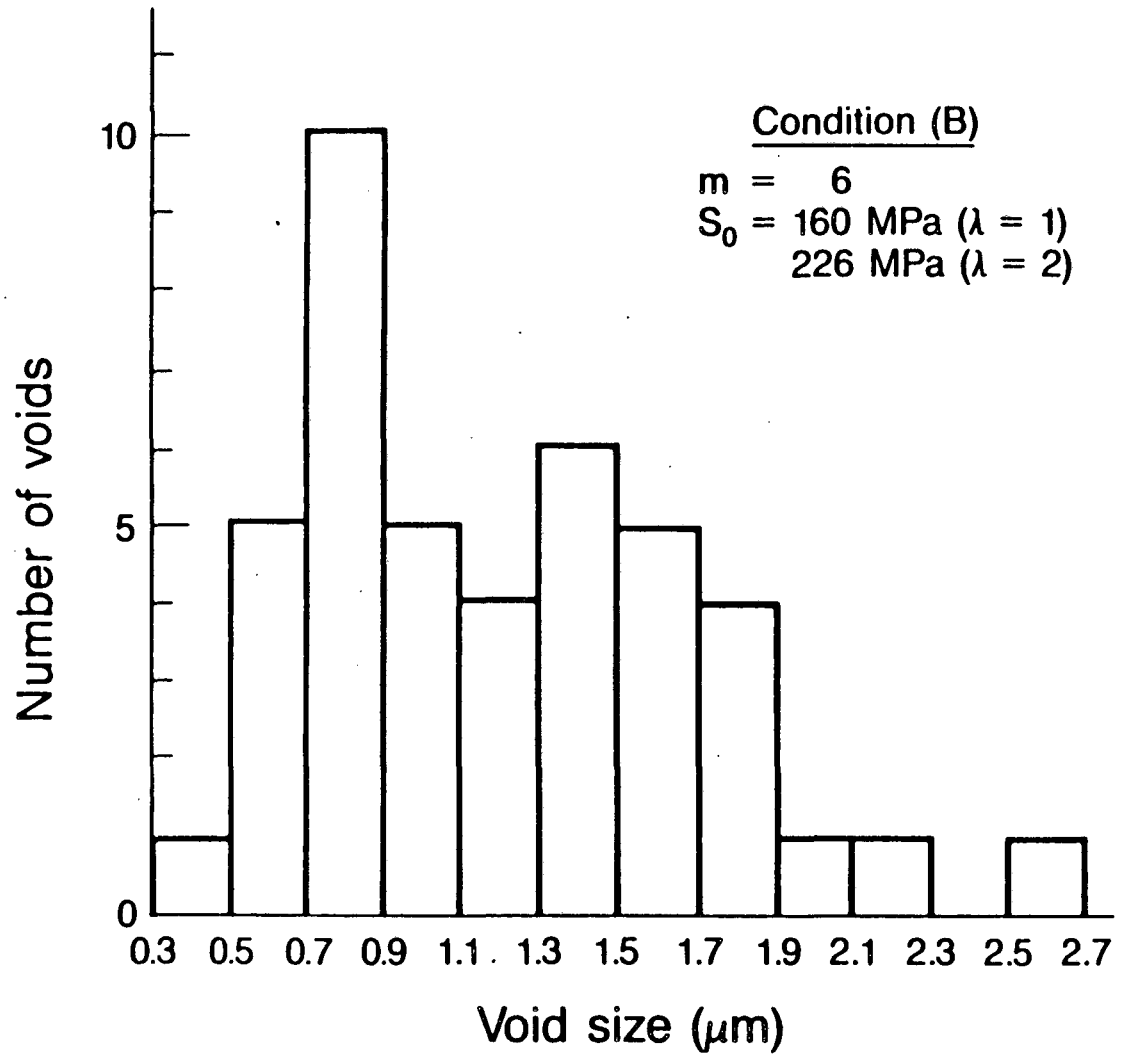

XBL 874-6269

Fig.5-16(b)

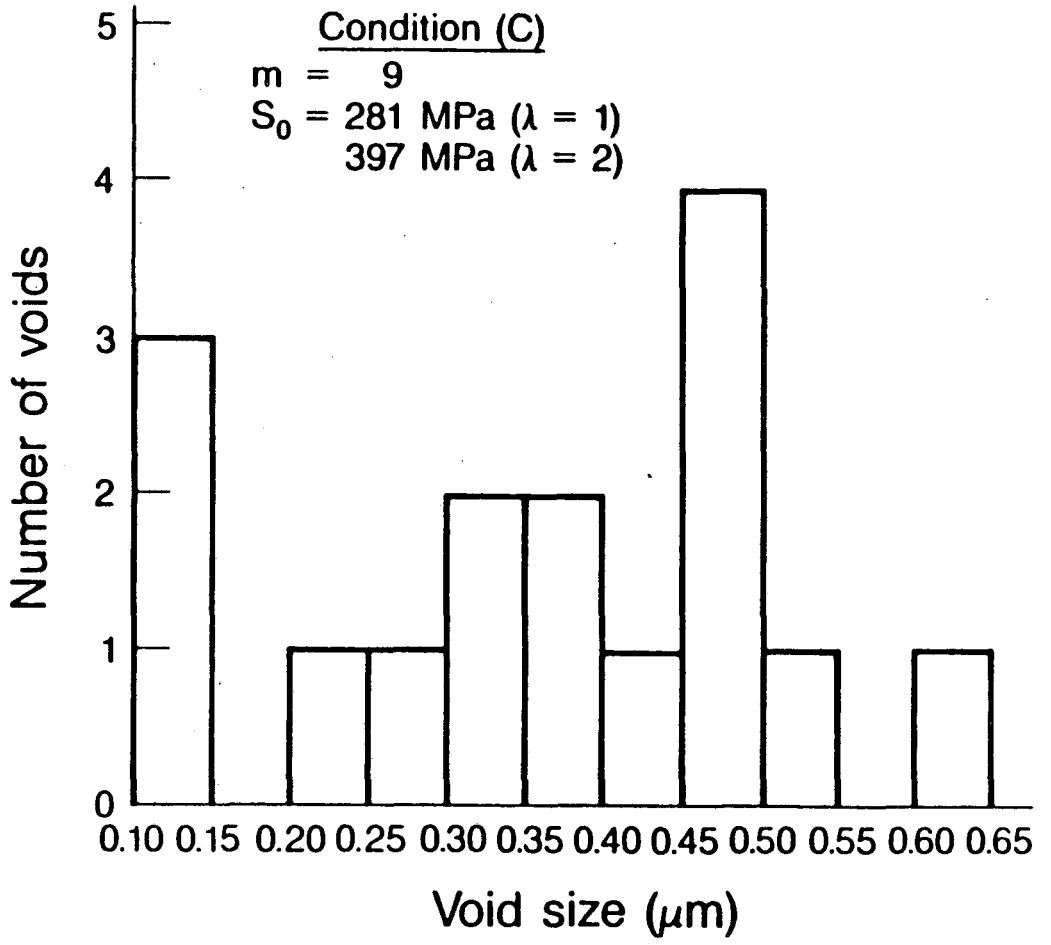

XBL 874-6270

Fig.5-16(c)

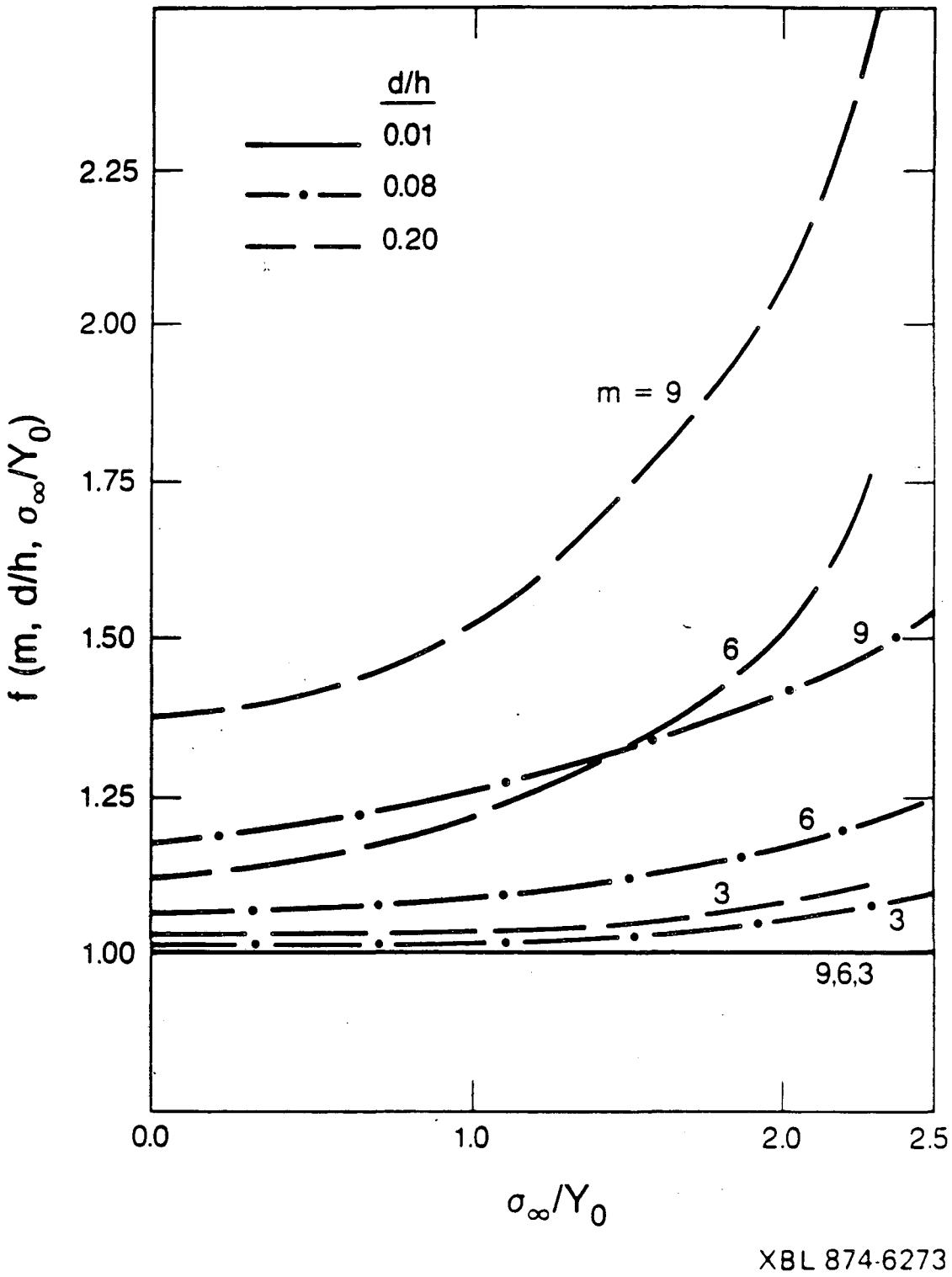
d/h
0.01
0.08
0.20
2.25
2.00
1.75
1.50
1.25
1.00
f (m, d/h, σ∞/Y0)
m = 9
6
9
6
3
3
9,6,3
0.0
1.0
2.0
2.5
σ∞/Y0
XBL 874-6273

Fig.5-17

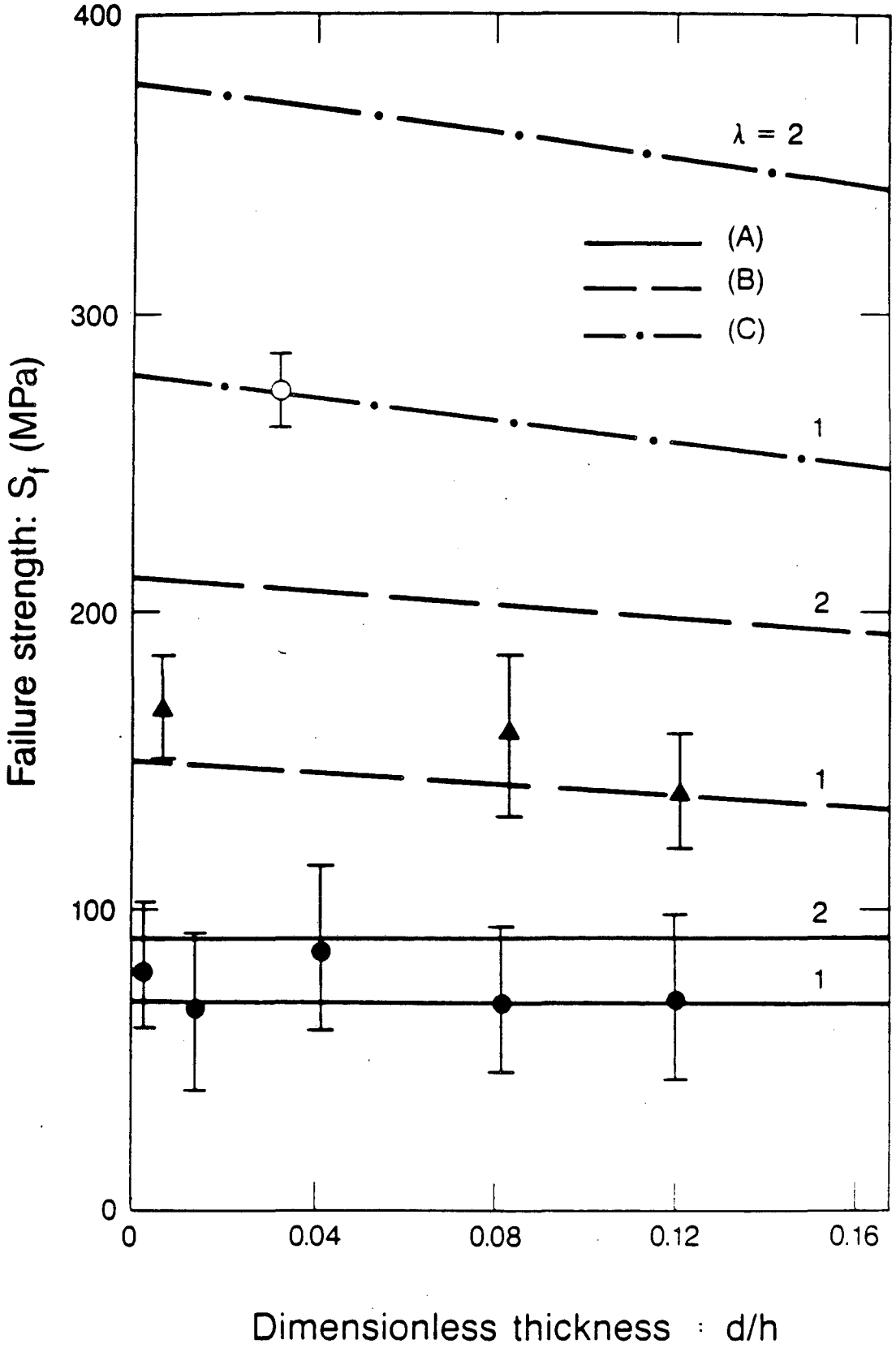

XBL 874-6271

Fig.5-18

CHAPTER 6

SUMMARY AND CONCLUSIONS

Metal plasticity has many effects on the behavior of metal/ceramic bonded systems. Stress concentrations at the edge can be limited by yield and interfacial cracks can be blunted. Conversely, plastic flow can induce residual stress around inclusions close to the interface. A limit load condition also exists, with the stress increasing markedly as the relative metal layer thickness decreases.

The interfacial strength is strongly dependent on the defects at the interface. Defects remaining at the interface become the pre-existing flaws. These void distributions make the interfacial strength sensitive to the interfacial stress distribution and, hence, the dimensionless metal interlayer thickness.

The strength trends are complicated. Nevertheless, a fracture mechanism map seems insightful, constructed in space bounded by the relative metal layer thickness and the stress relative to the yield strength (Fig.6-1). Two boundaries are derived from the transitions in the engineering stress-strain curves. One is the limit load for plastic flow limited failure. The other is the transition from small-scale yielding to large scale plasticity resulting in a transition from edge dominated failure to failure from the center. Furthermore, the strength of the ceramic and the edge stress can be placed in the map. With the separate knowledge of the interfacial defect distribution, an estimation of the strength of bonded system is provided.

One case (Fig.6-1) has the strength of the ceramic higher than both the yield strength and the edge stress concentration. Failure occurs at the interface with poor bonding. Otherwise, ductile fracture occurs with a thick metal interlayer or brittle fracture from a center crack in the ceramic for this metal layer.

The combination of materials in Fig.6-2 shows the case with the strength of ceramic lower than the limit of edge stress concentration. When the interfacial strength is strong failure strength is smaller than that of monolithic ceramic due to the edge failure enhanced by stress concentration. When the interfacial strength is poor, the strength is dependent of the competition of interfacial strength and the strength of edge failure in ceramic. Mismatch of material properties is important in this case.

The experimental example in the present work have the strength of ceramic to be about twice of the yield strength of metal (Fig.6-3). The edge dominated failure is eliminated. The thin metal layers obviate the ductile failure in metal too. Therefore, the strength is dominated by the microstructure at the interface. With very tiny and little voids at the interface, failure is limited in ceramic part. This satisfies the current prediction.

The strength of metal/ceramic bonded systems can thus be predicted by constructing the strength via geometric factor map so long as the strength of monolithic ceramic, the yield strength of metal and the microstructure of interface are known. Effects of edge stress concentration, limit load in fully plastic range and the ceramic strength are included. Damage model by inclusion or residual stresses can also be included if a sophisticated estimation is desired. Basically, a fundamental understanding of the strength of the bonded system has been presented in the present work.

Figure Captions:

Fig.6-1.

A failure mechanism map with strength of the ceramic material higher than that of the yield strength of the metal.

Fig.6-2.

A failure mechanism map with strength of the ceramic smaller than the limit of the edge stress concentration.

Fig.6-3.

A comparison of the present observation with the predicted failure mechanism map.

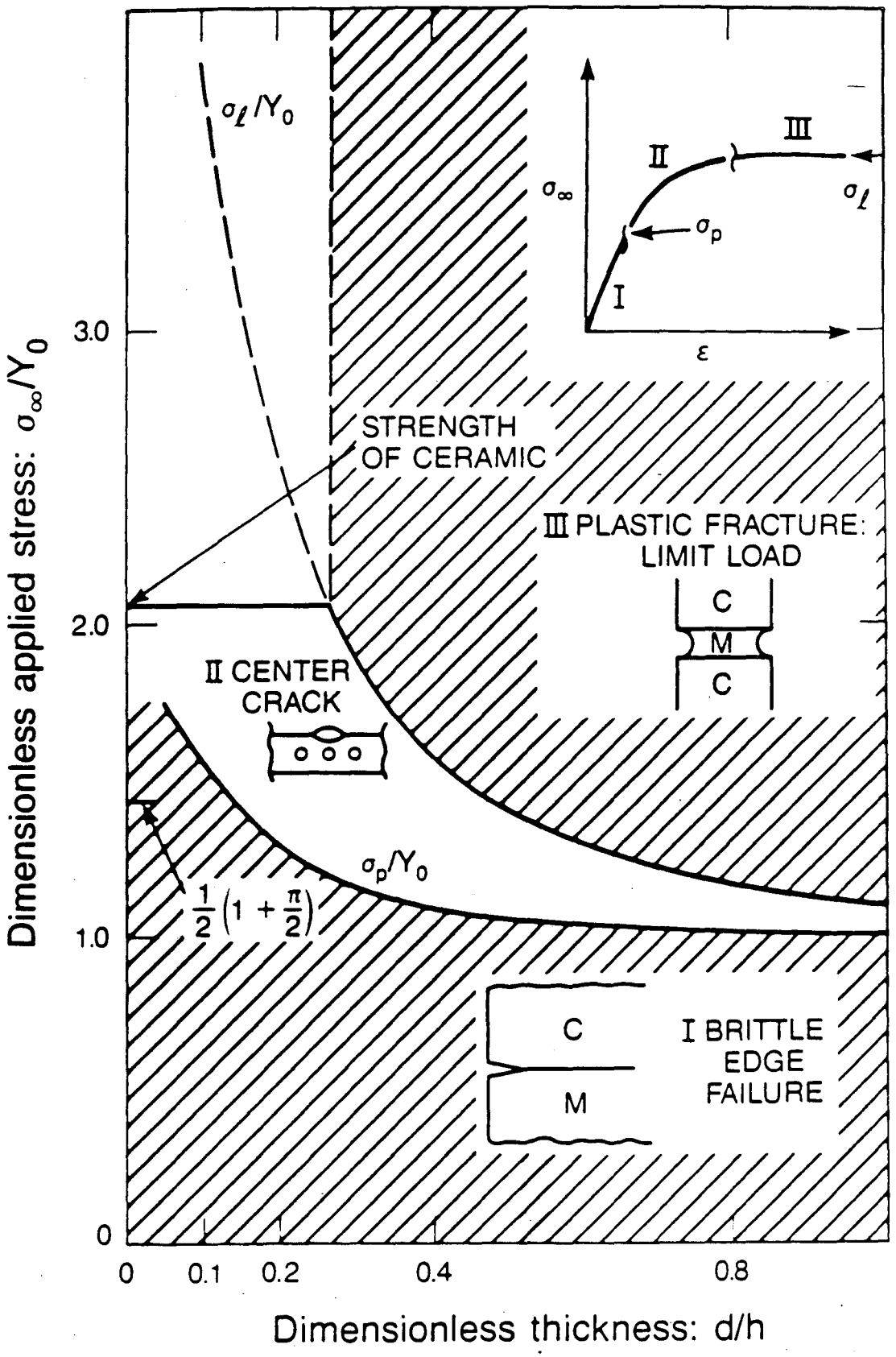

Fig.6-1

XBL 874-6274

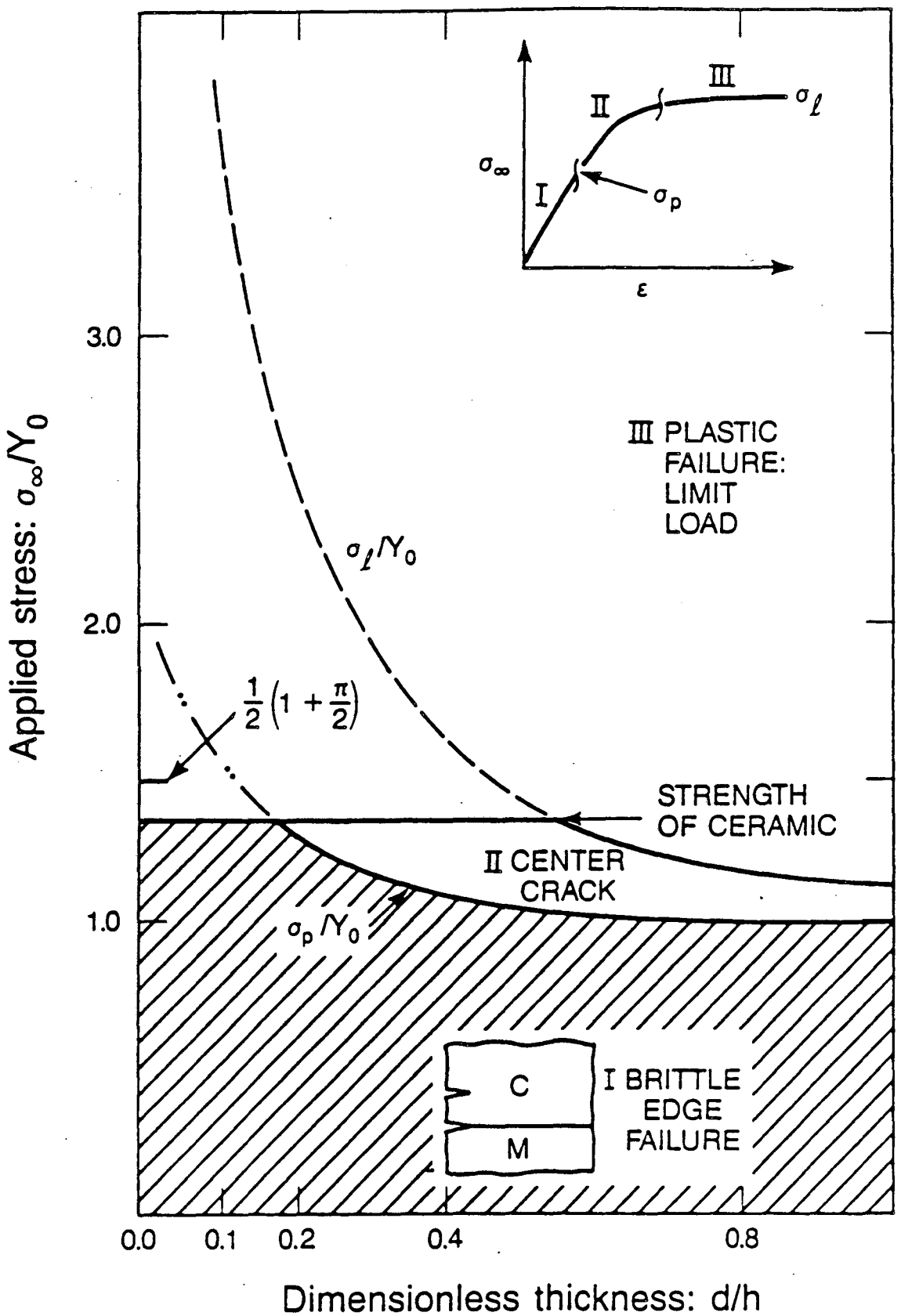

XBL 874-6285

Fig.6-2

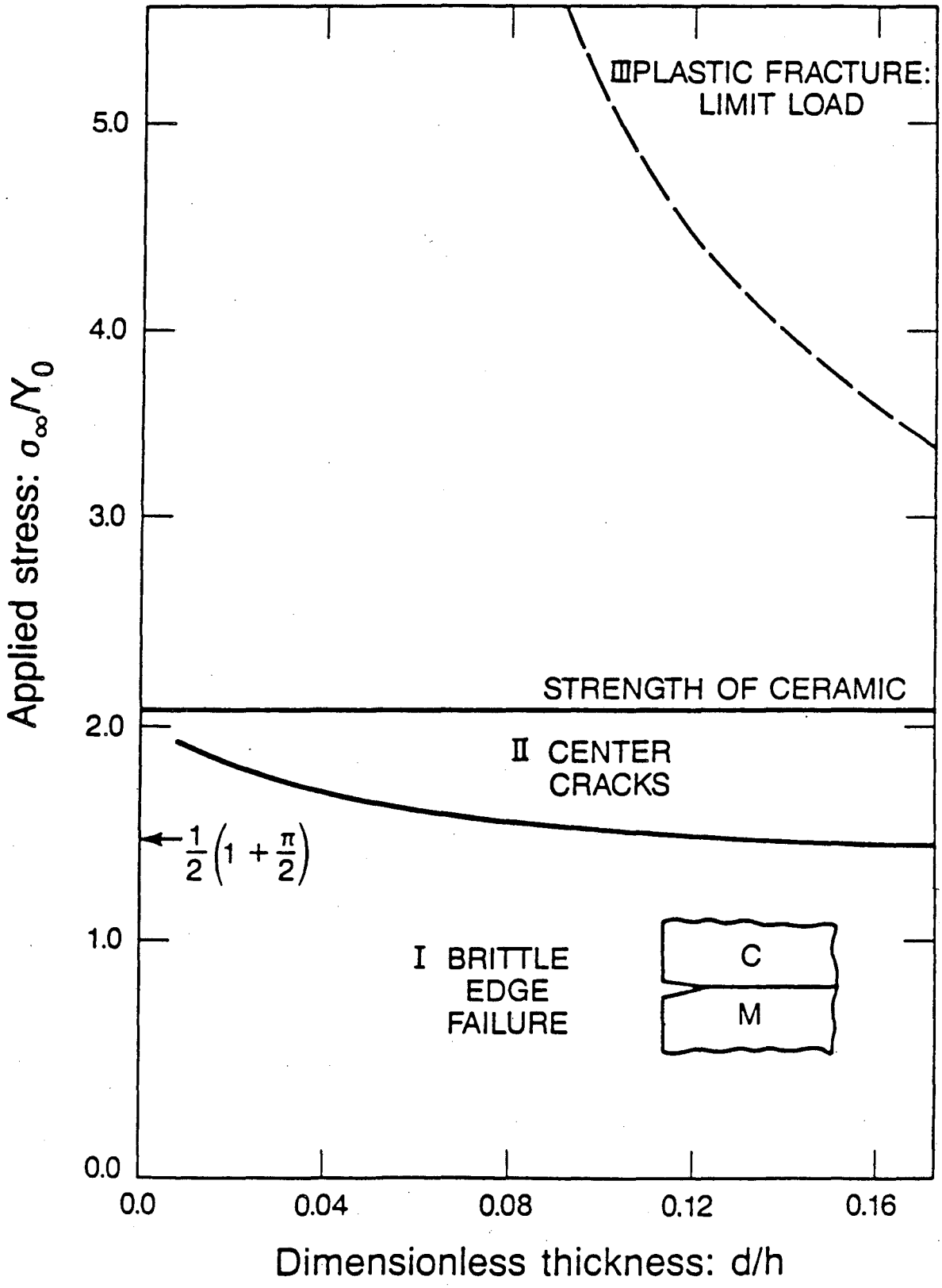

XBL 874-6277

Fig.6-3

REFERENCES

1. H. J. Sanders, "High-Tech Ceramics", *C&EN,* (1984), 26-40.

2. A. G. Evans, M. Ruhle, and M. Turwitt, "On the Mechanics of Failure in Ceramic/Metal Bonded Systems." *J. de Physique.* C4, (1985), 613-625.

3. A. G. Evans, M. C. Lu, S. Schmauder and M. Ruhle, "Some Aspects of the Mechanical Strength of Ceramic/Metal Bonded Systems", *Acta. Metall.* **34** (1986), 1643-1655.

4. C. H. Hsueh, and A. G. Evans, "Residual Stresses in Metal-Ceramic Bonded Strips" *J. Amer. Ceram. Soc.* **68,** (1985), 241-248.

5. R. M. Cannon, "Mechanical Properties of MgO and Al_2O_3" *Advances in Ceramics* **10,** (1984), 818-838.

Mechanics of Bimaterial Systems

6. J. Dundurs, "Effect of Elastic Constants on Stress in a Composite Under Plane Deformation", *J. of Composite Materials,* **1,** (1967),310-322.

7. D. B. Bogy, "Edge-Bonded Dissimilar Orthogonal Elastic Wedges Under Normal and Shear Loading", *J. Appl. Mech.,* **35,** (1986), 460-466.

8. J. Dundurs, "Discussion", *J. Appl. Mech.*, **36,** (1969), 650-652.

9. M. L. Williams, "The Stresses Around a Fault or Crack in Dissimilar Media", *Bull. of Seism. Soc. Amer.* **49,** (1959), 199-204.

10. F. Erdogan, "Stress Distribution in a Non-homogeneous Elastic Plane with Cracks", *J. Appl. Mech.*, **30,** (1963), 232-236.

11. A. H. England, "A Crack Between Dissimilar Media", *J. Appl. Mech.*, **32,** (1965), 400-402.

12. G. C. Sih and J. R. Rice, "The Bending of Plates of Dissimilar Materials with Cracks", *J. Appl. Mech.*, **31,** (1964), 477-486.

13. F. Erdogan, "Stress Distribution in Bonded Dissimilar Materials with Cracks", *J. Appl. Mech.*, **32,** (1965), 403-410.

14. J. R. Rice and G. C. Sih, "Plane Problems of Cracks in Dissimilar Media", *J. appl. Mech.* **32,** (1965), 418-423.

15. E. M. Wu and R. L. Thomas, "Interfacial Facture Phenomena", Proceedings, The Fifth International Congress on Rheology. (1969), 575-587.

16. F. Erdogan and G. Gupta, "The Stress Analysis of Multi-Layered Composites with a Flaw", *Int. J. Sol. Struc.*, **7,** (1971), 39-61.

17. S. G. Sawyer and R. B. Anderson, "Collocated Interfacial Stress Intensity Factors for Finite Bi-Material Plates", *Eng. Frac. Mech.*, **4**, (1972), 605-616.

18. V. L. Hein and F. Erdogan, "Stress Singularities in a Two-Material Wedge", *Int. J. Frac. Mech.*, **7**, (1971), 317-330.

19. A. Piva and E. Viola, "Biaxial Load Effects on a Crack Between Dissimilar Media", *Eng. Frac. Mech.*, **13**, (1980), 143-174.

20. S. S. Wang and F. G. Yuan, "A Hybrid Finite Element Approach to Composite Laminate Elasticity Problems with Singularities", *J. Appl. Mech.*, **50**, (1983), 835-844.

21. G. Elssner, T. Suga and M. Turwitt, "Fracture of Ceramic-to-Metal Interfces", Conference Paper.

22. D. B. Bogy, "The Plane Solution for Joined Dissimilar Elastic Semistrips Under Tension", *J. Appl. Mech.*, **42**, (1975), 93-98.

Joining of Materials

23. H. J. De Bruin, A. F. Moodie, and C. E. Warble, "Ceramic-Metal Reaction Welding", *J. Mat. Sci.*, **7**, (1972), 909-918.

24. J. F. Burgess, C. A. Neugebauer and G. Flanagan, "The Direct Bonding of Metals to Ceramics by the Gas-Metal Eutectic Method", *J.*

Electrochem. Soc., **122,** (1975), 688-690.

25. G. Elssner, S. Riedel, and R. Pabst, "Fractography and Fracture Paths in Ceramic-Metal Composites", *Prac. Metall.* **12,** (1975), 234-243.

26. S. V. Pepper, "Shear Strength of Metal-Sapphire Contacts", *J. Appl. Mech.*, **47,** (1976), 801-808.

27. A. F. Moodie and C. E. Warble, "Direct Observation of Pd/MgO and *Pd* /SiO_2 Reactions in the Transmission Electron Microscope", *Phil. Mag.* **35,** (1977), 201-211.

28. F. P. Bailey and K. J. T. Black, "Gold-to-Alumina Solid State Reaction Bonding", *J. Mat. Sci.*, **13,** (1978), 1045-1052.

29. F. P. Bailey and K. J. T. Black, "The Effect of Ambient Atmosphere on the Gold-to-Alumina Solid State Reaction Bond", *J. Mat. Sci.*, **13,** (1978) Letters, 1606-1608.

30. F. P. Bailey and W. E. Borbidge, "Solid-State Metal-Ceramic reaction Bonding", Material Science Research vol.14, (1982).

31. M. E. Twentyman and P. Hancock", High-Temperature Metallizing of Alumina", Material Science Research, vol.14, (1982), 535-545.

32. G. Elssner, W. Diem, J. S. Wallace, "Microstructure and Mechanical Properties of Metal-to-Ceramic and Ceramic-to-Ceramic Joints", Material Science Research, Vol.14, (1982), 629-639.

33. R. F. Pabst and G. Elssner, "Adherence Properties of Metal-to-Ceramic Joints", *J. Mat. Sci.*, **15,** (1980), 188-196.

34. J. T. Klomp, and J. C. Van De Ven, "Parameters in Solid-State Bonding of Metals to Oxide Materials and the Adherence of Bonds, "*J. Mat. Sci.*, **15,** (1980), 2483-2488.

35. S. Morozumi, M. Kikuchi, and T. Nishino, "Bonding Mechanism Between Alumina and Niobium", *J. Mat. Sci.*, **16,** (1981), 2137-2144.

36. R. V. Allen, and W. E. Borbidge, "Solid State Metal-Ceramic Bonding of Platinum to Alumina", *J. Mat. Sci.*, **18,** (1983), 2835-2843.

37. P. Popper, "The Joining of Industrial Ceramics to Metals", 569-581.

38. H. J. de Bruin, S. P. S. Badwal and P. W. Slatery, "The Nature of the Metal/Ceramic Interface. (1980), 1038-1050.

39. M. Turwitt, G. Elssner and G. Petzow, "Manufacturing and Mechanical Properties of Interfaces Between Sapphire and Niobium", Conference Paper.

40. R. G. Hill, R. P. Nelson and C. L. Hellerich, "Composites work at Battelle-Northwest", Battelle Memorial Inst., Pacific Northwest Lab., 16th Refractory Composties Working Group Meeting, Seattle, Washington, Oct.(1969).

Diffusion Bonding Mechanism

41. B. Derby and E. R. Wallach, "Theoretical Model for Diffusion Bonding" *Matel. Sci.* **16,** (1982), 49-56.

42. B. Derby and E. R. Wallach, "Diffusion Bonds in Iron and a Low-Alloy Steel' *Mat. Sci.* **19** (1984), 3149-3158.

43. B. Derby and E. R. Wallach, "Diffusion Bonding: Development of Theoretical Model", *J. Mat. Sci.* **18,** (1984),427-431.

44. B. Derby and E. R. Wallach, "Diffusion Bonds in Copper", *J. Mat. Sci.* **19,** (1984), 3140-3149.

Work of Adhesion

45. E. D. Hondros, "Bonding of Metal/Ceramic Interfaces", Inst. Phys. Conf. Ser. No.75: Chapter 2.

46. R. M. Pillar and J. Nutting, "Solid-Solid Interfacial Energy Determinations in Metal-Ceramic Systems" *Phil. Mag.* **16,** (1967), 181-188.

47. M. Nicholas, R. R. D. Forgan, and D. M. Poole, "The Adhesion of Metal/Alumina Interfaces", *J. Mat. Sci.*, **3**, (1968), 9-14.

48. M. Nicholas, "The Strength of Metal/Alumina Interfaces", *J. Mat. Sci.*, **3**, (1968), 571-576.

Finite Element Analysis

49. M. W. Johnson and R. W. McLay, "Convergence of the Finite Element Method in the Theory of Elasticity", *J. Appl. Mech.*, **35**, (1968), 274-278.

50. D. F. Mowbray, "A Note On the Finite Element Method in Linear Fracture Mechanics", *Eng. Frac. Mech.*, **2**, (1970), 173-176.

51. S. K. Chan, I. S. Tuba and W. K. Wilson, "On the Finite Element Method in Linear Fracture Mechanics", *Eng. Frac. Mech.*, **2**, (1970),1-17.

52. G. P. Anderson, V. L. Ruggles and G. S. Stibor, "Use of Finite Element computer Programs in Fracture Mechanics", *Int. J. of Frac.*, **7**, (1971), 63-76.

53. D. M. Parks, "A Stiffness Derivative Finite Element Technique for Determination of Crack Tip Stress Intensity Factors", *Int. F. Frac.*, **10** (1974), 487-502.

54. T. K. Hellen, "On the Mehtod of Virtual Crack Extensions", *Int. J. for Num. Meth. in Eng.*, **9**, (1975), 187-207.

55. K. Y. Lin and J. W. Mar, "Finite Element Analysis of Stress Intensity Factors for Cracks at a Bi-material Interface", *Int. J. Frac.*, **12,** (1976), 521-531.

56. E. F. Rybicki and M. F. Kannien, "A Finite Element Calculation of Stress Intensity Factors by a Modified Crack Closure Integral", *Eng. Frac. Mech.*, **9,** (1977), 931-938.

57. J. J. Guydish and J. F. Fleming, "Optimization of the Finite Element Mesh for the Solution of Fracture Problems", *Eng. Frac. Mech.*, **10,** (1978), 31-42.

58. G. T. Sha, "On the Virtual Crack Extension Technique for Stress Intensity Factors and Energy Release Rate Calculations for Mixed Fracture Mode", *Int. J. Frac.*, **25,** (1984), R33-R34.

59. T. K. O'Brien, N. J. Johnson, D. H. Morris and R. A. Simonds, "Determination of Interlaminar Fracture Toughness and Facture Mode Dependence of Composites Using the Edge Delamination Test", Presented at the International conference on Testing, Evaluation, and Quality Control of Composites", (1983), Guildford, England.

60. T. K. O'Brien, "Mixzed-Mode Strain-Energy Release Rate Effects on Edge Delamination of Composites", NASA Technical Memorandum 84592, (1983).

61. R. Hill, "The Mathematical Theory of Plasticity", Oxford Eng. Sci. Series, 1950.

62. J. C. Nagtegaal, D. M. Parks and J. R. Rice, "On Numerically Accurate Finite Element Solutions in the Fully Plastic Range", *Comp. Meth. in Appl. Mech. and Eng.*, **4,** (1974), 153-177.

63. J. C. Simo and R. L. Taylor, "Consistent Tangent Operators for Rate Independent Elasto-Plasticity" *Comp. Meth. Appl. Mech. Eng.* **48,** (1985), 101-118.

64. J. L. Loubet, J. M. Georges, and G. Meille, " Vickers Indentation Curves of Elastoplastic Materials", ASTM STP 889, (1986), 27-89.

Statistical Analysis

65. W. Weibull, "Statistical Distribution Function of Wide Applicability" *J. Appl. Mech.* **18** (1951), 293-297.

66. A. G. Evans and R. L. Jones, "Evaluation of a Fundamental Approach for the Statistical Analysis of Fracture", *J. Amer. Ceram. Soc.* **61,** (1978),156-160.

67. A. G. Evans, "Statistical Aspects of Cleavage Fracture in Steel", *Metal. Trans. A* **14A,** (1983), 1349-1355.

68. T. Lin, A. G. Evans, And R. O. Ritchie, "A Statistical Model of Brittle Fracture by Transgranular Cleavage", *J. Mech. Phys. solids.* **34** (1986), 477-497.

This report was done with support from the Department of Energy. Any conclusions or opinions expressed in this report represent solely those of the author(s) and not necessarily those of The Regents of the University of California, the Lawrence Berkeley Laboratory or the Department of Energy.

Reference to a company or product name does not imply approval or recommendation of the product by the University of California or the U.S. Department of Energy to the exclusion of others that may be suitable.

LAWRENCE BERKELEY LABORATORY
TECHNICAL INFORMATION DEPARTMENT
UNIVERSITY OF CALIFORNIA
BERKELEY, CALIFORNIA 94720